University of Cyprus

Department of Electrical and Computer Engineering

Optimization and Management of Distributed Energy Resources in Power Systems

Lysandros Tziovani

A Dissertation
Submitted in Partial Fulfillment of the
Requirements for the Degree of
Doctor of Philosophy
at the University of Cyprus

April, 2023

VALIDATION PAGE

Doctoral Candidate: Lysandros Tziovani

Doctoral Dissertation Title: Optimization and Management of Distributed Energy Resources in Power Systems

The present Doctorate Dissertation was submitted in partial fulfillment of the requirements for the Degree of Doctor of Philosophy in the ***Department of*** *Electrical and Computer Engineering, and was approved on April 5, 2023 by the members of the* ***Examination Committee****.*

Examination Committee:

Committee Chair _____
Dr. Christos Panayiotou, Professor

Research Supervisor _____
Dr. Stelios Timotheou, Assistant Professor

Research Supervisor _____
Dr. Lenos Hadjidemetriou, Research Lecturer

Committee Member _____
Dr. Mathaios Panteli, Assistant Professor

Committee Member _____
Dr. Angelos Georghiou, Assistant Professor

Committee Member _____
Dr. Alessandro Astolfi, Professor

DECLARATION OF DOCTORAL CANDIDATE

The present doctoral dissertation was submitted in partial fulfillment of the requirements for the degree of Doctor of Philosophy of the University of Cyprus. It is a product of original work of my own, unless otherwise mentioned through references, notes, or any other statements.

Lysandros Tziovani

I dedicate this PhD thesis to my late father, Ioannis Tziovani, and my supervisor, Elias Kyriakides, who both passed away during my doctoral studies. My father battled with the rapidly progressive and fatal Creutzfeldt-Jakob disease and passed away on May 27, 2021. Professor Kyriakides, who bravely fought cancer, passed away on October 28, 2019.

May God rest their souls.

ΠΕΡΙΛΗΨΗ

Η αυξανόμενη διείσδυση των ανανεώσιμων πηγών ενέργειας (ΑΠΕ) στο ηλεκτρικό σύστημα εισάγει πολλαπλές προκλήσεις ασφάλειας, αξιοπιστίας και αποδοτικότητας, κυρίως λόγω της ανεξέλεγκτης παραγωγής ΑΠΕ. Τα συστήματα αποθήκευσης ενέργειας (ΣΑΕ) αποτελούν μια αναδυόμενη τεχνολογία που μπορεί να αντισταθμίσει τα αρνητικά αποτελέσματα της παραγωγής ΑΠΕ μέσω της βέλτιστης διαχείρισης της ενέργειας που παράγεται από τις ΑΠΕ.

Ο κύριος στόχος αυτής της διδακτορικής διατριβής αφορά την επίλυση προβλημάτων βελτιστοποίησης που σχετίζονται με τη διαχείριση κατανεμημένων πηγών ενέργειας σε ηλεκτρικά συστήματα με υψηλή διείσδυση ΑΠΕ και ΣΑΕ. Τέτοια προβλήματα είναι δύσκολο να επιλυθούν καθώς απαιτούν γρήγορες και βέλτιστες ή υψηλής ποιότητας λύσεις και συχνά συνδέονται με ανακρίβειες μοντελοποίησης και αβεβαιότητα στην παραγωγή ενέργειας από ΑΠΕ. Σε αυτό το πλαίσιο, έχουν μελετηθεί τα ακόλουθα προβλήματα: (α) η βελτιστοποίηση γενικών προβλημάτων διαχείρισης ενέργειας σε συστήματα ηλεκτρικής ισχύος που περιλαμβάνουν μη-κυρτά μοντέλα των ΣΑΕ, (β) η διαχείριση ενέργειας από φωτοβολταϊκά και συστήματα μπαταριών σε ενεργά δίκτυα διανομής, (γ) η διαχείριση ενέργειας ενός συστήματος αποθήκευσης με σφόνδυλο για την μείωση των κορυφών φορτίου στα ηλεκτρικά δίκτυα και (δ) η βελτιστοποίηση της στρατηγικής υποβολής προσφορών από παραγωγούς ΑΠΕ στις αγορές ηλεκτρικής ενέργειας χρησιμοποιώντας συστήματα μπαταριών.

Το πρώτο πρόβλημα έχει σκοπό να αναπτύξει μια γρήγορη και αποτελεσματική μεθοδολογία για τη βελτιστοποίηση γενικών προβλημάτων διαχείρισης ενέργειας σε συστήματα ηλεκτρικής ισχύος που περιλαμβάνουν μη-κυρτά μοντέλα των ΣΑΕ. Στη βιβλιογραφία αναπτύσσονται ποικίλα μοντέλα ΣΑΕ που χρησιμοποιούν μη-κυρτούς περιορισμούς για να αναπαραστήσουν τις απώλειες ισχύος των ΣΑΕ, με αποτέλεσμα τα προκύπτοντα προβλήματα βελτιστοποίησης να είναι δύσκολο να επιλυθούν. Για να μειωθεί η πολυπλοκότητα, συνήθως αναπτύσσονται μοντέλα ΣΑΕ τα οποία χαλαρώνουν τους μη-κυρτούς περιορισμούς, αλλά παράγουν μη εφικτές λύσεις όταν παραβιάζεται η ακρίβεια της χα-

λάρωσης. Για να αντιμετωπιστεί αυτό το ζήτημα, η παρούσα διατριβή αναπτύσσει δύο επαναληπτικούς αλγορίθμους που δημιουργούν γρήγορες και υψηλής ποιότητας εφικτές λύσεις όταν η προκύπτουσα λύση παραβιάζει την ακρίβεια της χαλάρωσης. Ο πρώτος αλγόριθμος αντιμετωπίζει γενικές συναρτήσεις απώλειας ενέργειας των ΣΑΕ, ενώ ο δεύτερος εξειδικευμένος αλγόριθμος βελτιώνει την απόδοση του πρώτου αλγορίθμου όταν χρησιμοποιούνται τμηματικά γραμμικές συναρτήσεις απώλειας ενέργειας. Συγκεκριμένα, και οι δύο αλγόριθμοι μειώνουν σε κάθε επανάληψη την εφικτή περιοχή των χαλαρωμένων μοντέλων ΣΑΕ, χρησιμοποιώντας μια περιοχή εμπιστοσύνης γύρω από την προκύπτουσα λύση.

Το δεύτερο πρόβλημα αποσκοπεί στη διαχείριση της λειτουργίας ενός ενεργού δικτύου διανομής με τον έλεγχο των συστημάτων φωτοβολταϊκής ενέργειας και μπαταριών των παραγωγών/καταναλωτών. Για την επίλυση αυτού του προβλήματος, αναπτύσσεται ένα κυρτό μοντέλο βελτιστοποίησης, χαλαρώνοντας τους μη-κυρτούς περιορισμούς ροής ισχύος και ΣΑΕ. Επιπλέον, προτείνονται δύο αλγόριθμοι λύσης που (α) διασφαλίζουν την εφικτότητα του χαλαρωμένου μοντέλου και (β) παρέχουν μια δίκαιη κατανομή του κόστους μεταξύ των παραγωγών/καταναλωτών και του διαχειριστή λειτουργίας του συστήματος.

Το τρίτο πρόβλημα έχει σκοπό να εξαλείψει τις παραβιάσεις ισχύος που συμβαίνουν στους μετασχηματιστές διανομής, λόγω της υψηλής διείσδυσης των ανανεώσιμων πηγών ενέργειας και της αύξησης της ζήτησης φορτίου. Η επίλυση αυτού του προβλήματος πραγματοποιείται με την χρήση ενός συστήματος αποθήκευσης ενέργειας με σφόνδυλο. Για την επίτευξη αυτού του στόχου, παράγονται κυρτές συναρτήσεις που αντιπροσωπεύουν τις απώλειες ισχύος του σφονδύλου και τη μέγιστη ισχύ του και στη συνέχεια ενσωματώνονται σε ένα μοντέλο βελτιστοποίησης λεξικογραφικής ταξινόμησης. Επιπλέον, παρουσιάζεται ένα ιεραρχικό πλαίσιο ελέγχου δύο επιπέδων για την λειτουργία του συστήματος μετασχηματιστή και σφονδύλου το οποίο αντιμετωπίζει τα σφάλματα πρόβλεψης φορτίου και τις ανακρίβειες μοντελοποίησης. Στο υψηλότερο επίπεδο, αναπτύσσεται ένας προβλεπτικός ελεγκτής που επιλύει το μοντέλο βελτιστοποίησης λεξικογραφικής ταξινόμησης. Στο χαμηλότερο επίπεδο, ένας δευτερεύων ελεγκτής διορθώνει τα σημεία ρύθμισης ισχύος του προβλεπτικού ελεγκτή, χρησιμοποιώντας μετρήσεις σε πραγματικό χρόνο.

Το τέταρτο πρόβλημα αποσκοπεί στη στρατηγική υποβολής προσφορών από παραγωγούς ΑΠΕ στις αγορές ηλεκτρικής ενέργειας με στόχο τη μεγιστοποίηση των κερδών τους από την πώληση ενέργειας. Για την επίτευξη αυτού του στόχου, χρησιμοποιούνται συστήματα μπαταριών και λαμβάνονται υπόψη δύο παράγοντες, α) η απώλεια διάρκειας ζωής της μπαταρίας και β) τα όρια του δικτύου λόγω συμφόρησης μετάδοσης

ισχύος. Για την επίλυση αυτού του προβλήματος, αναπτύχθηκε ένα στοχαστικό μοντέλο βελτιστοποίησης βασισμένο σε σενάρια για τη διαχείριση της αβεβαιότητας στην παραγωγή ηλεκτρικής ενέργειας από ΑΠΕ και στις τιμές ηλεκτρικής ενέργειας. Το στοχαστικό μοντέλο διατυπώνεται ως πρόβλημα γραμμικού προγραμματισμού, το οποίο μπορεί να επιλυθεί γρήγορα και αξιόπιστα, χρησιμοποιώντας ένα προσεγγιστικό μοντέλο για την απώλεια διάρκειας ζωής της μπαταρίας και ένα χαλαρωμένο μοντέλο ΣΑΕ.

Οι προσομοιώσεις και τα πειραματικά αποτελέσματα επιβεβαιώνουν την αποτελεσματικότητα των προτεινόμενων μεθόδων επίλυσης των εξεταζόμενων προβλημάτων, διασφαλίζοντας την ασφαλή, αξιόπιστη και αποδοτική λειτουργία του συστήματος ηλεκτρικής ενέργειας.

Abstract

The increasing penetration of renewable energy sources (RESs) into the power system introduces several safety, reliability and efficiency challenges, mainly due to the uncontrollability of RES. Energy storage systems (ESSs) constitute an emerging technology that can compensate the negative effects of intermittent RES generation by optimally managing the energy produced by RES.

The main aim of this PhD thesis regards the solution of optimization problems associated with the management of distributed energy resources in power systems with high RES and ESS penetration. Such problems are challenging because they require fast and optimal or close-to-optimal solutions, and often involve modelling inaccuracies and RES uncertainty. In this context, the following problems are considered: (i) optimization of general energy management problems in power systems involving non-convex ESS models, (ii) energy management of photovoltaic and battery storage systems in active distribution grids, (iii) energy management of a flywheel storage system for peak shaving applications, and (iv) stochastic optimization of the bidding strategy of RES producers in electricity markets considering battery degradation.

The first problem aims to develop a fast and effective methodology for optimizing general energy management problems in power systems involving non-convex ESS models. Different ESS models are developed that utilize non-convex constraints to represent the ESS power losses, resulting in challenging optimization problems. To reduce the complexity, convex relaxation models are often derived but generate infeasible solutions when the relaxation exactness is violated. To deal with this issue, this thesis develops two successive convexification algorithms that generate fast and high-quality feasible solutions when the derived solution is not exact. The first algorithm handles general ESS loss functions, while the second algorithm enhances performance when piecewise-linear loss functions are used. The general idea of

the algorithms is to reduce the feasible region of the relaxed ESS models using a tightening box trust region around the current solution in successive iterations.

The second problem aims to manage the operation of an active distribution grid by controlling the photovoltaic and battery energy storage systems (BESSs) of prosumers. To solve this problem, a convex multi-objective optimization model is formulated by relaxing the non-convex power flow and BESS constraints. Two solution algorithms are developed that (a) ensure feasibility of the relaxed model and (b) provide a fair allocation of the costs between the prosumers and the system operator.

The scope of the third problem is to eliminate the power violations occurring in distribution transformers, due to the high RES penetration and load demand growth, using a flywheel energy storage system. For the solution of this problem, convex functions that represent the flywheel power losses and its maximum power are derived and integrated in a lexicographic optimization scheme. A two-level hierarchical control framework to operate the transformer-flywheel-system in a way that handles prediction errors and modelling inaccuracies is also introduced. At the higher level, a model predictive controller (MPC) is developed that solves the lexicographic optimization scheme. At the lower-level, a secondary controller corrects the power set-points of the MPC using real-time measurements.

The fourth problem aims to develop a bidding strategy for combined BESS-RES plants to maximize the expected producer profits in day-ahead and balancing electricity markets, considering battery degradation and power exchange limitations with the grid due to transmission congestion. Towards this direction, a two-stage scenario-based stochastic optimization scheme is developed to deal with uncertainties in RES power generation, day-ahead energy prices, and imbalance prices. The considered stochastic scheme is formulated as a linear program, which can be fast and reliably solved, by utilizing an approximate cycle-based degradation model and a relaxed BESS model.

Simulation and/or experimental results validate the quality of the developed solution approaches for the considered problems in ensuring the safe, reliable, and efficient operation of the power system.

Acknowledgments

I would like to express my sincere gratitude to my doctoral supervisors: the late Professor Elias Kyriakides, Professor Stelios Timotheou, and Dr. Lenos Hadjidemetriou. Professor Kyriakides, who was my supervisor during my BSc and MSc studies, provided me with the opportunity to pursue a Ph.D. degree at KIOS CoE. I am forever grateful for his trust and support. His dedication to academic excellence, passion for research, and unwavering support will always be remembered.

Professor Stelios Timotheou played a pivotal role in shaping this PhD dissertation, and I am grateful for his kindness and constant support both on a personal and academic level. His expertise in the field was invaluable, and I feel privileged to have learned from such an exceptional scientist.

I would also like to thank Dr. Lenos Hadjidemetriou for his insightful comments and ideas, his guidance in developing my research skills, and his unwavering support during my doctoral studies. Both Professor Timotheou and Dr. Hadjidemetriou were not only exceptional advisors and scientists, but also wonderful friends.

I would like to express my sincere thanks to all of my co-authors, and especially to Dr. Irina Ciornei, Dr. Markos Asprou, Dr. Panayiotis Kolios, and Professor Alessandro Astolfi, for their effective collaboration and shared research experience throughout these years.

Finally, I wish to express my deepest and most sincere gratitude to my parents, Ioannis and Maria, and my sisters, Antri, Panayiota, Loukia, and Tziovana, for their support and unconditional love throughout my entire life. I am incredibly grateful to my late father, who passed away before the completion of this thesis. I am certain he would have been proud of this achievement. Moreover, I would like to extend my thanks to my friends for their constant encouragement and support.

Lysandros Tziovani

Publications

Journal Papers

1. **L. Tziovani**, L. Hadjidemetriou, P. Kolios, A. Astolfi, E. Kyriakides and S. Timotheou, “Energy Management and Control of Photovoltaic and Storage Systems in Active Distribution Grids," in *IEEE Transactions on Power Systems*, vol. 37, no. 3, pp. 1956-1968, May 2022.

2. **L. Tziovani**, L. Hadjidemetriou, C. Charalambous, M. Tziakouri, S. Timotheou and E. Kyriakides, “Energy Management and Control of a Flywheel Storage System for Peak Shaving Applications," in *IEEE Transactions on Smart Grid*, vol. 12, no. 5, pp. 4195-4207, Sept. 2021.

Journal Papers (submitted)

3. **L. Tziovani**, L. Hadjidemetriou, and S. Timotheou, “Successive convexification algorithms for optimizing power systems with energy storage models," submitted to *IEEE Transactions on Smart Grid* (Feb. 2023).

4. **L. Tziovani**, L. Hadjidemetriou, and S. Timotheou, “Optimizing the Bidding Strategy of RES Producers in Electricity Markets Under Uncertainty and Battery Degradation," submitted to *IEEE Transactions on Energy Markets, Policy and Regulation* (March 2023).

Conference Papers

5. **L. Tziovani**, L. Hadjidemetriou, and S. Timotheou, "Investigating Piecewise Linear Energy Storage Models for Optimization in Power Systems," *2023 IEEE Power and Energy Society General Meeting (PESGM)*, Orlando, Florida, USA, 2023, pp. 1-5 (accepted).

6. **L. Tziovani**, M. Asprou, I. Ciornei, P. Kolios L. Hadjidemetriou, A. Lazari, R. Tapakis and S. Timotheou, "Long-Term Unit Commitment With Combined-Cycle Units," *2023 IEEE PES PowerTech*, Belgrade, Serbia, 2023, pp. 1-6 (accepted).

7. **L. Tziovani**, L. Hadjidemetriou, and S. Timotheou, "Energy Storage Arbitrage and Peak Shaving in Distribution Grids Under Uncertainty," *2022 IEEE PES Innovative Smart Grid Technologies Conference Europe (ISGT-Europe)*, Novi Sad, Serbia, 2022, pp. 1-5.

8. **L. Tziovani**, L. Hadjidemetriou, and S. Timotheou, "Energy Scheduling of Wind-Storage Systems Using Stochastic and Robust Optimization," *2022 IEEE Power and Energy Society General Meeting (PESGM)*, Denver, CO, USA, 2022, pp. 1-5.

9. **L. Tziovani**, L. Hadjidemetriou, C. Charalampous, S. Timotheou and E. Kyriakides, "Modelling and energy management of a flywheel storage system for peak shaving applications," *2020 IEEE PES Innovative Smart Grid Technologies Europe (ISGT-Europe)*, Hague, Netherlands, 2020, pp. 774-778.

10. I. Papayiannis, M. Asprou, **L. Tziovani** and E. Kyriakides, "Enhancement of Power System Flexibility and Operating Cost Reduction Using a BESS," *2020 IEEE PES Innovative Smart Grid Technologies Europe (ISGT-Europe)*, Hague, Netherlands, 2020, pp. 784-788.

11. **L. Tziovani**, M. Savva, M. Asprou, P. Kolios, E. Kyriakides, R. Tapakis, M. Michael, C. Hadjilaou, "Assessing the Operational Flexibility in Power Systems with Energy Storage Integration," Németh B., Ekonomou L. (eds) Flexitranstore. ISH 2019. *Lecture Notes in Electrical Engineering*, vol 610, Springer, Cham, 2020.

12. **L. Tziovani**, P. Kolios, L. Hadjidemetriou and E. Kyriakides, "Grid Friendly Operation of a PV-Storage System with Profit Maximization and Reliability Enhancement," *2019 IEEE International Conference on Smart Energy Systems and Technologies (SEST)*, Porto, Portugal, 2019, pp. 1-6.

13. L. Zacharia, **L. Tziovani**, M. Savva, L. Hadjidemetriou, E. Kyriakides et al., "Optimal Energy Management and Scheduling of a Microgrid in Grid-Connected

and Islanded Modes," *2019 IEEE International Conference on Smart Energy Systems and Technologies (SEST)*, Porto, Portugal, 2019, pp. 1-6.

14. **L. Tziovani**, P. Kolios, L. Hadjidemetriou and E. Kyriakides, "Energy scheduling in non-residential buildings integrating battery storage and renewable solutions," *2018 IEEE International Energy Conference (ENERGYCON)*, Limassol, Cyprus, 2018, pp. 1-6.

TABLE OF CONTENTS

List of Figures

List of Tables

Abbreviations and Acronyms

RES	Renewable energy sources
PV	Photovoltaic
DER	Distributed energy resources
DSO	Distribution System Operator
TSO	Transmission System Operator
ESS	Energy storage system
FESS	Flywheel energy storage system
BESS	Battery energy storage system
UC	Unit commitment
PSEA	Peak shaving and energy arbitrage
LP	Linear programming
QP	Quadratic programming
QCQP	Quadratically constrained quadratic programming
SOCP	Second-order cone programming
MIP	Mixed-integer programming
MILP	Mixed-integer linear programming
MIQP	Mixed-integer quadratic programming
MISOCP	Mixed-integer second-order cone programming
MIQCQP	Mixed-integer quadratically constrained quadratic programming
MPC	Model predictive control

MOO	Multi-objective optimization
SoC	State-of-charge
SOS-1	Type 1 special ordered set
SOS-2	Type 2 special ordered set
HV	High voltage
MV	Medium voltage
LV	Low voltage
CEMC	Centralized energy management and control scheme
SC	Self-consumption scheme
AC	Alternating current
GC	Grid-level controller
NBI	Normal boundary intersection
LAN	Local area network
RMSE	Root mean squared error
VPN	Virtual private network
MQTT	Message queuing telemetry transport
EP	Expansion planning
DoD	Depth-of-discharge
DA	Day-ahead
ADMM	Alternating direction method of multipliers

Notation

$\mathbf{R}$	Real numbers
$\mathbf{R}^n$	Real n-vectors ($n \times 1$ matrices)
$\mathbf{R}^{m \times n}$	Real $m \times n$ matrices
$\mathbf{Z}$	Integers
$\mathbf{S}_+^n$	Symmetric positive semidefinite matrix
$\|\|x\|\|_2$	Euclidean norm of vector x

Chapter 1

Introduction

1.1 Background and motivation

The increasing penetration of renewable energy sources (RESs) into the power system supports the reduction of carbon dioxide emissions towards a climate neutral economy. Figure 1.1 depicts the growth in renewable power capacity from 2010 to 2021, where the total power capacity worldwide has increased from 1150 to 2963 GW [1]. As can be observed in the figure, there is a fast growth in wind and solar energy compared to other sources such as hydropower, bioenergy and geothermal energy. Hence, wind power and photovoltaics (PVs) are the fastest-growing renewable energy technologies and this trend is expected to continue, as the European Union has set a target to become climate-neutral by 2050 [2].

A large RES penetration into the power system, in particular from PVs and wind power, can cause several challenges to Distribution System Operators (DSOs) and Transmission System Operators (TSOs) for the safe, reliable and efficient operation of the system mainly due to the uncontrollability of RES generation. Specifically, the high renewable generation from PV and wind power plants can cause the following problems at the distribution and transmission levels.

Distribution level: The intermittency of the renewable generation along with the variation of the local load demand can cause the switching between direct and reverse power flow in the distribution grid. A reverse power flow occurs when the distributed generation exceeds the local load demand, resulting in a flow of power back towards the substation. For example, Figure 1.2 shows 24 net-load[1]

[1]The net-load demand is defined as the system load demand minus the RES generation.

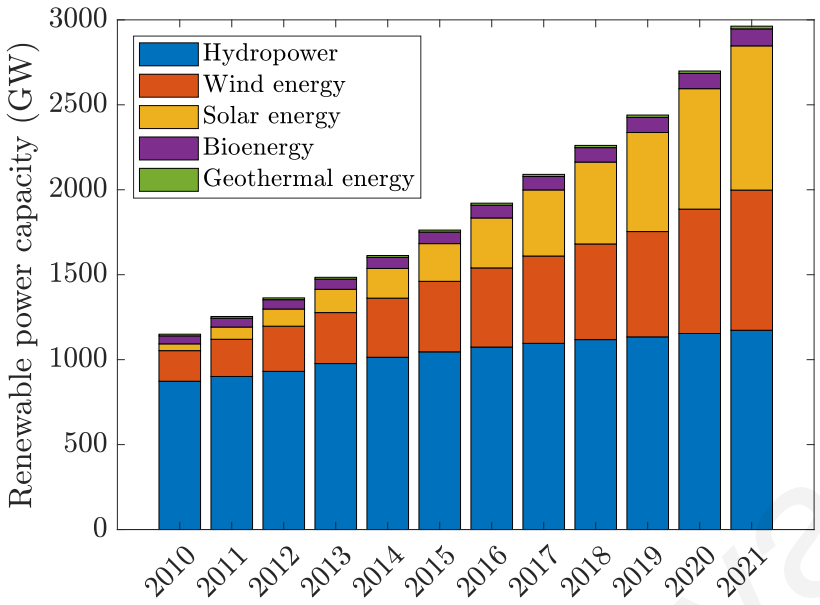

Figure 1.1: Renewable power capacity growth by energy source.

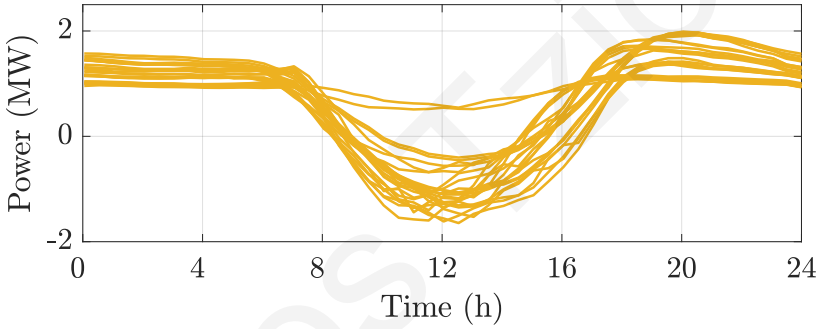

Figure 1.2: Net-load curves of a real distribution grid that present high reverse (negative values) and direct (positive values) power flows.

curves constructed from historical data of a real distribution grid, obtained from a substation in Larnaca region, Cyprus, as provided by the Cyprus DSO. As shown by the net-load curves, high reverse and direct power flows are present during the noon and evening hours due to intense generation by RES and high load demand, respectively. This phenomenon causes high voltage fluctuations or even voltage violations, makes the power equipment to operate near its power limits, and creates high energy losses, leading to stability and power quality issues, equipment failures, and inefficient grid operation [3–5].

Transmission level: Having a high share of RES in the energy generation mix can negatively affect the scheduling and operation of conventional generation. Figure 1.3 demonstrates the total load demand, as well as the conventional, wind and PV generation of the power system of Cyprus for two consecutive days, 10-11/03/2023 [6]. The conventional generation, or net load, is the result of the subtraction of the PV and

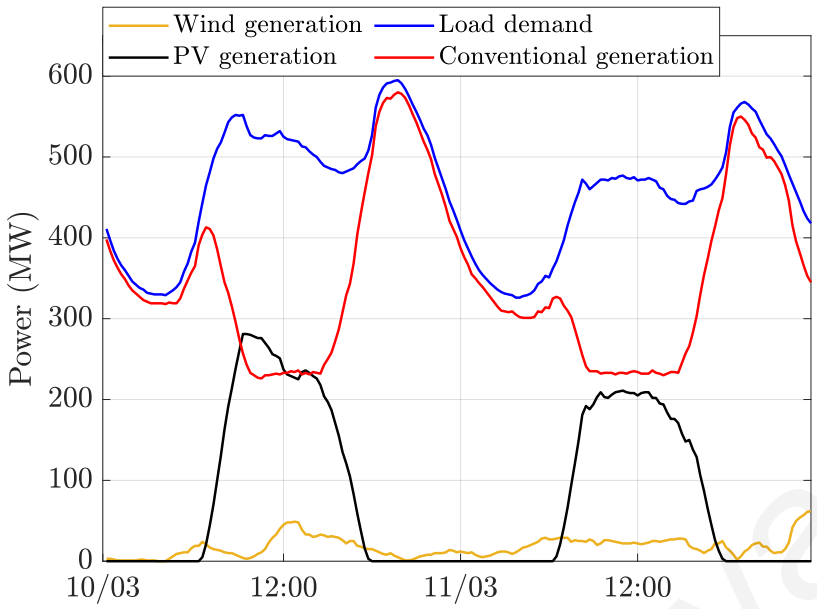

Figure 1.3: Impact of renewable generation on the conventional generation: The case of the power system of Cyprus for 10-11/03/2023.

wind generation from the load demand. The figure indicates that the RES generation increases the difference and steepness between minimum and maximum power that the conventional units must provide, compared to the smoothest and predictable load demand curve. As a result, the non-smooth net-load curve leads to (a) more frequent start-ups/shut-downs of the conventional units, (b) the provision of higher operating reserves, and (c) the requirement for higher operational flexibility in order to ensure the power balance between generation and demand. In addition, RES curtailments from wind and PV plants are often necessary to ensure the minimum stable generation level (>200 MW) of the conventional generation. Therefore, the high RES penetration into the power system can (i) lead to an inefficient operation of conventional generation, (ii) reduce the profit of RES producers when RES curtailments are applied, and (iii) threaten the safe and reliable operation of the system, increasing the risk of a possible blackout [7–9].

The negative effects of the high RES penetration can be compensated using energy storage systems (ESSs), which is an emerging technology that can be used in both distribution and transmission level. In general, ESSs can provide several functionalities in the electricity sector including [10–12]:

- **Grid services**: ESSs can provide services to the power grid, e.g., frequency control, energy shifting, and peak shaving, in order to support the grid under an increasing RES penetration. For example, ESSs can store the energy produced

by RES and use it to avoid the overloading of a distribution transformer during high load demand (peak shaving).

- **Residential prosumers and large RES producers**: The climate and energy strategy for the growth of the RES capacity, mainly from PVs and wind power plants, along with the evolution of electricity markets create new opportunities for RES owners to manage the energy produced by RES in order to reduce their electricity bills or increase their profits. Specifically, the RES owners can store and use the energy produced by RES for their own needs (self-consumption application), or can manage their energy consumption and generation with the aim to absorb and inject power to the grid when the electricity prices are low and high, respectively (time-of-use application).

- **Off-grid applications**: Approximately 940 million people worldwide do not have access to electricity, especially in rural areas [13]. Moreover, remote farms and mines are often not connected to the grid and rely on the use of diesel generators to produce power; however, diesel generators are noisy, pollutant and vulnerable to fluctuating diesel prices. The usage of PV-ESSs systems can support the electricity needs of these areas, providing electricity autonomy and avoiding the usage of diesel generators.

As depicted in Table 1.1, the main ESSs technology types are the pumped hydro storage, thermal storage, electro-chemical batteries and electro-mechanical storage. These technologies are further divided in sub-technology types; for example, the lithium-ion battery energy storage systems (BESSs) and the flywheel energy storage systems (FESSs) are subcategories of electro-chemical batteries and electro-mechanical storage, respectively [10]. Different storage technologies are suitable for specific applications, depending on their characteristics in relation to efficiency, standby losses, charging/discharging power capabilities and expected lifetime. The suitability of three main ESSs technologies, pumped hydro, lithium-ion battery and flywheel, for different power system applications is illustrated in Table 1.2 [10, 11]. Although the lithium-ion battery is applicable in a wide variety of applications compared to other ESSs technologies, only the 5.5% (10.19 GW) of the total electricity storage capacity (185.3 GW) was from electro-chemical batteries for the year 2020. Specifically, the pumped hydro was the dominant ESSs technology with an installed capacity of 92.3% (171 GW), while the flywheel capacity was 0.3% (0.55 GW) [10].

Table 1.1: The main electricity storage technologies

Technology type	Sub-technology type
Electro-chemical	**Lithium-ion battery, lead-acid battery, flow battery, capacitor**
Electro-mechanical	**Flywheel, compressed air storage**
Pumped hydro storage	**Closed-loop or open-loop pumped hydroelectricity storage**
Thermal storage	**Molten salt thermal storage, chilled water thermal storage**

Table 1.2: Possible applications for three main ESSs technologies

	Frequency containment reserve	**Frequency restoration reserve**	**Energy shifting and load levelling**	**Peak shav.**	**Self-cons.**	**Time-of-use**	**Off-grid**
Pumped hydro		✓	✓				
Lithium-ion battery	✓	✓	✓	✓	✓	✓	✓
Flywheel	✓			✓			

The total electricity storage capacity is expected to growth in order to enable an increased and effective RES integration; however, the expansion of the pumped hydro is limited due to environmental constraints. Therefore, the electricity storage capacity from other ESSs technologies, especially from electro-chemical batteries, is expected to rapidly grow. This is attributed to the steep cost reduction of lithium-ion batteries from 1100 to 137 $/KWh over the period 2010-2021, as shown in Figure 1.4 [14, 15].

The effective integration of different RESs and ESSs technologies, termed also distributed energy resources (DER), into the power distribution or transmission system requires the development of optimization schemes to enable their optimized operation. The main aim of this PhD thesis regards the solution of optimization problems associated with the management of distributed energy resources in power systems with high RES and ESS penetration. Such problems are challenging because they require fast and optimal or close-to-optimal solutions, and often involve

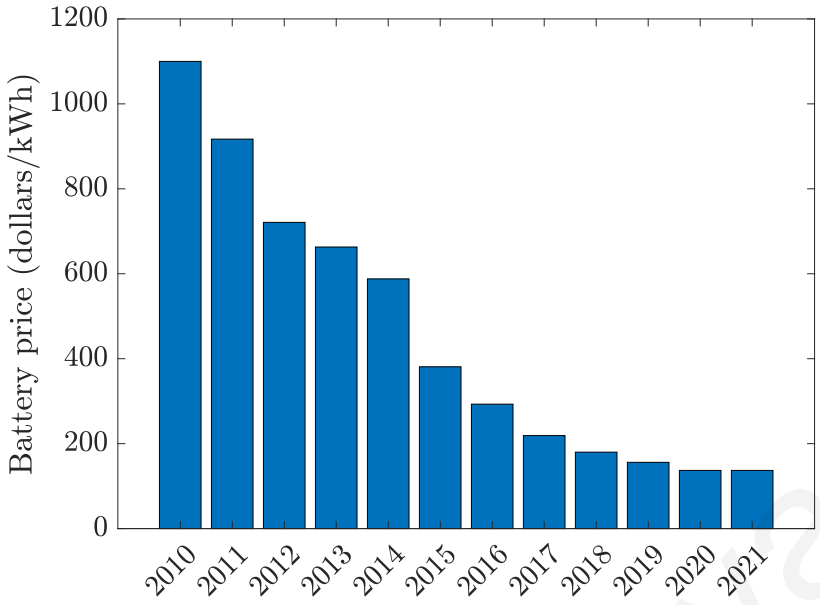

Figure 1.4: Average lithium-ion battery prices ($/kWh) for 2010-2021.

modelling inaccuracies and RES uncertainty. In this context, the following problems are considered: (i) optimization of general energy management problems in power systems involving non-convex ESS models, (ii) energy management of photovoltaic and battery storage systems in active distribution grids, (iii) energy management of a flywheel storage system for peak shaving applications, and (iv) stochastic optimization of the bidding strategy of RES producers in electricity markets considering battery degradation.

The common objective of the considered optimization problems is to minimize the operating cost, or maximize profits, while ensuring the safe, reliable and efficient operation of the power system. The examined problems have a number of common challenging characteristics that should be addressed by any developed optimization scheme:

- **Real-Time Decision-Making**: The best decisions regarding the operation and control of the system should be made and executed repeatedly in a short time-frame, in order to ensure the reliable system operation. These decisions can be the ESSs or RES power coordination set-points. Therefore, any developed optimization scheme should make the best possible decisions within a short time-frame using all available input data, including real-time measurements, as well as historical and predicted data.

- **Hard Problems**: The considered problems are non-convex optimization prob-

lems which are challenging to solve, especially for large scale systems. It is almost sure that these problems cannot be optimally solved with polynomial algorithms. The time needed to solve non-convex problems increases exponentially as the problem size expands, while high-accuracy solutions are not always guaranteed. Hence, the developed optimization schemes should be solved fast and reliably, providing optimal or close-to-optimal solutions.

- **Modelling Inaccuracy**: The simplifications and assumptions that are applied to model the physical system, along with the uncertain parameters of the derived models, introduce modelling errors that can affect the reliability and cost-effectiveness of the system. For example, an inaccurate ESS model can lead to a wrong estimation of the ESSs state-of-charge, leading to wrong decisions during the operation of the power system. Therefore, modelling errors should be considered by the developed optimization schemes to avoid any undesirable operation of the system.

- **Uncertainty**: Although forecasting techniques have been considerably improved over the last decade, prediction of the PV or wind generation is far from perfect. In addition, the prediction error increases significantly as the prediction horizon increases. Similar to modelling errors, prediction errors can lead to wrong and undesirable decisions during the system operation. As a result, the developed optimization schemes should handle well prediction errors associated with the PV or wind generation, load consumption, and energy market prices, generating reliable and cost-effective solutions.

- **Multiple Objectives**: In many problems, there are multiple objectives that should be simultaneously minimized or maximized. The objectives in the considered problems are conflicting, which implies that an improvement in one objective deteriorates the other objectives. Hence, the developed optimization schemes should consider multiple objectives and provide the best trade-off solution for the system operation.

1.2 Review of examined problems

In this thesis we will examine four different optimization problems for the management of distributed energy resources in power systems, which are associated with the aforementioned challenging characteristics.

- *Optimization of general energy management problems in power systems involving non-convex ESS models*:

  The increasing utilization of ESSs in power system applications necessitates the use of mathematical models for their representation in power system optimization problems. Different ESS models have been proposed that utilize non-convex constraints to represent the ESS power losses, e.g., using piecewise linear and quadratic loss functions, resulting in non-convex optimization problems. To reduce the complexity, convex relaxation models are often derived but generate infeasible solutions when the relaxation exactness is violated. This problem aims to develop a fast and effective methodology for optimizing general energy management problems in power systems involving non-convex ESS models.

- *Energy management of photovoltaic and battery storage systems in active distribution grids*: This problem considers the operation of an active distribution grid with prosumers[2] by managing the PVs and BESSs, integrated in the buildings. The objectives are to minimize (i) the prosumers electricity cost and (ii) the cost of the grid energy losses, while guaranteeing safe and reliable grid operation through the power flow constraints. This can be done by determining the active and reactive power set-points of the PVs and BESSs. The power flow constraints are non-linear, non-convex and along with the BESSs complementarity constraints make the problem hard to solve. The PV uncertainty and BESSs modelling inacuracies challenge the efficient operation of the system, while the two conflicting objectives impose the need of selecting an operating point that provides a fair trade-off between the prosumers and the grid costs.

- *Energy management of a flywheel storage system for peak shaving applications*: Peak shaving services provided by energy storage systems enhance the utilization

[2]Prosumers are users who consume and produce energy.

of existing grid infrastructure to accommodate the increased penetration of renewable energy sources and the load demand growth. This problem considers the provision of peak shaving services from a flywheel energy storage system installed in a transformer substation. The objectives are to (a) eliminate the direct and reverse power flow violations of a distribution transformer using a FESS and (b) minimize the FESS power losses for a cost-effective operation of the distribution grid by optimizing the energy schedule of the FESS. The nonlinear, and non-convex nature of the FESS model challenges the solution of the considered problem. In addition, the net-load uncertainty of the distribution grid along with the FESS modelling inaccuracy can lead to power violations of the transformer during the real operation, threatening the safety of the grid infrastructure.

- *Stochastic optimization of the bidding strategy of RES producers in electricity markets considering battery degradation*: RES producers who participate in day-ahead electricity markets are paid for their scheduled RES production profile submitted to the market for the next day based on variable day-ahead prices. However, as the day-ahead prices are unknown, producers must make decisions based on forecasted prices, which may reduce their profits in case of high forecasting errors. In addition, forecasting errors in RES power generation create power imbalances in real operation that threaten the stability of the power system. These imbalances can result in power deficits, which are penalized at higher costs compared to the day-ahead prices, or power excesses, which are paid at lower prices. This incentivizes RES producers to submit accurate scheduled production profiles to the day-ahead market to maximize their profits. This problem considers the development of a bidding strategy for RES-BESS producers to maximize their expected profits by buying and selling power in electricity markets, considering battery degradation and power limits of the grid due to transmission congestion. The main challenges of the considered problem are associated with the uncertainty in RES power generation, day-ahead energy prices, and imbalance prices, which can deteriorate the producer's profits in case of high prediction errors. Furthermore, the non-convex degradation and ESS models make the problem hard to solve.

1.3 Summary of contributions

Overall, this thesis makes several contributions to the field of power systems and their optimization in ensuring safe, reliable, and efficient operation. In particular, the thesis formulates and solves four important problems, described in Section 1.2, related to the optimization and management of distributed energy resources in power systems with high RES and ESS penetration. In addressing these problems, this thesis develops multiple novel optimization methods that yield high-quality and fast solutions in the presence of modelling inaccuracies and information uncertainties. The specific contributions of this PhD thesis are summarized below.

- Development of a solution methodology that deals with violations of the relaxed ESS constraints in general energy management problems in power systems involving non-convex ESS models. Specifically, a general successive convexification algorithm is developed that yields fast and high-quality feasible solutions considering general ESS power loss functions, e.g., piecewise linear and quadratic loss functions. Furthermore, a second specialized successive convexification algorithm is developed that enhances the solution quality and execution speed when piecewise-linear loss functions are used. The performance of the proposed algorithms is investigated by considering two optimization problems in power systems that incorporate ESSs: (a) the *Unit Commitment* and (b) the *Peak Shaving and Energy Arbitrage*.

- Development of a centralized energy management and control scheme (CEMC) for managing the PV-BESSs operation in active distribution grids. The CEMC scheme minimizes both the prosumers electricity cost and the grid energy losses cost, while ensuring reliable grid operation by incorporating power flow constraints and reactive power support. A convex multi-objective second-order cone program (SOCP) to fast and reliably solve the considered optimization problem by relaxing the non-convex constraints is formulated. The SOCP model yields optimal solutions under most operating conditions; however, non-exact solutions are generated under "extreme" operating conditions. To deal with this issue, a solution algorithm that ensures feasibility of the relaxed SOCP model under all operating conditions is developed. Furthermore, a second algorithm that finds the operating point that provides fairness between

the prosumers and grid losses costs is proposed.

- Development of an energy management scheme for providing peak shaving services using a flywheel storage system. Towards this direction, FESS power losses and maximum power functions are constructed to be dependent on parameters that are readily available through commercial FESS interfaces (charging/discharging power and SoC). Moreover, the derived FESS functions are modelled with convex constraints that enable the formulation of convex optimization problems. The derived FESS functions are used to develop a new optimization formulation for the peak-shaving problem that minimizes the transformer power limit violations and FESS power losses in a lexicographic fashion. Furthermore, a two-level hierarchical control scheme is developed to solve the peak-shaving problem fast and reliably, while handling prediction errors and modelling inaccuracies. For the experimental evaluation of the proposed control scheme, a software platform is developed for managing smart grid configurations and utilized for the integration of a prototype FESS system into a smart-grid testbed. In addition, model validation and parameter identification is experimentally performed for the prototype FESS.

- Development of an optimization scheme for the bidding strategy of RES-BESS producers in electricity markets considering battery degradation and uncertainty in RES generation and electricity prices. Specifically, the bidding strategy is developed as a linear deterministic optimization formulation that deals with the non-convexities arising from the degradation and power loss models of the BESS by incorporating an approximate cycle-based degradation model and a relaxed BESS model. In addition, the bidding strategy is developed as a scenario-based stochastic optimization formulation that handles uncertainty in RES power generation, day-ahead prices, and imbalance prices. The stochastic scheme is formulated as a linear program, which can be fast and reliably solved under a large number of scenarios. The proposed bidding strategy is investigated in two different RES-BESS plants, a wind-BESS and PV-BESS plant, using real data.

1.4 Thesis outline

The remainder of this thesis is organised as follows. In Chapter 2 we introduce the main optimization methods used in this thesis for the management of distributed energy resources in power system operation. First, an introduction to optimization problems is given by (a) stating mathematically an optimization problem, (b) providing the properties of a convex optimization problem and (c) classifying the optimization problems in different mathematical programming types. Second, an introduction to multi-objective optimization problems is given by (a) stating mathematically a multi-objective optimization problem, (b) elaborating on the conflicting objectives and demonstrating the Pareto front, and (c) presenting different multi-objective methods. Third, the model predictive control method that is often used to control a system while in operation is described. Finally, the scenario-based stochastic optimization approach that is used to make decisions under uncertainty is presented.

Chapter 3 examines the *optimization of general energy management problems in power systems involving non-convex ESS models* problem. In this chapter, we begin by discussing the motivation of using relaxed ESS models in optimization formulations and elaborating on the issue of the ESS relaxation violation. Then, we present the general mathematical model for ESS, followed by two optimization formulations that incorporate the exact and relaxed ESS models, respectively. Next, we define the exact and relaxed versions of the piecewise linear and quadratic ESS models. To overcome the issue of ESS relaxation violation, we develop two convexification algorithms that generate fast and high-quality feasible solutions. The first algorithm handles general ESS loss functions, while the second specialized algorithm enhances the algorithm performance when piecewise-linear loss functions are used. The two algorithms are applied in two different optimization problems in power systems, the *Unit Commitment* and *Peak Shaving and Energy Arbitrage* problems, to investigate their performance considering piecewise-linear and quadratic ESS loss functions. Simulation results demonstrate the impact of the ESSs relaxation violation on the actual system operation and validate the algorithms efficacy to generate high-quality feasible and even optimal solutions with significantly lower execution times compared to problems utilizing exact ESS models.

In Chapter 4 we investigate the *energy management of photovoltaic and battery stor-*

age systems in active distribution grids problem. We start with the introduction and the literature review of the problem, followed by a description of the system architecture and the mathematical formulation of the considered problem. In detail, a centralized multi-objective optimization model to minimize (i) the prosumers electricity cost and (ii) the cost of the grid energy losses, while guaranteeing safe and reliable grid operation is formulated. Then, in the solution methodology we (a) formulate a convex multi-objective SOCP optimization model to solve fast and reliably the considered optimization problem by relaxing the non-convex constraints, (b) develop an algorithm to ensure feasibility of the relaxed SOCP model under all operating conditions and (c) propose a second algorithm to find the operating point that minimizes the absolute difference between the objective gain losses. Simulation results demonstrate the superiority of the proposed optimization scheme in managing an industrial distribution grid compared to a self-consumption approach.

Chapter 5 studies the *energy management of a flywheel storage system for peak shaving applications* problem. First, we discuss the motivation for the solution of this problem followed by a description of related research topics. Then we describe the problem as a lexicographic optimization problem that aims to define the flywheel power set-points by minimizing the transformer power limit violations and the flywheel energy losses. Convex functions that represent the flywheel power losses and its maximum power are derived and integrated in the proposed scheme. We also introduce a two-level hierarchical control framework to operate the transformer-flywheel-system in a way that handles prediction errors and modelling inaccuracies. At the higher level, a model predictive controller is developed that solves the lexicographic optimization scheme using linear programming. At the lower-level, a secondary controller corrects the power set-points of the model predictive controller using real-time measurements. A software platform has been developed for integrating the proposed controllers in an experimental setup to test their effectiveness in a realistic testbed setting, and the flywheel system characteristics are experimentally identified. Finally, simulation and experimental results validate and verify the modelling, identification, control and operation of a real flywheel system for peak shaving services.

Chapter 6 examines the *stochastic optimization of the bidding strategy of RES producers in electricity markets considering battery degradation* problem. We start with the introduction and the literature review of the problem, followed by the statement of

the considered problem. Specifically, we (a) describe the constraints of the RES-BESS plant, (b) present the cycle-based degradation model, (c) introduce the framework of the considered electicity markets, and (d) formulate the optimization problem of the bidding strategy while considering the RES-BESS constraints, degradation model, and electricity market structure. To address the non-convexities associated with the BESS, a linear deterministic optimization scheme is developed that incorporates an approximate cycle-based degradation model and a relaxed BESS model. To handle uncertainties in RES power generation, day-ahead energy prices, and imbalance prices, a scenario-based linear stochastic optimization scheme is developed that can be fast and reliably solved. Simulation results evaluate the effectiveness of the stochastic scheme in improving the profits of wind-BESS and PV-BESS producers compared to the corresponding deterministic scheme.

Chapter 7 provides a summary of the work conducted in this PhD thesis and serves as the concluding chapter. Additionally, Chapter 8 proposes future research directions.

Chapter 2

Optimization methods

This chapter introduces the main optimization methods used in this thesis for the management of distributed energy resources in power systems. The structure of the chapter is as follows. Section 2.1 (a) states mathematically an optimization problem, (b) provides the properties of a convex optimization problem, (c) explains the role of convex relaxation in non-convex problems and (d) classifies the optimization problems in different mathematical programming types. In Section 2.2, an introduction to multi-objective optimization problems is given by (a) stating mathematically a multi-objective optimization problem, (b) elaborating on the conflicting objectives and demonstrating the Pareto front, and (c) presenting different methods for solving multi-objective optimization problems. Section 2.3 describes the model predictive control method that is used to control a system during the operation process. Finally, the scenario-based stochastic optimization approach that is used to make decisions under uncertainty is presented in Section 2.4.

2.1 Optimization problems

Optimization is the process of achieving the best outcome by taking decisions under given circumstances. The goal of all such decisions is either to minimize effort, cost or to maximize benefit, profit, etc. These objectives can be usually expressed as a function of certain design variables; thus, optimization is the act of finding the conditions that minimize or maximize the considered objective functions, satisfying the design constraints. The design constraints may represent physical and operating limitations of a system [16].

2.1.1 Statement of an optimization problem

An optimization, or mathematical programming problem can be stated as [16, 17]
Find

$$\mathbf{x} = (x^1, x^2, ..., x^n) \tag{2.1}$$

which minimizes

$$f(\mathbf{x}) \tag{2.2}$$

subject to the constraints

$$g_j(\mathbf{x}) \leq 0, \quad j = 1, ..., J \tag{2.3}$$

$$l_i(\mathbf{x}) = 0, \quad i = 1, ..., I \tag{2.4}$$

where vector $\mathbf{x} = (x^1, x^2, ..., x^n)$ is the design variable of the problem, $f(\mathbf{x})$ is the objective function, $g_j(\mathbf{x})$ and $l_i(\mathbf{x})$ are the inequality and equality constraints, respectively. Alternatively, the optimization problem (2.1) - (2.4) can be stated as

$$\begin{aligned} &\text{minimize} && f(\mathbf{x}) \\ &\text{subject to} && g_j(\mathbf{x}) \leq 0, \quad j = 1, ..., J, \\ &&& l_i(\mathbf{x}) = 0, \quad i = 1, ..., I. \end{aligned} \tag{2.5}$$

A point $\mathbf{x}$ is feasible if it satisfies the constraints, $g_1(\mathbf{x}) \leq 0, ..., g_J(\mathbf{x}) \leq 0$ and $l_1(\mathbf{x}) = 0, ..., l_I(\mathbf{x}) = 0$, while Problem (2.5) is feasible if there exists at least one feasible point, and infeasible otherwise. The set of all feasible points is called the feasible region or feasible set. If $\mathbf{x}$ is feasible, then the jth inequality constraint is active or

binding when $g_j(\mathbf{x}) = 0$ and inactive otherwise ($g_j(\mathbf{x}) < 0$), while equality constraints are always active. A point $\mathbf{x}^*$ is called optimal, or the solution of the optimization problem (2.5), if it is feasible and has the smallest objective value among all points that satisfy the constraints, such that for any $\mathbf{z}$ with $g_1(\mathbf{z}) \leq 0, ..., g_J(\mathbf{z}) \leq 0$ and $l_1(\mathbf{z}) = 0, ..., l_I(\mathbf{z}) = 0$, we have $f(\mathbf{x}^*) \leq f(\mathbf{z})$.

Optimization problems that aim to maximize a function $f(\mathbf{x})$ can be stated in the form of Problem (2.5) by minimizing the function $-f(\mathbf{x})$. This is because if a point $\mathbf{x}^*$ corresponds to the minimum value of a function $-f(\mathbf{x})$, then the same point corresponds to the maximum value of the function $f(\mathbf{x})$.

In general, there are families or classes of optimization problems, characterized by particular forms of the objective and constraint functions as well as the types of the quantitative variables, continuous and/or discrete. For example, optimization problem (2.5) is a linear program when the variables are continuous and both objective and constraint functions are linear and a nonlinear program when at least one function is not linear. For some classes of optimization problems there are effective methods for solving them even with hundreds of thousands variables and constraints. However, this is not true for some other classes where the solution of optimization problems with as few as ten variables can be extremely challenging, while larger problems can be intractable [17].

2.1.2 Convex optimization problems

Convex optimization problems is a class of optimization problems where there are very effective methods for solving them. Problem (2.5) is convex if it has the following requirements [17]:

- The objective function $f(\mathbf{x})$ is convex. An example of convex and non-convex functions is demonstrated in Figure 2.1.
- The inequality constraint functions $g_j(\mathbf{x})$ are convex.
- The equality constraint functions $l_i(\mathbf{x})$ are affine[1].

Therefore, in a convex optimization problem, we minimize a convex objective function over a convex set, since its feasible set (feasible region) is convex. An example of a convex and non-convex set is illustrated in Figure 2.2.

[1] A function $l_i(\mathbf{x})$ is affine if it is a sum of a linear function and a constant, i.e., $l_i(\mathbf{x}) = \hat{a}_i^T \mathbf{x} - \hat{b}_i$.

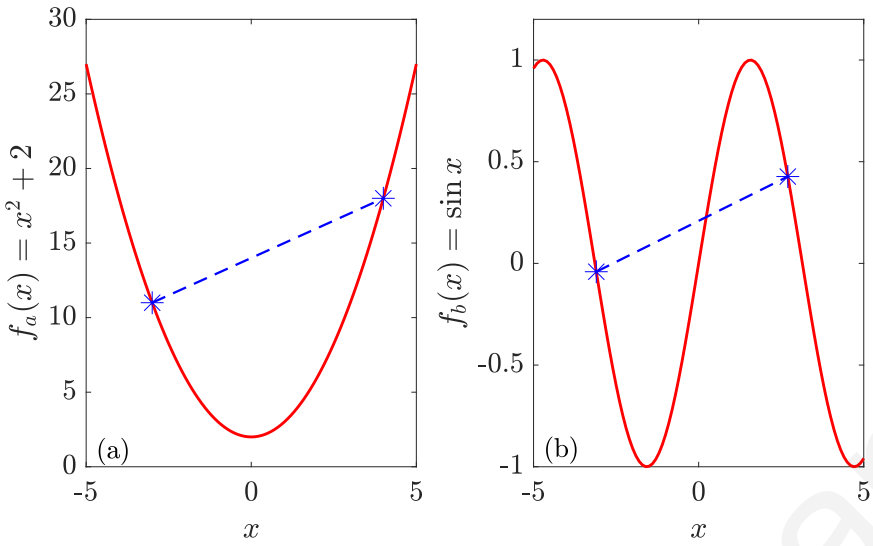

Figure 2.1: Convex and non-convex functions: Function $f_a(x) = x^2 + 2$ is convex because the chord joining any two points on the curve always falls entirely on or above the curve between those two points, while function $f_b(x) = \sin x$ is non-convex.

There are sub-classes of convex optimization problems based on the forms of the objective and constraint functions; however, the three requirements for convex optimization must be satisfied. For example, linear programs are convex since all the objective and constraint functions are linear and hence convex, but for non-linear programs this is not always true.

The challenge, and art, in using convex optimization is in recognizing convex optimization problems, or those that can be transformed to convex optimization problems, and formulating them. Once this formulation is done, solving the problem is straightforward, even for large problems, using optimization solvers which ensure a fast, reliable and optimal solution. In contrast, formulating a practical problem as a general non-convex and non-linear optimization problem is relatively easy; however, solving such a problem is challenging, since there are no effective methods to solve it [17].

2.1.3 The role of convex relaxation in non-convex problems

Convex relaxations are used to replace non-convex constraints with convex constraints and therefore to transform non-convex optimization problems to convex. This can be done by relaxing a non-convex constraint to a looser, but convex, constraint, increasing the feasible set of the original problem. For example, Figure 2.3 depicts the relaxed convex set, C_b, of a non-convex set C_a by taking the smallest

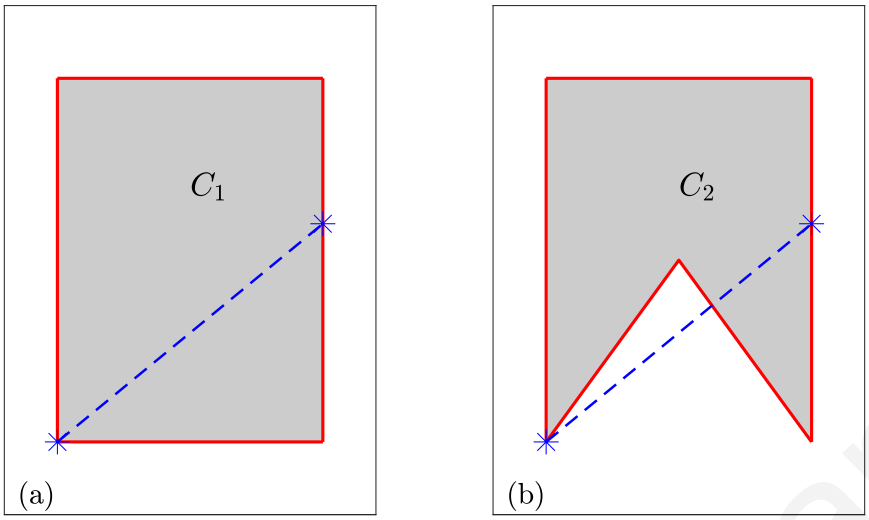

Figure 2.2: Convex and non-convex sets: The feasible set C_1 is convex because the line segment between any two points in C_1 lies in C_1, while the set C_2 is non-convex.

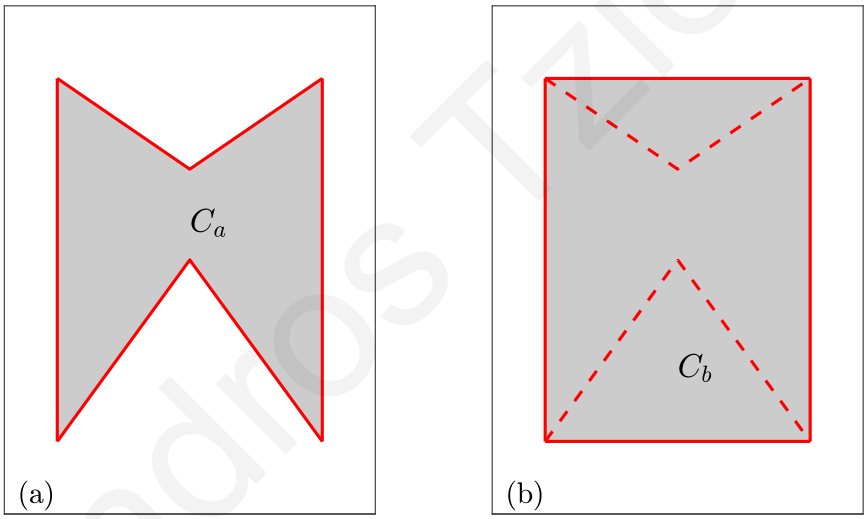

Figure 2.3: Convex relaxation: The non-convex set C_a is relaxed to the convex set C_b by taking the smallest convex set (convex hull) that contains C_a.

convex set (convex hull) that contains C_a, $C_a \subset C_b$. As a result, all possible solutions of the original problem are still feasible for the relaxed problem. Thus, the optimal value of the relaxed problem is (a) optimal for the original problem when the solution is contained in the non-convex set C_a, (also called exact solution), and is (b) a lower bound on the optimal value of the original problem when the solution is not contained in the non-convex set (non-exact solution) [17].

2.1.4 Classification of optimization problems

The classes of optimization problems that are used in this thesis, characterized by particular forms of the objective and constraint functions as well as the types of the variables, are the following:

Linear programming (LP)

Linear programming is the simplest class of optimization problems in which all the objective and constraints functions are affine and all variables are continuous, $\mathbf{x} = (x^1, x^2, ..., x^n) \in \mathbf{R}^n$ [17, 18]:

$$\begin{aligned} &\text{minimize} && \mathbf{c}^T\mathbf{x} \\ &\text{subject to} && \mathbf{a}_j^T\mathbf{x} \leq b_j, \quad j = 1, ..., J, \\ &&& \hat{\mathbf{a}}_i^T\mathbf{x} = \hat{b}_i, \quad i = 1, ..., I, \end{aligned} \tag{2.6}$$

where vectors $\mathbf{c}$, $\mathbf{a}_1, ..., \mathbf{a}_J$, $\hat{\mathbf{a}}_1, ..., \hat{\mathbf{a}}_I \in \mathbf{R}^n$ and scalars $b_1, ..., b_J$, $\hat{b}_1, ..., \hat{b}_I \in \mathbf{R}$ are problem parameters that specify the objective, inequality and equality constraint functions. LP programs are convex and can be solved efficiently and reliably using very effective methods such as, Dantzig's simplex method and more recent interior-point methods [17].

Quadratic programming (QP)

Quadratic programming is a class of non-linear optimization problems in which the objective function is quadratic, the constraints are affine, and all the variables are continuous, $\mathbf{x} \in \mathbf{R}^n$ [17]:

$$\begin{aligned} &\text{minimize} && (1/2)\mathbf{x}^T\mathbf{P}\mathbf{x} + \mathbf{c}^T\mathbf{x} + r \\ &\text{subject to} && \mathbf{a}_j^T\mathbf{x} \leq b_j, \quad j = 1, ..., J, \\ &&& \hat{\mathbf{a}}_i^T\mathbf{x} = \hat{b}_i, \quad i = 1, ..., I, \end{aligned} \tag{2.7}$$

where $\mathbf{P}$ is the Hessian matrix of the objective function, denoting the coefficients of the quadratic term; vector $\mathbf{c} \in \mathbf{R}^n$ denotes the coefficients of the linear term and $r \in \mathbf{R}$ is a constant. QP programs are convex when the objective function is convex which is true when $\mathbf{P} \in S_+^n$, where S_+^n is the set of symmetric positive semidefinite matrices. When convex quadratic inequality constraints are presented along with the convex

quadratic objective function, then the problem is called quadratically constrained quadratic program (QCQP) [17]:

$$\begin{aligned} \text{minimize} \quad & (1/2)\mathbf{x}^T\mathbf{P}_0\mathbf{x} + \mathbf{c}_0^T\mathbf{x} + r_0 \\ \text{subject to} \quad & \mathbf{a}_j^T\mathbf{x} \leq b_j, \quad j = 1, ..., J, \\ & \hat{\mathbf{a}}_i^T\mathbf{x} = \hat{b}_i, \quad i = 1, ..., I. \\ & (1/2)\mathbf{x}^T\mathbf{P}_k\mathbf{x} + \mathbf{c}_k^T\mathbf{x} + r_k \leq 0, \quad k = 1, ..., M, \end{aligned} \tag{2.8}$$

where $\mathbf{P_k} \in \boldsymbol{S}_+^n$, $\mathbf{c_k} \in \mathbf{R}^n$, $r_k \in \mathbf{R}$, $k = 0, 1, ..., M$. Convex QP and QCQP programs can be solved efficiently using interior-point methods [17].

Second-order cone programming (SOCP)

Second-order cone programming is a class of non-linear, but convex, optimization problems which is a generalization of QP and deals with the following conic constraints [19]:
Quadratic cone:

$$x_1^2 \geq \sum_{j=2}^{n} x_j^2, \quad x_1 \geq 0, \mathbf{x} \in \mathbf{R}^n \tag{2.9}$$

Rotated Quadratic Cone:

$$2x_1x_2 \geq \sum_{j=3}^{n} x_j^2, \quad x_1, x_2 \geq 0, \mathbf{x} \in \mathbf{R}^n \tag{2.10}$$

An SOCP program has the following form [17]

$$\begin{aligned} \text{minimize} \quad & \mathbf{c}^T\mathbf{x} \\ \text{subject to} \quad & \mathbf{a}_j^T\mathbf{x} \leq b_j, \quad j = 1, ..., J, \\ & \hat{\mathbf{a}}_i^T\mathbf{x} = \hat{b}_i, \quad i = 1, ..., I, \\ & \|\mathbf{A}_k\mathbf{x} + \tilde{b}_k\|_2 \leq \tilde{\mathbf{c}}_k^T\mathbf{x} + \tilde{d}_k, \quad k = 1, ..., K, \end{aligned} \tag{2.11}$$

where $\mathbf{x} \in \mathbf{R}^n$, $\mathbf{A}_k \in \mathbf{R}^{n_k \times n}$, $\tilde{\mathbf{c}}_k \in \mathbf{R}^n$, $\tilde{b}_k, \tilde{d}_k \in \mathbf{R}$, $k = 1, ..., K$. When $\tilde{\mathbf{c}}_k = 0$, $k = 1, ..., K$, the SOCP program is equivalent to a QCQP program. SOCP programs can be efficiently solved via specialized interior-point methods.

Mixed-integer programming (MIP)

Mixed-integer programming is a class of non-convex optimization problems that includes both continuous and integer variables:

$$
\begin{aligned}
\text{minimize} \quad & f(\mathbf{x}) \\
\text{subject to} \quad & g_j(\mathbf{x}) \leq 0, \quad j = 1, ..., J, \\
& l_i(\mathbf{x}) = 0, \quad i = 1, ..., I. \\
& x_w \in \mathbf{Z}, \quad w = 1, ..., W,
\end{aligned}
\tag{2.12}
$$

where $W \leq n$ denotes the set of variables that are constrained to be integers. LP, QP, and SOCP programs that include integer variables are called mixed-integer linear programs (MILP), mixed-integer quadratic programs (MIQP), and mixed-integer second-order cone programs (MISOCP), respectively. MIP programs can be used in a wide set of practical applications [20]:

- *Problems with discrete inputs and outputs*. For example, integer variables may be used to represent indivisible goods such as aeroplanes and cars.
- *Problems with logical conditions*. For example, if task A is assigned, then task C must be assigned as well. Integer variables with extra constraints can be used to represent logical conditions.
- *Combinatorial problems*. There are several practical problems that have the characteristic of a very large number of feasible solutions arising from different combinations of allocating items or people to different positions. For example, the unit commitment problem aims to find the feasible set with the committed generating units that minimize the total operational cost for the considered time horizon. In this problem, binary (integer) variables are used to indicate if a generating unit is committed or not.
- *Non-linear and non-convex problems*. For example, a non-linear and non-convex function may be approximated using several linear segments (piece-wise linear approximation) and integer variables. Thus, the original non-linear and non-convex problem may be formulated as an MILP program.

MIP optimization problems can be solved optimally using the branch-and-bound method; however, their execution time increases exponentially as the problem size increases, while large problems may be intractable [20].

2.2 Multi-objective optimization (MOO)

Optimization problems that involve more than one objectives to be optimized simultaneously are called multi-objective optimization problems. There are several practical problems that have several objectives; for example, in automotive design the objectives may be to maximize the performance and minimize the fuel consumption of a vehicle.

2.2.1 Statement of an MOO problem

An MOO problem is expressed as [21]

$$\begin{aligned} \text{minimize} \quad & F(\mathbf{x}) = [f_1(\mathbf{x}), f_2(\mathbf{x}), ..., f_L(\mathbf{x})] \\ \text{subject to} \quad & g_j(\mathbf{x}) \leq 0, \quad j = 1, ..., J, \\ & l_i(\mathbf{x}) = 0, \quad i = 1, ..., I, \end{aligned} \tag{2.13}$$

where $f_1(\mathbf{x}), f_2(\mathbf{x}), ..., f_L(\mathbf{x})$ are the considered objective functions.

In MOO problems the objectives are usually conflicting, thus there is not a single solution point that minimizes all objectives simultaneously. On the contrary, there are multiple Pareto optimal points, which are defined as the solution points where it is not possible to move from that points and improve the value of one objective function without deteriorating the value of another objective function. The set of all Pareto optimal points is called the Pareto front (or Pareto frontier or Pareto set) [21]. Figure 2.4 demonstrates the Pareto front of two conflicting objective functions, $f_1(x)$ and $f_2(x)$, that are minimized simultaneously. The figure indicates the Pareto optimal points that denote a trade-off solution between the objectives. Usually, the trade-off solution point is selected based on the preferences of a human decision maker, e.g., the vehicle manufacturer. However, the selection of a trade-off solution point is challenging in real-time applications, where a point that provides a fair trade-off solution should be always selected during the operation process of a system.

2.2.2 Methods

Weighted-sum

The most widely used method for solving MOO problems is the weighted-sum method, where the optimization problem (2.13) with the multiple objectives is trans-

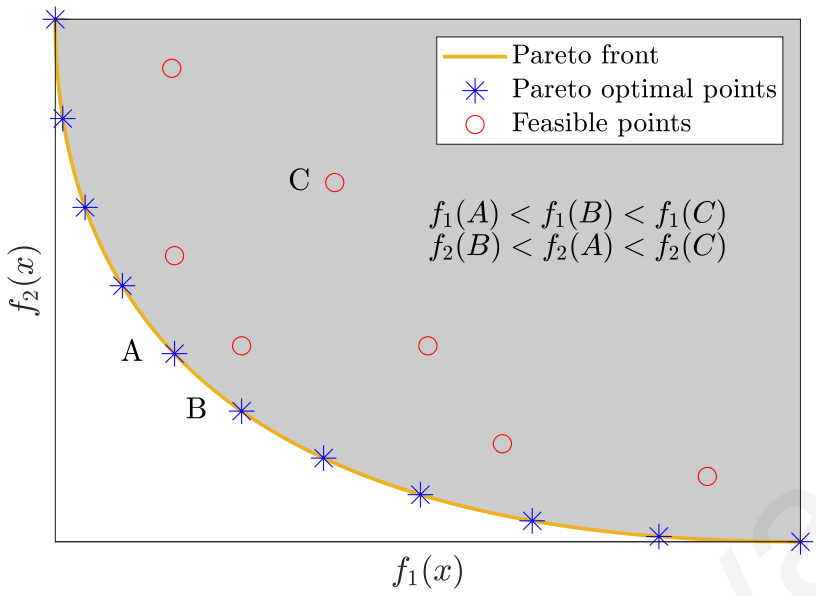

Figure 2.4: The Pareto front of two conflicting objective functions, $f_1(x)$ and $f_2(x)$. Solution points **A** and **B** are Pareto optimal, while **C** is feasible but not optimal.

formed into an aggregated single objective optimization problem [21]:

$$\begin{aligned} \text{minimize} \quad & F(\mathbf{w}) = w_1 f_1(\mathbf{x}) + w_2 f_2(\mathbf{x}), ..., w_L f_L(\mathbf{x}) \\ \text{subject to} \quad & g_j(\mathbf{x}) \leq 0, \quad j = 1, ..., J, \\ & l_i(\mathbf{x}) = 0, \quad i = 1, ..., I, \end{aligned} \tag{2.14}$$

where $\mathbf{w} = [w_1, w_2, ..., w_L]$, $\sum_{l=1}^{L} w_l = 1$ are the weighting parameters that control the trade-off between the objectives. Specifically, different Pareto optimal points are obtained for different values of $\mathbf{w}$.

Lexicographic optimization

The lexicographic method is used to solve multi-objective optimization problems considering that the objective functions can be ranked according to their importance, instead of assigning weights. Specifically, in lexicographic optimization L objective functions, $f_l(\mathbf{x}), l = 1, ..., L$, are to be optimized on a feasible set $\mathbf{x} \in \mathcal{X}$ in a *lexicographic order* such that $f_l(\mathbf{x})$ has higher priority than $f_{l+1}(\mathbf{x})$ [22]. This means that low priority objectives are optimized as far as they do not affect the optimization of higher priority objectives. Let us denote the L-objective lexicographic optimization problem by

$$\begin{aligned} \text{lexmin} \quad & \{f_1(\mathbf{x}),\ f_2(\mathbf{x}), ..., f_L(\mathbf{x})\} \\ \text{subject to} \quad & \mathbf{x} \in \mathcal{X}, \end{aligned} \tag{2.15}$$

where the feasible set $\mathbf{x} \in \mathcal{X}$ is defined by the inequality and equality constraints $g_1(\mathbf{x}) \leq 0, ..., g_J(\mathbf{x}) \leq 0$ and $l_1(\mathbf{x}) = 0, ..., l_I(\mathbf{x}) = 0$. Optimizing problem (2.15) requires the solution of L optimization subproblems with the lth one defined as

$$\begin{aligned} \text{minimize} \quad & f_l(\mathbf{x}) && (2.16) \\ \text{subject to} \quad & f_m(\mathbf{x}) \leq f_m(\mathbf{x}_m^*), \quad m = 1, ..., l-1, && (2.17) \\ & \mathbf{x} \in \mathcal{X}, \end{aligned}$$

where $\mathbf{x}_m^*$ denotes the optimal solution of the m-th subproblem. Then, the optimal solution to problem (2.15) is $\mathbf{x}_L^*$, which is also a Pareto optimal point.

2.3 Model predictive control

Model predictive control (MPC) is an advanced method of process control that is used to control a process or plant [23, 24]. As shown in Figure 2.5, the MPC method utilizes a plant model to control the plant, defining the control set-points, by predicting the plant output at future time instants over a specific time horizon. This method uses as input data to the plant model the latest measurements of the plant as well as predicted and historical data. The plant operation is optimized through the solution of an optimization problem that minimizes an objective function subject to the plant model and other physical constraints as follows

$$\begin{aligned} \min \quad & \sum_{t=1}^{T} f_t(\mathbf{x}_t) && (2.18) \\ \text{s.t.} \quad & g_{j,t}(\mathbf{x}_t) \leq 0, \quad j = 1, ..., J, t \in \mathcal{T} \\ & l_{i,t}(\mathbf{x}_t) = 0, \quad i = 1, ..., I, t \in \mathcal{T}, \end{aligned}$$

where $\mathcal{T} = \{1, ..., T\}$ denotes the considered time horizon and decision variables x_t, $t \in \mathcal{T}$, denote the control set-points for each time instant t.

MPC, also known as receding horizon control, solves repeatedly the optimization problem of the plant model, using updated input data, and sends control set-points to the plant. Specifically, the following steps are applied in every ΔT (time-slot length) hours [24]:

1. The optimization problem (2.18) of the plant model is solved to define the control set-points x_t, $\forall t \in T$, by optimizing the plant operation over a moving time horizon.

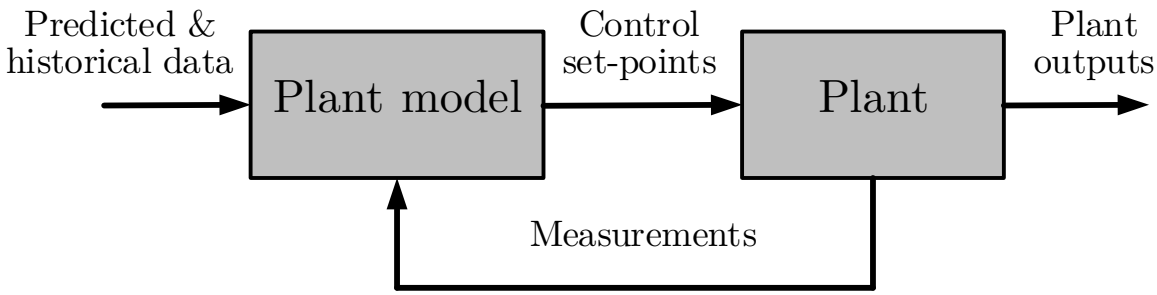

Figure 2.5: Model predictive control framework.

2. The first control set-point $x_{t=1}$ is sent to the plant, while the next control set-points are neglected, $x_t, \forall t = \{2, 3, ..., T\}$. This is because in every iteration of the MPC method new information is available, e.g., predicted data and real-time measurements, thus the horizon is shifted towards the future and step 1 is repeated using the updated input data.

The MPC method is widely used for industrial applications because it addresses well prediction uncertainty and modelling inaccuracies through the use of the receding horizon concept [23, 24].

2.4 Scenario-based stochastic optimization

Decision-making problems in the real world, e.g., in fields such as engineering, economics, and finance, frequently involve uncertainty. However, decisions must be made even with lack of perfect information. One way to address this issue is with the use of scenario-based stochastic programming.

Scenario-based stochastic optimization is widely used in power systems to solve optimization problems under different uncertainty sources, e.g., RES power generation. This approach uses representative scenarios to capture a wide range of possible realizations of the underlying stochastic processes (e.g., day-ahead RES generation) [25]. Let $\mathcal{S} = \{1, ..., S\}$ denotes the scenario set, $\mathbf{u}_s$ the vector of values associated with scenario curve $s \in \mathcal{S}$, and ϕ_s the associated weight of scenario curve s, such that $\sum_{s \in \mathcal{S}} \phi_s = 1$. The goal of scenario-based stochastic formulations is to optimize the expected value of the objective function. This value is computed as a

weighted average across all scenarios [26], yielding the optimization formulation

$$\begin{aligned} \text{minimize} \quad & \sum_{s\in\mathcal{S}} \phi_s f(\mathbf{x}, \mathbf{u}_s, \mathbf{y}_s) \\ \text{subject to} \quad & g_j(\mathbf{x}, \mathbf{u}_s, \mathbf{y}_s) \leq 0, \quad j = 1, ..., J, \quad s = 1, ..., S, \\ & l_i(\mathbf{x}, \mathbf{u}_s, \mathbf{y}_s) = 0, \quad i = 1, ..., I, \quad s = 1, ..., S, \end{aligned} \tag{2.19}$$

where vectors $\mathbf{x}$ and $\mathbf{y}_s$, $s = 1, ..., S$, denote the scenario-independent and scenario-dependent variables, respectively.

The effectiveness of the scenario-based stochastic optimization problem (2.19) depends on the representative scenarios that characterize the stochastic processes. To improve the accuracy of the optimization results, the scenarios should be diverse enough to cover the range of all possible outcomes. However, selecting a large number of scenarios increases the computational complexity of the resulting problem. A problem can even become computationally intractable when the considered problem is non-convex. Therefore, a main challenge in scenario-based stochastic optimization is to find a good trade-off between computational efficiency and solution quality by appropriately selecting representative scenarios [25, 26].

Chapter 3

Optimization of general energy management problems in power systems involving non-convex ESS models

Energy storage systems (ESSs) are increasingly used in power system optimization. Different ESS mathematical models are developed that consider nonlinear functions for power losses. However, these models require non-convex constraints to represent the ESS losses, resulting in challenging optimization problems. To reduce the complexity, convex relaxation models are often derived but generate infeasible solutions when the relaxation exactness is violated. To deal with this issue, this work develops two successive convexification algorithms that generate fast and high-quality feasible solutions when the derived solution is not exact. The first algorithm handles general loss functions, while the second algorithm enhances performance when piecewise-linear loss functions are used. Specifically, the algorithms reduce the feasible region of the relaxed ESS models using a tightening box trust region around the current solution in successive iterations. The proposed algorithms are applied to the Unit Commitment and Peak Shaving and Energy Arbitrage problems to investigate their performance considering piecewise-linear and quadratic ESS loss functions. Simulation results demonstrate the impact of the ESSs relaxation violation on the actual system operation and validate the algorithms efficacy to generate high-quality feasible and even optimal solutions with significantly lower execution times compared to problems utilizing exact ESS models.

3.1 Introduction

The increasing utilization of ESSs in power system applications necessitates the use of mathematical models for their representation in power system optimization problems. Different ESS models have been proposed that utilize non-convex constraints to represent the ESS power losses, e.g., using piecewise linear and quadratic loss functions [27], resulting in non-convex optimization problems. To solve these challenging problems, relaxed ESS models are often derived by relaxing the non-convex constraints. The relaxed ESS models reduce the problem complexity because they are convex, making them suitable for real-time online energy management, e.g, using model predictive control. However, the relaxed models yield infeasible solutions when the derived solutions are not exact.

The relaxed ESS models have been used in [28–33] to formulate convex optimization problems, which can be fast and reliably solved. These optimization problems manage the ESSs operation in active distribution grids [28–30], transmission networks [31] and microgrids [32]. Although the exactness of relaxed ESS models is shown to hold in some optimization formulations [28,30,33], they can be non-exact in other formulations [31].

The relaxed ESS models are also used in non-convex mixed-integer optimization problems, which are hard to solve, to reduce their computational complexity by decreasing the number of binary variables [34–38]. Specifically, the relaxed ESS models are utilized in various unit commitment problems that consider electric vehicles [34], stochasticity of RES [35], and contingencies [36], as well as in expansion planning (EP) problems [37,38]. Although the relaxation exactness is shown to hold under some conditions in [36] and [37], two examples where the relaxation exactness is violated in the UC and EP problems are presented in [39].

There are two approaches for dealing with potential violation of the exactness of the ESS relaxed constraints. The first approach is to prove their exactness under all or specific conditions to guarantee feasibility of the considered problems. The relaxation exactness is ensured for different formulations under some sufficient conditions [30,33,34,40], but these conditions limit the applicability of the relaxed ESS models. The second approach is to develop methodologies that find feasible solutions when the derived solutions result in non-exact ESS constraints. In [31], a penalty term is added in the optimization objective function to avoid simultaneous

charging and discharging, generating feasible solutions. However, this approach is applicable only to a specific piecewise-linear ESS model and requires a proper tuning of the penalty parameter because small values may yield infeasible solutions, while large values may lead to non-optimal solutions. In fact, tuning needs to be performed separately for each problem instance, limiting the applicability of this method.

This chapter develops two convexification algorithms that yield fast and high-quality feasible solutions when the derived solution using relaxed ESS models is not exact. The first algorithm considers various ESS models with different loss functions, while the second specialized algorithm enhances the algorithm performance when piecewise-linear ESS models are used. Specifically, both algorithms reduce the feasible region of the relaxed ESS models in each iteration using a *trust region* around the obtained solution. The performance of the proposed algorithms is investigated by considering two optimization problems in power systems that incorporate ESSs: (a) the *Unit Commitment* and (b) the *Peak Shaving and Energy Arbitrage* (PSEA). These problems were appropriately selected to study the impact of the relaxation violation on the actual system operation, because they can generate non-exact solutions when the relaxed ESS models are used. Simulation results validate the effectiveness of the proposed algorithms to yield high-quality feasible and even optimal solutions with significantly lower execution times compared to problems utilizing exact ESS models. To the best of our knowledge, this is the first work that develops convexification algorithms that deal with potential violation of the exactness of the ESS relaxed constraints considering general power loss functions.

The rest of the chapter is organized as follows. Section 3.2 states the examined problem and Section 3.3 describes the considered ESSs models. The proposed algorithms are presented in Section 3.4 and the UC and PSEA problems are formulated in Section 3.5. Simulation results are shown in Section 3.6 and conclusions are given in Section 3.7.

3.2 Problem statement

3.2.1 Generic ESS model

The generic ESS model used in power system optimization problems is expressed in discrete time and describes the evolution of the ESS state-of-charge (SoC[1]) over time based on the charging/discharging power and power losses, given by

$$C_{t+1,k} = C_{t,k} + \Delta T(-P^S_{t,k} - P^L_{t,k}), \quad \forall t \in \mathcal{T}, k \in \mathcal{K}, \tag{3.1}$$

where $\mathcal{T} = \{1, ..., T\}$ denotes the considered time horizon and ΔT the time-slot length in hours; $\mathcal{K} = \{1, ..., K\}$ denotes the set of ESSs, and K the number of the considered ESSs. Variables $C_{t,k}$, $P^S_{t,k}$ and $P^L_{t,k}$ denote the ESS SoC, discharging ($P^S_{t,k} \geq 0$) or charging ($P^S_{t,k} < 0$) power, and power losses, respectively. The ESS energy and power limits are set as

$$C_{0,k} = I_k, \quad \underline{C}_k \leq C_{t,k} \leq \overline{C}_k, \quad \forall t \in \mathcal{T}, k \in \mathcal{K}, \tag{3.2a}$$

$$\underline{P}^S_{t,k} \leq P^S_{t,k} \leq \overline{P}^S_{t,k}, \quad \forall t \in \mathcal{T}, k \in \mathcal{K}, \tag{3.2b}$$

where constants $\underline{C}_k$ and $\overline{C}_k$ denote the minimum and maximum SoC limits, $\overline{P}^S_{t,k}$ and $\underline{P}^S_{t,k}$ the discharging and charging power limits, and I_k the initial SoC.

3.2.2 ESS power losses

Several ESS models have been proposed in the literature that consider different functions to represent the ESS power losses in (3.1), depending on the ESS technology.
Lossless ESS Model. This is the simplest but most unrealistic model given by

$$P^L_{t,k} = 0, \quad \forall t \in \mathcal{T}, k \in \mathcal{K}. \tag{3.3}$$

Piecewise-linear ESS Model. This is the most widely used model that represents electrochemical storage technologies [27]. It is defined as

$$P^L_{t,k} = e_k |P^S_{t,k}|, \quad \forall t \in \mathcal{T}, k \in \mathcal{K}, \tag{3.4}$$

where e_k is a positive power loss coefficient. The absolute value in (3.4) is used to avoid negative losses when $P^S_{t,k} < 0$; thus, the power losses are represented by two

[1]SoC refers to the ratio between the energy stored in an ESS and the ESS capacity given in %. This work refers to the SoC as the energy stored in an ESS in Wh.

piecewise-linear segments. Note that the model in (3.4) can be reformulated using a constant charging/discharging efficiency and two separate variables for charging and discharging [29,30,33]. A variation of the piecewise-linear model in (3.4), where the power losses are proportional to $|P^S_{t,k}|$ and $C_{t,k}$ [27], is defined as

$$P^L_{t,k} = e_k|P^S_{t,k}| + e^c_k C_{t,k}, \quad \forall t \in \mathcal{T}, k \in \mathcal{K}, \tag{3.5}$$

where e^c_k is the losses coefficient associated with the SoC.

Quadratic ESS Model. The quadratic model is also used for electrochemical storage [27], given by

$$P^L_{t,k} = e^q_k(P^S_{t,k})^2, \quad \forall t \in \mathcal{T}, k \in \mathcal{K}, \tag{3.6}$$

where e^q_k is a positive losses coefficient. Using (3.6), high charging/discharging power rates are "penalized", because increased power losses are generated.

General ESS Model. To represent various power loss functions using one ESS model, we define the general model as

$$P^L_{t,k} = \hat{g}(P^S_{t,k}, C_{t,k}), \quad \forall t \in \mathcal{T}, k \in \mathcal{K}, \tag{3.7}$$

where $\hat{g}(P^S_{t,k}, C_{t,k})$ denotes the power loss function. For example, $\hat{g}(P^S_{t,k}, C_{t,k}) = e_k|P^S_{t,k}|$ and $\hat{g}(P^S_{t,k}, C_{t,k}) = e^q_k(P^S_{t,k})^2$ when the ESS models in (3.4) and (3.6) are used, respectively.

3.2.3 Optimization formulation

The general ESS model (3.1)-(3.2b), (3.7) can be used in an optimization problem to allow the optimal energy scheduling of ESSs incorporated in a power system application. Let $\mathbf{P^S}$, $\mathbf{P^L}$, and $\mathbf{C}$ denote the vector forms of the variables $P^S_{t,k}$, $P^L_{t,k}$, and $C_{t,k}$, $\forall t \in \mathcal{T}, k \in \mathcal{K}$, respectively. Let also vector $\mathbf{y}$ denote all the ESS variables, $\mathbf{y} = \{\mathbf{P^S}, \mathbf{P^L}, \mathbf{C}\}$, and vector $\mathbf{x}$ denote the rest design variables of a problem under consideration. Such an optimization problem, can be stated as

$$\begin{aligned}
\text{minimize} \quad & f(\mathbf{x}, \mathbf{y}) && \text{(3.8a)}\\
\text{subject to} \quad & g_j(\mathbf{x}, \mathbf{y}) \leq 0, \quad j = 1, ..., J, && \text{(3.8b)}\\
& l_h(\mathbf{x}, \mathbf{y}) = 0, \quad h = 1, ..., H, && \text{(3.8c)}\\
& (3.1) - (3.2b), (3.7) && \text{(3.8d)}
\end{aligned}$$

where $f(\mathbf{x}, \mathbf{y})$ is the objective function and $g_j(\mathbf{x}, \mathbf{y})$ and $l_h(\mathbf{x}, \mathbf{y})$ are the inequality and equality constraints associated with the considered problem, respectively. Problem

(3.8) is convex, which can be fast and reliably solved, when (a) $f(\mathbf{x}, \mathbf{y})$ and $g_j(\mathbf{x}, \mathbf{y})$ are convex functions and (b) $l_h(\mathbf{x}, \mathbf{y})$ and $\hat{g}(P^S_{t,k}, C_{t,k})$ are affine functions [17]. However, constraint (3.7) is non-convex in the general case because function $\hat{g}(P^S_{t,k}, C_{t,k})$ is nonlinear; hence, Problem (3.8) is non-convex and hard to solve. To address this issue, (3.7) can be relaxed to an inequality constraint, yielding the relaxed problem

$$\text{minimize} \quad f(\mathbf{x}, \mathbf{y}) \tag{3.9a}$$

$$\text{subject to} \quad (3.1) - (3.2b), (3.8b) - (3.8c), \tag{3.9b}$$

$$P^L_{t,k} \geq \hat{g}(P^S_{t,k}, C_{t,k}), \quad \forall t \in \mathcal{T}, k \in \mathcal{K}. \tag{3.9c}$$

Constraint (3.9c) is convex when function $\hat{g}(P^S_{t,k}, C_{t,k})$ is convex, e.g., using the power loss functions of the piecewise linear and quadratic ESS models. Therefore, the relaxed problem deals with power losses using nonlinear convex constraints. The relaxed problem generates the optimal solution of the exact problem (3.8) when the relaxation exactness is satisfied, i.e., equality is attained in constraint (3.9c). Otherwise, the solution is infeasible because increased ESS power losses are generated, which means that more energy is wasted than prescribed by the power loss function. In addition to generating fast and reliable solutions when the relaxed problem is convex, a significant computational time reduction can also be achieved even when the formulated relaxed problem is a mixed-integer program, i.e. when $\mathbf{x}$ includes integer variables.

Obtaining equality in constraint (3.9c) when solving the relaxed problem (3.9) implies relaxation exactness and hence optimality for problem (3.8). Nonetheless, little attention has been given to cases where the relaxation is not exact. This work aims to develop solution methodologies that yield fast and high-quality solutions to (3.8) under different ESS models, even when the solution of (3.9) is infeasible for (3.8).

3.3 Energy storage models

This section formulates the exact and relaxed versions of the piecewise-linear and quadratic ESS models and presents the feasible region of their power losses.

3.3.1 Piecewise-linear ESS models

Exact Model E_L. The loss function in (3.4) is reformulated to define the discharging and charging power losses

$$P^{L,d}_{t,k} = e^d_k P^S_{t,k}, \quad P^{L,c}_{t,k} = (-e^c_k) P^S_{t,k}, \quad \forall t \in \mathcal{T}, k \in \mathcal{K}, \tag{3.10}$$

where e^d_k and e^c_k denote the positive discharging and charging losses coefficients. Note that $P^{L,d}_{t,k} \geq 0$ and $P^{L,c}_{t,k} \leq 0$ when $P^S_{t,k} \geq 0$ (discharging), while $P^{L,d}_{t,k} < 0$ and $P^{L,c}_{t,k} \geq 0$ when $P^S_{t,k} \leq 0$ (charging). Therefore, the power losses are defined as the maximum between $P^{L,d}_{t,k}$ and $P^{L,c}_{t,k}$, given by

$$P^L_{t,k} = \max(P^{L,d}_{t,k}, P^{L,c}_{t,k}), \quad \forall t \in \mathcal{T}, k \in \mathcal{K}. \tag{3.11}$$

Constraint (3.11) is non-convex and logical constraints with binary variables are needed to represent it. An alternative way to handle constraint (3.11) is by replacing $P^S_{t,k}$ with separate variables for the charging and discharging power, $P^c_{t,k} \geq 0$ and $P^d_{t,k} \geq 0$, defined as

$$P^S_{t,k} = P^d_{t,k} - P^c_{t,k}, \quad \forall t \in \mathcal{T}, k \in \mathcal{K}. \tag{3.12}$$

Using (3.12), the power losses in (3.10)-(3.11) are reformulated as

$$P^L_{t,k} = e^d_k P^d_{t,k} + e^c_k P^c_{t,k}, \quad \forall t \in \mathcal{T}, k \in \mathcal{K}, \tag{3.13a}$$

$$P^d_{t,k} \perp P^c_{t,k}, \quad \forall t \in \mathcal{T}, k \in \mathcal{K}. \tag{3.13b}$$

The non-convex complementarity constraint (3.13b) ensures non-simultaneous charging and discharging, such that $P^L_{t,k} = e^d_k P^d_{t,k}$ and $P^L_{t,k} = e^c_k P^c_{t,k}$ when $P^S_{t,k} \geq 0$ and $P^S_{t,k} \leq 0$, respectively. Replacing (3.12)-(3.13a) in (3.1) yields the widely-used model formulation [29,30,33] given by

$$C_{t+1,k} = C_{t,k} + \Delta T(-P^d_{t,k}/\eta^d_k + \eta^c_k P^c_{t,k}), \quad \forall t \in \mathcal{T}, k \in \mathcal{K}, \tag{3.14a}$$

$$0 \leq P^d_{t,k} \leq \overline{P}^S_{t,k},\ 0 \leq P^c_{t,k} \leq |\underline{P}^S_{t,k}|, \quad \forall t \in \mathcal{T}, k \in \mathcal{K}, \tag{3.14b}$$

$$\text{Constraints (3.2a), (3.13b)}, \tag{3.14c}$$

where constants $\eta^d_k = 1/(1 + e^d_k)$ and $\eta^c_k = 1 - e^c_k$ denote the discharging and charging efficiency coefficients. The complementarity constraints (3.13b) can be modelled using type 1 special ordered set (SOS-1) constraints, as SOS-1($P^d_{t,k}, P^c_{t,k}$).

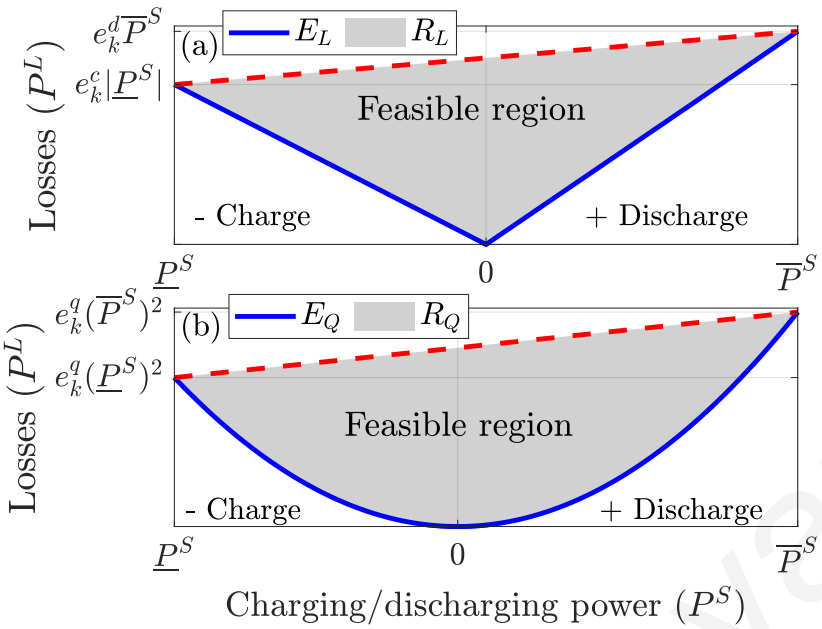

Figure 3.1: Power losses of the exact and relaxed versions of the (a) piecewise linear and (b) quadratic ESS models as a function of the charging/discharging power. The blue solid lines have the dual role of (a) presenting the feasible region of the exact models, indicating the actual losses, and (b) providing lower bounds on the power losses with respect to the relaxed models. Similarly, the red dashed lines provide upper bounds on the power losses, such that the shaded areas are the feasible regions of the relaxed models. For ease of representation we omit indices t, k from the variables in the figure.

Relaxed Model R_L. Deriving the convex hull of constraint (3.11) yields the relaxed model as

$$\text{Constraints (3.1)} - \text{(3.2b)} \tag{3.15a}$$

$$P^L_{t,k} \geq e^d_k P^S_{t,k}, \quad P^L_{t,k} \geq (-e^c_k) P^S_{t,k}, \quad \forall t \in \mathcal{T}, k \in \mathcal{K}, \tag{3.15b}$$

$$P^L_{t,k} \leq e^c_k |\underline{P}^S_{t,k}| + \alpha_{t,k}(P^S_{t,k} + |\underline{P}^S_{t,k}|), \quad \forall t \in \mathcal{T}, k \in \mathcal{K}, \tag{3.15c}$$

where constant $\alpha_{t,k} = (e^d_k \overline{P}^S_{t,k} - e^c_k |\underline{P}^S_{t,k}|)/(\overline{P}^S_{t,k} + |\underline{P}^S_{t,k}|)$. Affine constraints (3.15b) and (3.15c) provide lower and upper bounds on the power losses according to (3.11), creating the feasible region shown in Figure 3.1(a).

3.3.2 Quadratic ESS models

Exact Model E_Q. The exact quadratic ESS model is set as

$$\text{Constraints (3.1)} - \text{(3.2b)}, \text{(3.6)}. \tag{3.16a}$$

The non-convex quadratic constraint (3.6) can be modeled using bilinear constraints, but solving problems with bilinear constraints optimally is computationally expensive [41].

Approximate Model E_X. To reduce the computational complexity of Model E_Q, the non-convex quadratic constraint (3.6) is approximated using a piecewise-linear function with N linear segments. Specifically, $N+1$ points, $\mathcal{N} = \{1, ..., N+1\}$, on the Cartesian plane with coordinates $(\hat{x}_n, \hat{y}_n)$, $n \in \mathcal{N}$ are selected, where $\hat{x}_n$ and $\hat{y}_n$ correspond to the values of $P^S_{t,k}$ and $P^L_{t,k}$, respectively. Since two adjacent points can be used as the endpoints that represent a linear segment, the approximate model is given by

$$\text{Constraints (3.1)} - \text{(3.2b)} \tag{3.17a}$$

$$P^S_{t,k} = \sum_{n \in \mathcal{N}} \hat{x}_n \lambda_{t,k,n}, \qquad \forall t \in \mathcal{T}, k \in \mathcal{K}, \tag{3.17b}$$

$$P^L_{t,k} = \sum_{n \in \mathcal{N}} \hat{y}_n \lambda_{t,k,n}, \qquad \forall t \in \mathcal{T}, k \in \mathcal{K}, \tag{3.17c}$$

$$\sum_{n \in \mathcal{N}} \lambda_{t,k,n} = 1, \qquad \forall t \in \mathcal{T}, k \in \mathcal{K}, \tag{3.17d}$$

$$\text{SOS-2: } \{\lambda_{t,k,1}, \lambda_{t,k,2}, ..., \lambda_{t,k,N+1}\}, \quad \forall t \in \mathcal{T}, k \in \mathcal{K}, \tag{3.17e}$$

where $\lambda_{t,k,n}$ are positive continuous variables which correspond to one specific point. The type 2 special ordered set (SOS-2[2]) constraints (3.17e) ensure that the points lie on the piecewise linear curve [20]. Although approximating the quadratic loss function selecting a large number of linear segments reduces the approximation error, the computational complexity increases. Figure 3.2 shows an example of the piecewise-linear approximation with $N = 4$ and $N = 20$.

Relaxed Model R_Q. Deriving the convex hull of the feasible set of constraint (3.6) yields the following relaxed model

$$\text{Constraints (3.1)} - \text{(3.2b)} \tag{3.18a}$$

$$P^L_{t,k} \geq e^q_k (P^S_{t,k})^2, \qquad \forall t \in \mathcal{T}, k \in \mathcal{K}, \tag{3.18b}$$

$$P^L_{t,k} \leq e^q_k (\underline{P}^S_{t,k})^2 + \hat{\alpha}_{t,k} (P^S_{t,k} + |\underline{P}^S_{t,k}|), \quad \forall t \in \mathcal{T}, k \in \mathcal{K}, \tag{3.18c}$$

where constant $\hat{\alpha}_{t,k} = (e^q_k (\overline{P}^S_{t,k})^2 - e^q_k (\underline{P}^S_{t,k})^2) / (\overline{P}^S_{t,k} + |\underline{P}^S_{t,k}|)$. The convex quadratic and affine constraints (3.18b) and (3.18c) provide lower and upper bounds on the power losses according to (3.6), creating the feasible region of Figure 3.1(b).

[2]The SOS-2 constraint involves an ordered set of variables where at most two adjacent variables in the set can take non-zero values (see [20], Section 9.3).

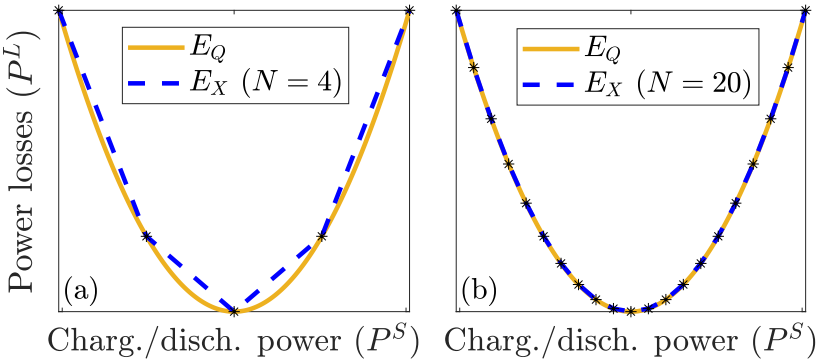

Figure 3.2: ESSs power losses as a function of the charging/discharging power for Models E_Q and E_X: (a) $N = 4$ and (b) $N = 20$ linear segments are considered for the piecewise linear approximation in Model E_X.

3.3.3 Relaxation exactness and tightness

The Relaxed Model R_L provides the same solution with the Exact Model E_L when equality is attained in one of the two constraints in (3.15b), otherwise increased power losses occur. Similarly, the Relaxed Model R_Q is exact when the equality is attained in (3.18b). Figure 3.1 depicts the feasible region of the power losses for both the exact and relaxed versions of the piecewise linear and quadratic ESS models. As can be observed, Models R_L and R_Q are tight because the feasible region of these models is the convex hull of the feasible region of the corresponding Exact Models E_L and E_Q.

3.4 Solution methodology

This section proposes a methodology to generate fast and high-quality feasible solutions, using the relaxed problem (3.9), when the relaxed ESS constraint (3.9c) is not exact. Specifically, two successive convexification algorithms for (a) general ESS models (SCA-GN) and (b) piecewise-linear ESS models (SCA-PL) are developed. Algorithm SCA-PL is a specialized version of SCA-GN to enhance the algorithm performance when piecewise-linear loss functions are used. Thus, only Model R_L and both Models R_L and R_Q can be used in Algorithms SCA-PL and SCA-GN, respectively. Towards this direction, we define the optimization formulations $\mathbb{P}_L^R$ and $\mathbb{P}_Q^R$ that integrate Models R_L and R_Q, respectively, and are utilized by the proposed

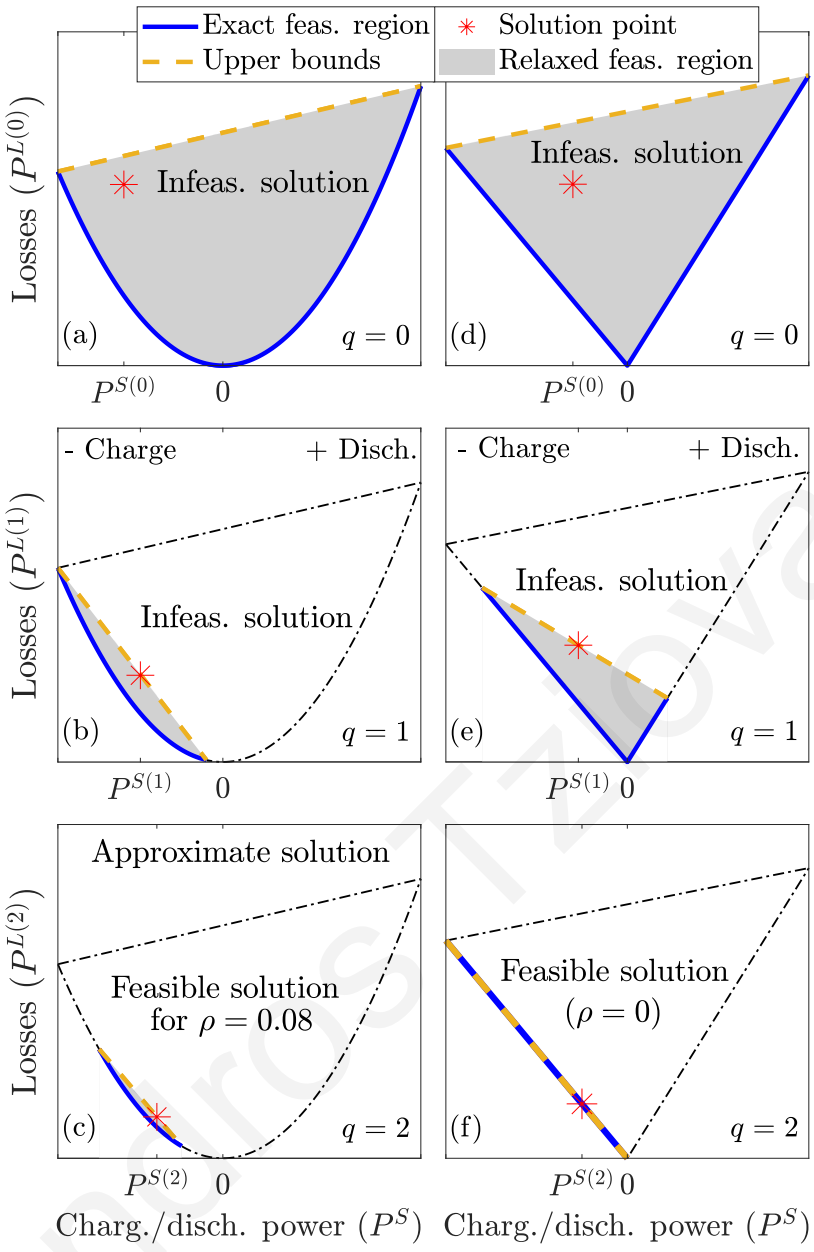

Figure 3.3: Examples of Algorithm SCA-GN using Model R_Q (a)-(c) and Algorithm SCA-PL using Model R_L (d)-(f) over iterations $q = \{0, 1, 2\}$.

algorithms as

$$\mathbb{P}_L^R : \begin{cases} \text{minimize} & \text{(3.8a)} \\ \text{subject to} & \text{(3.8b), (3.8c), (3.15a) – (3.15c).} \end{cases}$$

$$\mathbb{P}_Q^R : \begin{cases} \text{minimize} & \text{(3.8a)} \\ \text{subject to} & \text{(3.8b), (3.8c), (3.18a) – (3.18c).} \end{cases}$$

3.4.1 Algorithm SCA-GN

The main idea of Algorithm SCA-GN is to reduce the relaxed feasible region of the ESS power losses, depicted in Figures 3.1(a) and (b), in successive iterations using a tightening box *trust region* around the current solution. Specifically, as shown in Figures 3.3(a)-(c), the relaxed feasible region is reduced by adjusting the maximum discharging and charging power limits in iteration q, $\overline{P}_{t,k}^{S(q)}$ and $\underline{P}_{t,k}^{S(q)}$, based on a *trust region* around the ESS power set-points, $P_{t,k}^{S(q-1)}$, obtained in the previous iteration $q-1$. Feasible solutions are obtained for Algorithm SCA-GN when the relaxation exactness condition is satisfied $\forall t \in \mathcal{T}$, $k \in \mathcal{K}$, defined as

$$\hat{g}(P_{t,k}^{S(q)}, C_{t,k}^{(q)}) \leq P_{t,k}^{L(q)} \leq \hat{g}(P_{t,k}^{S(q)}, C_{t,k}^{(q)}) + \rho, \tag{3.19}$$

where parameter $\rho \geq 0$ denotes the maximum approximation error. Note that feasible solutions are generated according to (3.7) when $\rho = 0$. However, similarly with the Approximate Model E_X, an approximate solution can also be obtained when $\rho > 0$. For example, an approximate solution for Algorithm SCA-GN is presented in Figure 3.3(c) when $\rho = 0.08$.

Algorithm 1 summarizes the proposed procedure utilizing Problem $\mathbb{P}_i^R$, $i = \{L, Q\}$. Initially, Problem $\mathbb{P}_i^R$ is solved (Line 3) such that the obtained solution is feasible when condition (3.19) is satisfied; otherwise, the iterative procedure is executed (Lines 7-16). Algorithm SCA-GN considers a "trust region" length $L_{t,k}^{(q)}$ that defines the relative distance between the maximum charging and discharging bounds in iteration q, $\underline{P}_{t,k}^{S(q)}$ and $\overline{P}_{t,k}^{S(q)}$, initialized as $L_{t,k}^{(0)} = |\underline{P}_{t,k}^{S}| + \overline{P}_{t,k}^{S}$ (Line 7). The region length $L_{t,k}^{(q)}$ is reduced in each iteration q according to Line 10 of Algorithm 1, where the coefficient $0 < \sigma \leq 1$ controls the "trust region" length. Next, the new bounds $\overline{P}_{t,k}^{S(q)}$ and $\underline{P}_{t,k}^{S(q)}$ are calculated according to Lines 11-12 based on the $L_{t,k}^{(q)}$ and the ESS power set-points, $P_{t,k}^{S(q-1)}$, obtained in the previous iteration $q-1$. Lines 13-14 ensure that $\overline{P}_{t,k}^{S(q)}$ and $\underline{P}_{t,k}^{S(q)}$ are within the ESS power limits $\overline{P}_{t,k}^{S}$ and $\underline{P}_{t,k}^{S}$. Finally, Problem $\mathbb{P}_i^R$ is solved using the new bounds $\overline{P}_{t,k}^{S(q)}$ and $\underline{P}_{t,k}^{S(q)}$ (Line 15). Algorithm 1 converges when condition (3.19) is satisfied or when all $L_{t,k}^{(q)}$, $\forall t \in \mathcal{T}$, $\forall k \in \mathcal{K}$, become smaller than the algorithm tolerance ϵ (Line 8).

The solution quality and execution speed of Algorithm SCA-GN is dependent on the coefficients ρ, ϵ and σ. Small values of ρ are desirable because they reduce the approximation error, but increase the number of iterations and hence the execution time of Algorithm SCA-GN. Note that the tolerance ϵ is only used to ensure

Algorithm 1 : SCA-GN

1: **Input:** ρ, σ, ϵ, i.
2: **Init.** $q = 0$.
3: Solve $\mathbb{P}_i^R$ to obtain $\mathbf{x}^{(q)}$ and $\mathbf{y}^{(q)}$ ($P_{t,k}^{S(q)}$, $C_{t,k}^{(q)}$, $P_{t,k}^{L(q)}$).
4: **if** condition (3.19) is satisfied **then**
5: Return $\hat{\mathbf{x}} = \mathbf{x}^{(q)}$, $\hat{\mathbf{y}} = \mathbf{y}^{(q)}$.
6: **else**
7: Set $L_{t,k}^{(q)} = |\underline{P}_{t,k}^{S}| + \overline{P}_{t,k}^{S} \;\; \forall t \in \mathcal{T}, k \in \mathcal{K}$.
8: **while** $(\max_{t\in\mathcal{T},k\in\mathcal{K}} (L_{t,k}^{(q)}) \geq \epsilon)$ and ((3.19) is violated) **do**
9: Set $q = q + 1$.
10: Set $L_{t,k}^{(q)} = L_{t,k}^{(q-1)}(1-\sigma), \;\; \forall t \in \mathcal{T}, k \in \mathcal{K}$.
11: Set $\overline{P}_{t,k}^{S(q)} = P_{t,k}^{S(q-1)} + 0.5L_{t,k}^{(q)}, \;\; \forall t \in \mathcal{T}, k \in \mathcal{K}$.
12: Set $\underline{P}_{t,k}^{S(q)} = P_{t,k}^{S(q-1)} - 0.5L_{t,k}^{(q)}, \;\; \forall t \in \mathcal{T}, k \in \mathcal{K}$.
13: Set $\overline{P}_{t,k}^{S(q)} = \min(\overline{P}_{t,k}^{S}, \overline{P}_{t,k}^{S(q)}), \;\; \forall t \in \mathcal{T}, k \in \mathcal{K}$.
14: Set $\underline{P}_{t,k}^{S(q)} = \max(\underline{P}_{t,k}^{S}, \underline{P}_{t,k}^{S(q)}), \;\; \forall t \in \mathcal{T}, k \in \mathcal{K}$.
15: Solve $\mathbb{P}_i^R$ to obtain $\mathbf{x}^{(q)}$ and $\mathbf{y}^{(q)}$.
16: Return $\hat{\mathbf{x}} = \mathbf{x}^{(q)}$, $\hat{\mathbf{y}} = \mathbf{y}^{(q)}$.

convergence of Algorithm 1 when condition (3.19) cannot be satisfied, yielding approximate solutions; thus, ϵ should be selected sufficiently small. Moreover, large values of σ reduce the number of iterations but may generate sub-optimal or infeasible solutions for Problem $\mathbb{P}_i^R$. In contrast, small values increase the number of iterations but improve the solution quality.

3.4.2 Algorithm SCA-PL

Algorithm 2, which is an extension of Algorithm 1, utilizes only Problem $\mathbb{P}_L^R$ and varies the bounds $\overline{P}_{t,k}^{S(q)}$ and $\underline{P}_{t,k}^{S(q)}$ until one of the two parameters become negative or positive, respectively. Then, the corresponding parameter is set equal to zero and the other parameter is set equal to its initial value (Lines 2-5) to consider the whole charging or discharging segment, improving the algorithm performance in terms of solution quality and execution speed. An example of Algorithm SCA-PL using the Model R_L is shown in Figures 3.3(d)-(f).

Algorithm 2 : SCA-PL

1: Lines 1-14 of Algorithm 1.
2: **if** $\overline{P}_{t,k}^{S(q)} < 0, \ \forall t \in \mathcal{T}, k \in \mathcal{K}$ **then**
3: Set $\overline{P}_{t,k}^{S(q)} = 0, \ \underline{P}_{t,k}^{S(q)} = \underline{P}_{t,k}^{S}$.
4: **if** $\underline{P}_{t,k}^{S(q)} > 0, \ \forall t \in \mathcal{T}, k \in \mathcal{K}$ **then**
5: Set $\underline{P}_{t,k}^{S(q)} = 0, \ \overline{P}_{t,k}^{S(q)} = \overline{P}_{t,k}^{S}$.
6: Lines 15-16 of Algorithm 1.

Remark

Algorithm SCA-GN can be used for any convex power loss function, $\hat{g}(P_{t,k}^{S}, C_{t,k})$, and Algorithm SCA-PL for any piecewise-linear loss function, e.g., see (3.5). This can be achieved by (a) relaxing the non-convex ESS power losses constraint (3.7) to the convex constraint (3.9c), and (b) introducing upper bounds on the power losses in the formulation of the relaxed problem such that

$$P_{t,k}^{L} \leq \widetilde{g}(P_{t,k}^{S}, C_{t,k}), \quad \forall t \in \mathcal{T}, k \in \mathcal{K}. \tag{3.20}$$

Function $\widetilde{g}(P_{t,k}^{S}, C_{t,k})$ must be constructed in a way such that constraints (3.9c) and (3.20) define the convex hull of the exact feasible region, defined by (3.7).

3.5 Power system optimization problems

The performance of the presented ESS models and the proposed algorithms is investigated by considering two different optimization problems in power systems, the UC and PSEA.

3.5.1 Unit commitment

The UC problem schedules the generating resources to satisfy the load demand over a time horizon by minimizing the total cost of operation. Based on the simplified UC problem in [39], this problem schedules the conventional generating units and ESSs to ensure the power balance between generation and demand, including ramping constraints of the units. Let $\mathcal{G} = \{1, ..., G\}$ denotes the set with the generating units and variables $P_{t,g}^{G}$ and $z_{t,g} \in \{0, 1\}$ denote the generating power and *on/off* status of the unit $g \in \mathcal{G}$ at time $t \in \mathcal{T}$, respectively. The objective is to minimize the quadratic

cost functions of units. The considered problem, denoted by **U** is given by

$$\text{minimize} \;\; \Delta T \sum_{t\in\mathcal{T}} \sum_{g\in\mathcal{G}} (\hat{\alpha}_g z_{t,g} + \hat{\beta}_g P^G_{t,g} + \hat{\gamma}_g (P^G_{t,g})^2) \tag{3.21a}$$

subject to:

$$z_{t,g}\underline{P}^G_g \le P^G_{t,g} \le z_{t,g}\overline{P}^G_g, \quad \forall t \in \mathcal{T}, \forall g \in \mathcal{G}, \tag{3.21b}$$

$$P^G_{t,g} - P^G_{t-1,g} \le \Delta T(R^U_g z_{t-1,g} + R^{SU}_g (z_{t,g} - z_{t-1,g})) + \overline{P}^G_g (1 - z_{t,g}), \quad t \in \{2, ..., T\}, \;\; \forall g \in \mathcal{G}, \tag{3.21c}$$

$$P^G_{t-1,g} - P^G_{t,g} \le \Delta T(R^D_g z_{t,g} + R^{SD}_g (z_{t-1,g} - z_{t,g})) + \overline{P}^G_g (1 - z_{t-1,g}), \quad t \in \{2, ..., T\}, \forall g \in \mathcal{G}, \tag{3.21d}$$

$$\sum_{g\in\mathcal{G}} P^G_{t,g} + \sum_{k\in\mathcal{K}} P^S_{t,k} = \hat{D}_t, \quad \forall t \in \mathcal{T}, \tag{3.21e}$$

ESS Model, (3.21f)

where constants $\hat{\alpha}_g$, $\hat{\beta}_g$, and $\hat{\gamma}_g$ denote the coefficients of the quadratic cost function of unit $g \in \mathcal{G}$. In objective (3.21a), the fixed cost $\hat{\alpha}_g$ is included in the objective only when the unit is *on*, i.e., $z_{t,g} = 1$. Constraint (3.21b) ensures that the power generation of unit $g \in \mathcal{G}$ at time $t \in \mathcal{T}$ is between its minimum and maximum limits $(\underline{P}^G_g, \overline{P}^G_g)$ when $z_{t,g} = 1$; otherwise, $P^G_{t,g} = 0$ implying that the unit is *off*. Ramp-up constraints in (3.21c) limit the power increment of unit $g \in \mathcal{G}$ between two consecutive time intervals, where constants R^U_g and R^{SU}_g denote the generation upward and start-up ramp rates. Similarly, ramp-down constraints are set in (3.21d), where constants R^D_g and R^{SD}_g denote the generation downward and shutdown ramp rates. Constraint (3.21e) ensures the power balance between produced power from the units, ESSs discharging/charging power, and load demand $\hat{D}_t$. Similar to [39], start-up and shutdown costs, minimum up and down times, and reserves are neglected. The following five optimization problems are derived by integrating the ESS models in Problem **U**:

- $\mathbf{U}^E_L$ and $\mathbf{U}^E_Q$: Use the Exact Models E_L and E_Q.
- $\mathbf{U}^X$: Uses the Approximate Model E_X.
- $\mathbf{U}^R_L$ and $\mathbf{U}^R_Q$: Use the Relaxed Models R_L and R_Q.

When Model E_L is used, $P^S_{t,k}$ is replaced by $P^d_{t,k} - P^c_{t,k}$ in (3.21e). Utilizing the Relaxed Problems $\mathbf{U}^R_L$ and $\mathbf{U}^R_Q$ in Algorithms SCA-GN and SCA-PL yield three additional problems:

- $\mathbf{U}_L^{A1}$ and $\mathbf{U}_Q^{A1}$: Use $\mathbf{U}_L^R$ and $\mathbf{U}_Q^R$ in Algorithm SCA-GN.
- $\mathbf{U}_L^{A2}$: Uses $\mathbf{U}_L^R$ in Algorithm SCA-PL.

Problems $\mathbf{U}_L^E$, $\mathbf{U}_Q^E$, and $\mathbf{U}^X$ are MIQPs with SOS-1, bilinear, and SOS-2 constraints, respectively. Problems $\mathbf{U}_L^R$, $\mathbf{U}_L^{A1}$, and $\mathbf{U}_L^{A2}$ with the relaxed ESS models are MIQPs, while $\mathbf{U}_Q^R$ and $\mathbf{U}_Q^{A1}$ are mixed-integer quadratically constrained quadratic programs (MIQCQPs).

3.5.2 Peak shaving and energy arbitrage

This problem considers the integration of a single ESS, $\mathcal{K} = \{1\}$, in a high to medium voltage (HV/MV) distribution substation for peak shaving and energy arbitrage purposes. As shown in Figure 3.4, an ESS is utilized to absorb [provide] power from the distribution grid to eliminate the reverse [direct] power limit violations of the substation transformer, enabling an increased RES penetration and load demand growth. Moreover, the ESS is used to maximize profits through energy arbitrage in electricity markets by buying and storing energy when prices are low and selling when prices are high [42]. Towards this direction, an optimization problem is formulated to maximize the arbitrage profit and minimize the square of the violated power, x_t, $\forall t \in \mathcal{T}$. The considered problem, denoted by **S** is given by

$$\text{minimize} \quad \Delta T \sum_{t\in\mathcal{T}} (-\hat{c}_t P_t^S + W x_t^2) \tag{3.22a}$$

$$\text{subject to:} \quad \underline{P}^F - x_t \leq P_t^F \leq \overline{P}^F + x_t, \quad \forall t \in \mathcal{T}, \tag{3.22b}$$

$$P_t^F + P_t^S = D_t^P, \quad \forall t \in \mathcal{T}, \tag{3.22c}$$

$$\textit{ESS Model}, \tag{3.22d}$$

where variables P_t^F denote the transformer power. Constants $\hat{c}_t$ denote the electricity price for buying and selling power at time t, $\underline{P}^F$, $\overline{P}^F$ the reverse and direct power limits of the transformer, and D_t^P the predicted net-load demand of the distribution grid. Soft constraints (3.22b) restrain the transformer power within its limits, because variables x_t are penalized in the objective (3.22a) with a penalty coefficient W. To protect the transformer, the value of W must be sufficiently large such that the arbitrage profit is maximized as far as it does not create power violations. Constraints (3.22c) ensure the power flow balance between the distribution substation, the ESS and the distribution grid. The following five optimization problems are derived by

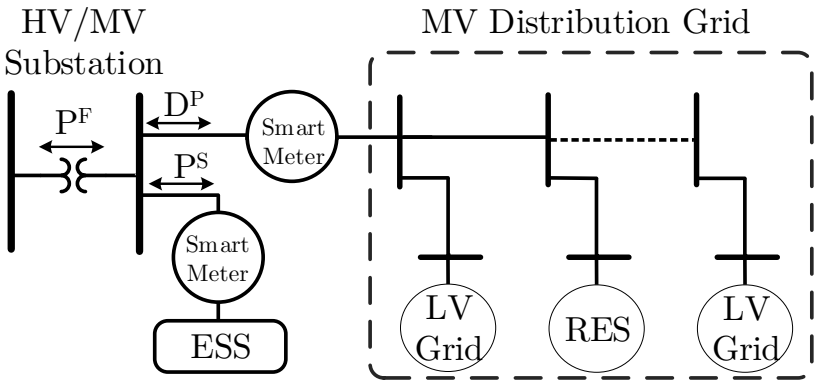

Figure 3.4: Peak shaving service to an HV/MV distribution substation.

incorporating the ESS models in Problem **S**:

- $\mathbf{S}_L^E$ and $\mathbf{S}_Q^E$: Use the Exact Models E_L and E_Q.
- $\mathbf{S}^X$: Uses the Approximate Model E_X.
- $\mathbf{S}_L^R$ and $\mathbf{S}_Q^R$: Use the Relaxed Models R_L and R_Q.

When *Model* E_L is used, P_t^S is replaced by $P_t^d - P_t^c$ in (3.22a) and (3.22c). Using the Relaxed Problems $\mathbf{S}_L^R$ and $\mathbf{S}_Q^R$ in Algorithms SCA-GN and SCA-PL yield problems:

- $\mathbf{S}_L^{A1}$ and $\mathbf{S}_Q^{A1}$: Use $\mathbf{S}_L^R$ and $\mathbf{S}_Q^R$ in Algorithm SCA-GN.
- $\mathbf{S}_L^{A2}$: Uses $\mathbf{S}_L^R$ in Algorithm SCA-PL.

Problems $\mathbf{S}_L^E$, $\mathbf{S}_Q^E$, and $\mathbf{S}^X$ are non-convex QPs with SOS-1, bilinear, and SOS-2 constraints, respectively. Problems $\mathbf{S}_L^R$, $\mathbf{S}_L^{A1}$, and $\mathbf{S}_L^{A2}$ are convex QPs, while $\mathbf{S}_Q^R$ and $\mathbf{S}_Q^{A1}$ are convex QCQPs.

3.6 Simulation results

This section evaluates the performance of the ESSs models and the proposed algorithms applied in the UC and PSEA problems. All problems in Section 3.5 are coded in Matlab and solved using optimization solver Gurobi [43] on a personal computer with 16 GB RAM and an Intel Core-i7 2.11 GHz processor. The algorithm parameters ρ and ϵ are set to 0.001 and 0.0001, respectively. To examine the solution quality of Problems $\mathbf{U}_i^R$, $\mathbf{U}_i^{A1}$, $\mathbf{U}_L^{A2}$, $\mathbf{S}_i^R$, $\mathbf{S}_i^{A1}$, and $\mathbf{S}_L^{A2}$, $i = \{L, Q\}$, the optimality gap metric is considered that defines the relative distance between their solution value and the

Table 3.1: Coefficients of generation units.

	$\underline{P}_g^G$	$\overline{P}_g^G$	$\hat{\alpha}_g$	$\hat{\beta}_g$	$\hat{\gamma}_g$	$R_g^U = R_g^D = R_g^{SU} = R_g^{SU}$
Unit 1:	2.4 MW	50 MW	0.5	3.0	0.02	15 MW
Unit 2:	2.4 MW	50 MW	5.0	19.9	0.04	15 MW

optimal solution

$$\text{Optim. Gap} = \frac{\text{Solut. Value} - \text{Optim. Value}}{\text{Optim. Value}} \times 100\%, \tag{3.23}$$

where the optimal value is obtained by solving the corresponding problems with the exact ESSs models. The following cases can be observed depending on the value of the optimality gap:

1. Optimality gap = 0: The optimal solution is generated if the ESSs relaxation is exact.

2. Optimality gap > 0: A feasible non-optimal solution is derived.

3. Optimality gap < 0: The ESSs relaxation is non-exact and hence an infeasible solution is generated.

3.6.1 Unit commitment

Setup. The simulation setup is composed of 2 conventional units and 6 ESSs presented in Tables 3.1 and 3.2 as well as the 24-hour load demand shown in Table 3.3, defined as Scenario S_1. Note that the ESSs efficiencies η_k^d and η_k^c and losses coefficients e_k^q, presented in Table 3.2, are used in the piecewise linear and quadratic ESS models, respectively. In Table 3.4 we consider Scenarios $S_1 - S_6$ with an increasing number of units and ESSs by (a) duplicating the units and ESSs of S_1 and (b) multiplying the load demand profile with the load magnitude of Table 3.4. The scenarios were selected in a way to yield non-exact solutions to Problems $\mathbf{U}_L^R$ and $\mathbf{U}_Q^R$.

ESSs relaxation violation. This case study examines the impact of the ESSs relaxation violation on the solution of the UC problem, considering only the piecewise-linear ESS model. Towards this direction, we consider Scenario S_1 but use the load demand given in Table 3.5 with a time horizon of 5 hours, instead of 24 hours, for better visualization of the results. The optimal results obtained from solving Problem

Table 3.2: ESSs Coefficients.

	$\underline{C}_k$	$\overline{C}_k$	I_k	$\overline{P}^S_{t,k} = \lvert\underline{P}^S_{t,k}\rvert$	$\eta^d_k = \eta^c_k$	e^q_k
ESS 1:	1.0 MWh	4.0 MWh	3.0 MWh	5.0 MW	0.89	0.030
ESS 2:	3.0 MWh	6.5 MWh	5.5 MWh	5.5 MW	0.91	0.020
ESS 3:	0.5 MWh	1.5 MWh	1.0 MWh	1.5 MW	0.88	0.025
ESS 4:	0.5 MWh	1.0 MWh	0.5 MWh	0.5 MW	0.92	0.018
ESS 5:	0.5 MWh	0.7 MWh	0.5 MWh	0.5 MW	0.89	0.040
ESS 6:	0.5 MWh	0.7 MWh	0.5 MWh	0.5 MW	0.91	0.019

Table 3.3: Load Demand I.

t (h)	1	2	3	4	5	6	7	8	9	10	11	12
$\hat{\mathbf{D}}_\mathbf{t}$ **(MW)**	10	36	28	38	14	46.1	39	34	38	43	36	28
t (h)	13	14	15	16	17	18	19	20	21	22	23	24
$\hat{\mathbf{D}}_\mathbf{t}$ **(MW)**	38	14	49	40	28	17	14	22	29	39	49	38

Table 3.4: Simulation Scenarios.

Scenarios	S_1	S_2	S_3	S_4	S_5	S_6
Total Units	2	12	18	24	30	36
Total ESSs	6	36	54	72	90	108
Load Magnitude	×1	×6	×9	×12	×15	×18

Table 3.5: Load Demand II.

t (h)	1	2	3	4	5
$\hat{\mathbf{D}}_\mathbf{t}$ **(MW)**	10	28	38	14	46.1

$\mathbf{U}^E_L$ are demonstrated in Figures 3.5(a)-3.5(d), while the results generated from solving Problem $\mathbf{U}^R_L$ are shown in Figures 3.5(e)-3.5(h). The generating power of the two units is illustrated in Figures 3.5(a) and 3.5(e), indicating that $\mathbf{U}^E_L$ commits both units at $4-5$ h while $\mathbf{U}^R_L$ commits only Unit 1. The total ESSs discharging/charging power is presented in Figures 3.5(b) and 3.5(f) and the total ESSs SoC is depicted in Figures 3.5(c) and 3.5(g). The total ESSs energy losses based on the discharging/charging power decisions are shown in Figures 3.5(d) and 3.5(h). The ESSs relaxation vio-

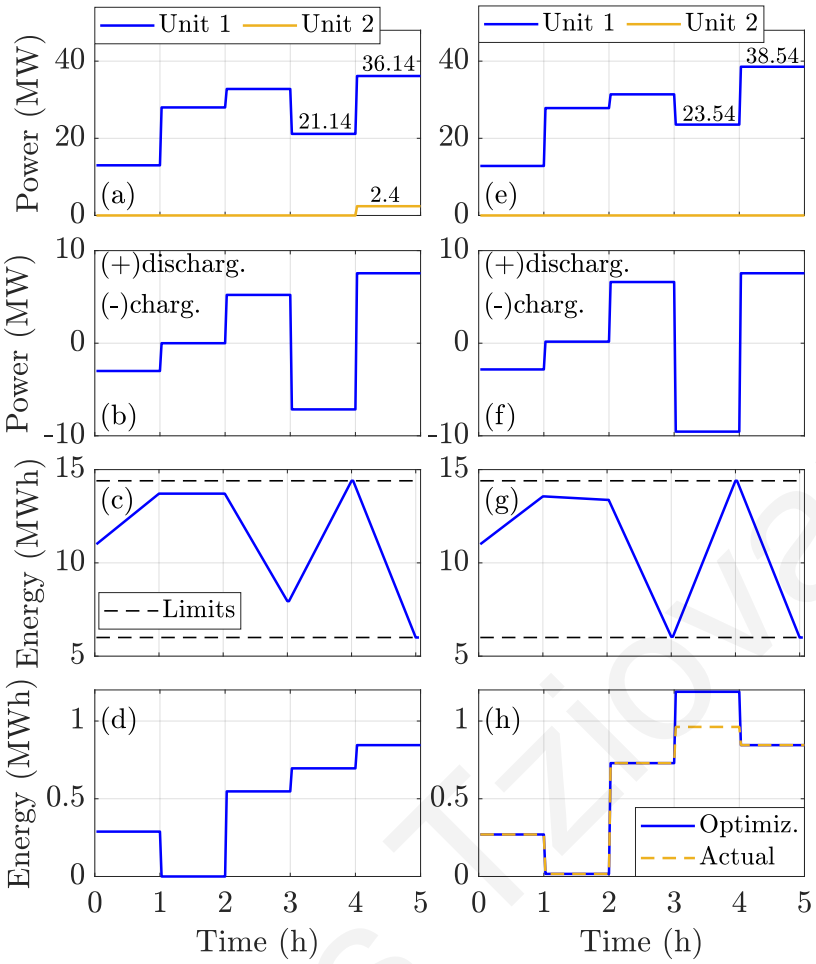

Figure 3.5: Optimization results obtained by solving Problems $\mathbf{U}_L^E$ (a)-(d) and $\mathbf{U}_L^R$ (e)-(h): (a) and (e) generating power of the conventional units, (b) and (f) total ESSs discharging/charging power, (c) and (g) total ESSs state-of-charge, and (d) and (h) total ESSs energy losses.

lation in $\mathbf{U}_L^R$ is indicated in Figure 3.5(h), for the interval $[3, 4]$ h, where the energy losses resulting from the optimization solution are higher than the actual losses[3]. As a result, the commitment of the "expensive" Unit 2 is avoided, yielding an operating cost of 484.26 € which is 7.65% (optimality gap = -7.65 %) lower than the optimal value of 524.36 €.

To study the impact of the relaxation violation on the real system operation, we calculate the actual ESSs power set-points[4] assuming that the charging/discharging decisions (see Figure 3.5(f)) are applied in actual ESSs with embedded primary controllers. Figure 3.6 shows a total power imbalance of -0.27 MW in the interval

[3]The actual losses are calculated by applying the discharging/charging power decisions of the optimization solution in the power loss function (3.7).

[4]The actual ESSs power set-points are calculated by assuming that the charging/discharging decisions of the optimization solution are applied in actual ESSs. Note that actual ESSs are embedded with primary controllers that ensure their power and energy limits.

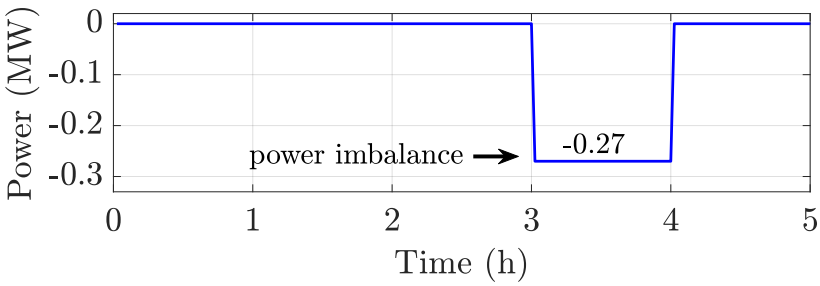

Figure 3.6: Total power imbalances occurring from the ESSs relaxation violation. The total power imbalances are defined as the scheduled ESSs discharging and charging power minus the actual ESSs power.

Table 3.6: Optimality gap (%) of Algorithms SCA-GN ($\mathbf{U}_L^{A1}$ and $\mathbf{U}_Q^{A1}$) and SCA-PL ($\mathbf{U}_L^{A2}$) for different values of σ.

σ	0.1	0.3	0.5	0.7	0.9	0.999
$\mathbf{U}_L^{A1}$	0	0	0.01	0.02	0.02	Infeasible
$\mathbf{U}_L^{A2}$	0	0	0	0	0	1.45
$\mathbf{U}_Q^{A1}$	0	0	0	0.02	Infeasible	Infeasible

[3, 4] h due to the relaxation violation, because the primary controllers reduce the ESSs charging power by 0.27 MW to ensure the SoC upper limits. The power imbalance leads to infeasibility because Unit 1 cannot reduce its generation under 23.54 MW and in the next interval to produce 38.54 MW due to its ramp-up limit of 15 MW/h. Power imbalances in real operation can be compensated by maintaining reserves, which is undesirable because it threatens the safe operation of the system.

Solution quality. This case study examines the efficacy of Algorithms SCA-GN and SCA-PL to generate high-quality feasible solutions when Problems $\mathbf{U}_L^R$ and $\mathbf{U}_Q^R$ yield infeasible solutions due to the ESSs relaxation violation. Towards this direction, Scenario S_1 is considered for 20 random load demand instances. Table 3.6 depicts the maximum optimality gap derived from solving Problems $\mathbf{U}_L^{A1}$, $\mathbf{U}_L^{A2}$ and $\mathbf{U}_Q^{A1}$ for the 20 new demand instances under different values of σ. Algorithm SCA-GN generates feasible solutions with less than 0.02% maximum optimality gap using the piecewise linear ESS model ($\mathbf{U}_L^{A1}$) when $\sigma \leq 0.9$; infeasible solutions are obtained for $\sigma = 0.999$. Algorithm SCA-PL ($\mathbf{U}_L^{A2}$) always generates feasible solutions and yields optimal solutions for $\sigma \leq 0.9$, indicating the superiority of Algorithm SCA-PL compared to SCA-GN when the piecewise-linear ESS model is used. When the quadratic ESS

Table 3.7: Maximum number of iterations (q) of Algorithms SCA-GN ($\mathbf{U}_L^{A1}$ and $\mathbf{U}_Q^{A1}$) and SCA-PL ($\mathbf{U}_L^{A2}$) for different values of σ.

σ	0.1	0.3	0.5	0.7	0.9	0.999
$\mathbf{U}_L^{A1}$	13	4	2	2	1	Infeasible
$\mathbf{U}_L^{A2}$	13	4	2	2	1	1
$\mathbf{U}_Q^{A1}$	32	10	5	3	Infeasible	Infeasible

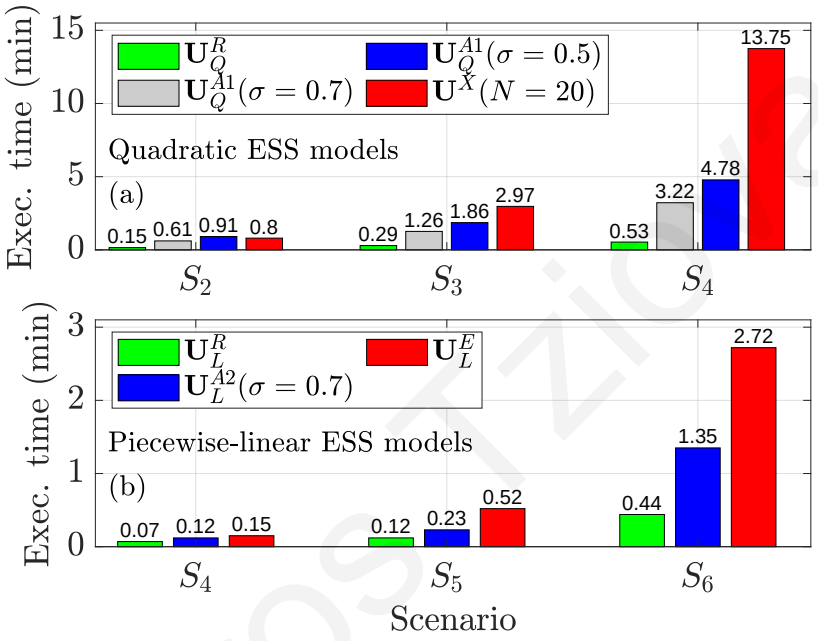

Figure 3.7: Average execution times of the problems with the relaxed and exact ESS models as well as the proposed algorithms when the (a) quadratic and (b) piecewise linear ESS models are considered.

model is utilized, Algorithm SCA-GN ($\mathbf{U}_Q^{A1}$) yields (a) feasible solutions for $\sigma \leq 0.7$ and (b) optimal solutions for $\sigma \leq 0.5$. Table 3.7 shows the decrement of the algorithms iterations q as the value of σ increases, indicating that optimal solutions with a small number of iterations ($q \leq 5$) are obtained for $0.5 \leq \sigma \leq 0.7$ (see Table 3.6).

Algorithms performance. The execution times and solution quality of the proposed algorithms are investigated for Scenarios $S_2 - S_6$, for five random demand instances. Considering the quadratic ESS models, Figure 3.7(a) depicts the low average execution times of Problem $\mathbf{U}_Q^R$ compared to the high execution times of $\mathbf{U}^X$ for $S_2 - S_4$; however, infeasible solutions are obtained by $\mathbf{U}_Q^R$ due to the relaxation violation. Note that Problem $\mathbf{U}^X$ is used instead of $\mathbf{U}_Q^E$, because the execution times of $\mathbf{U}_Q^E$ exceed the maximum time-limit set (60 minutes) for all scenarios. In Problem $\mathbf{U}^X$, we

Table 3.8: Average objective values of the problems that consider the quadratic ESS models.

Scenario	S_2	S_3	S_4
$\mathbf{U}_Q^R$	17300.598	25950.530	34600.632
$\mathbf{U}^X(N = 20)$	17373.302	26051.868	34731.653
$\mathbf{U}_Q^{A1}(\sigma = 0.7)$	17372.570	26050.788	34730.156
$\mathbf{U}_Q^{A1}(\sigma = 0.5)$	17372.538	26050.715	34730.105

Table 3.9: Average objective values of the problems that consider the piecewise linear ESS models.

Scenario	S_4	S_5	S_6
$\mathbf{U}_L^R$	34854.181	43567.698	52281.164
$\mathbf{U}_L^E$	34940.882	43675.605	52410.368
$\mathbf{U}_L^{A2}(\sigma = 0.7)$	34940.891	43675.616	52410.380

selected $N = 20$ to yield solutions with a maximum approximation error of $\rho = 0.001$ according to (3.19). As shown in Figure 3.7(a), Algorithm SCA-GN for $\sigma = 0.5$ and $\sigma = 0.7$ yields significantly lower execution times compared to $\mathbf{U}^X$, achieving a total time reduction of 56.9% and 70.9%. This significant time reduction is achieved despite the fact that the relaxed problem remains an MIP. The figure also indicates that increasing σ results in faster solutions because the algorithm requires fewer iterations. Table 3.8 shows the average objective values of the considered problems for $S_2 - S_4$, indicating that Problem $\mathbf{U}_Q^R$ generates solutions with lower objective values compared to $\mathbf{U}^X$ and $\mathbf{U}_Q^{A1}$ due to the relaxation violation. Interestingly, Table 3.8 depicts that Algorithm SCA-GN for $\sigma = 0.5$ and $\sigma = 0.7$ always yields better solutions compared to $\mathbf{U}^X$, despite the fact that $\mathbf{U}^X$ is almost optimal. This clearly indicate the high quality of the obtained solutions. Considering the piecewise linear ESS models, Algorithm SCA-PL for $\sigma = 0.7$ yields considerably lower execution times compared to Problem $\mathbf{U}_L^E$, as shown in Figure 3.7(b) for $S_4 - S_6$, achieving a total time reduction of 49.85%. Table 3.9 shows the average objective values of the considered problems for $S_4 - S_6$, indicating that Problem $\mathbf{U}_L^R$ yields non-exact solutions with lower objective values compared to the optimal values obtained using $\mathbf{U}_L^E$ (optimality gap = -0.24%). The table also indicates that Algorithm SCA-PL for $\sigma = 0.7$ yields almost optimal solutions with a maximum optimality gap of 0.00002%.

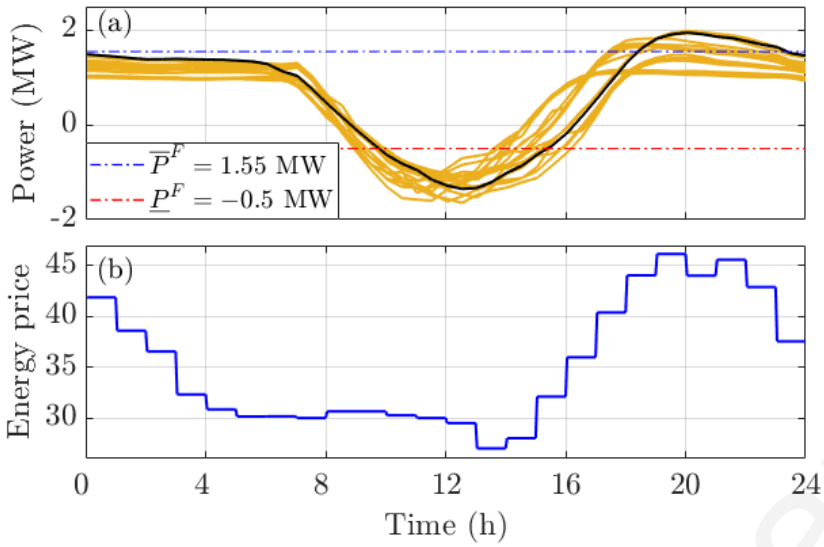

Figure 3.8: Input data: (a) net-load curves of the distribution grid and (b) energy price in €/MWh. The black load curve is used to study the ESS relaxation violation, while all curves are used to examine the algorithms performance.

3.6.2 Peak shaving and energy arbitrage

Setup. The simulation setup is composed of an ESS with usable capacity of 1.2 MWh and charging/discharging power of 2.4 MW, where the efficiencies $\eta^c = \eta^d = 0.96$ ($e^d = 0.0416$, $e^c = 0.04$) and the losses coefficient $e^q = 0.02$ are used in the piecewise linear and quadratic ESS models, respectively. Figure 3.8(a) illustrates 17 net-load curves constructed from historical data of a real distribution grid, obtained from a substation in Larnaca, Cyprus. As shown by the net-load curves, high reverse and direct power flows are presented during the noon and evening hours due to intense photovoltaic generation and high load demand, respectively. Since power violations do not occur in the real distribution transformer due to its large size, we consider a smaller transformer with power limits of $\overline{P}^F = 1.55$ MW and $\underline{P}^F = -0.5$ MW, respectively. Figure 3.8(b) depicts the electricity price for buying and selling power. The horizon is set to one day with 3-minute time intervals, the solver time limit is set to 15 minutes, and parameter W is set to 10000. Since Problems $\mathbf{S}_L^{A2}$ and $\mathbf{S}_Q^{A1}$ are convex and can be solved fast, parameter ρ is set to 0.0001, instead of 0.001, to improve the approximation error according to (3.19).

ESSs relaxation violation. This case study investigates the impact of the ESS relaxation violation on the solution of Problem PSEA, considering only the piecewise linear ESS models. Towards this direction, we solve Problems $\mathbf{S}_L^R$ and $\mathbf{S}_L^E$ using the black load curve shown in Figure 3.8(a). The optimal solution of Problem $\mathbf{S}_L^E$ and

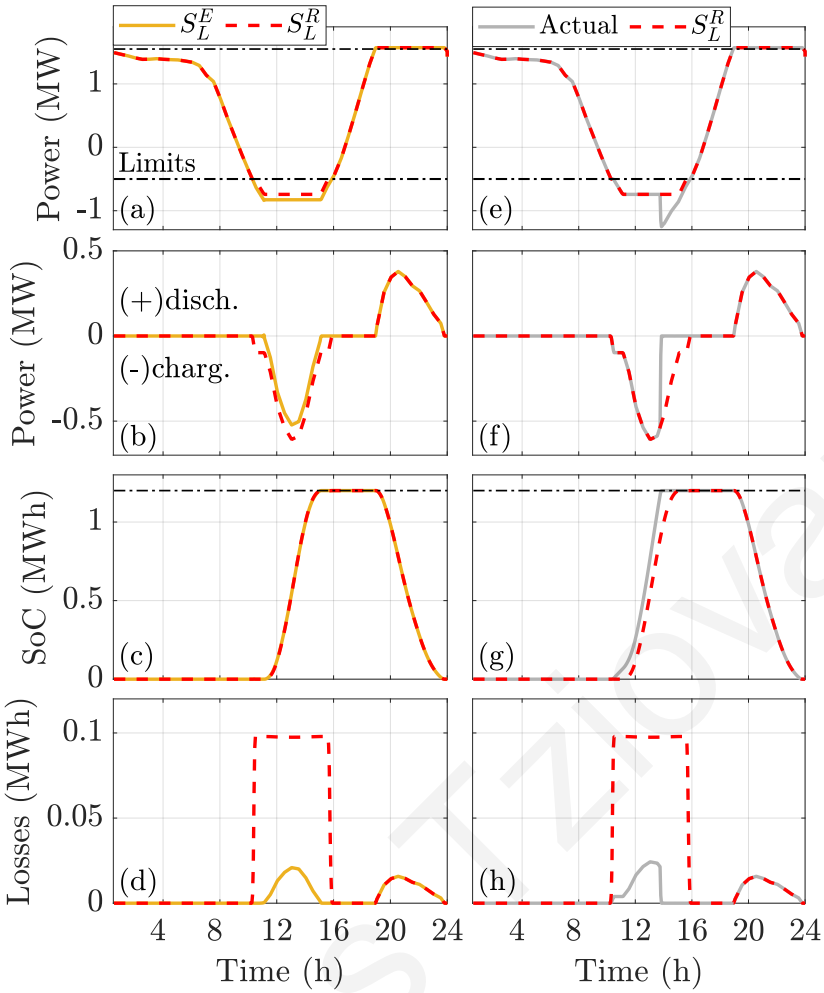

Figure 3.9: Optimization results obtained by solving Problems $\mathbf{S}_L^E$ and $\mathbf{S}_L^R$ (a)-(d) and actual results of Problem $\mathbf{S}_L^R$ considering the ESSs operating limits (e)-(h): (a) and (e) transformer power, (b) and (f) discharging/charging power, (c) and (g) ESS state-of-charge, and (d) and (h) ESS energy losses.

the solution of Problem $\mathbf{S}_L^R$, where the relaxation exactness is violated, are depicted in Figures 3.9(a)-3.9(d). Figure 3.9(a) shows a reduced reverse power flow through the transformer for Problem $\mathbf{S}_L^R$ compared to the optimal results, decreasing the transformer power violations which are penalized in objective (3.22a). As shown in Figure 3.9(b), the reduced power violations are achieved by increasing the ESS charging power; however, both problems present the same SoC in Figure 3.9(c) because increased ESS losses are depicted in Figure 3.9(d) for Problem $\mathbf{S}_L^R$ due to the ESS relaxation violation. As a result, the objective value of Problem $\mathbf{S}_L^R$ is 2585 which is 47.31% lower than the optimal value of 4906 obtained from Problem $\mathbf{S}_L^E$ (optimality gap = -47.31%).

Figures 3.9(e)-3.9(h) demonstrate the optimization results obtained from the so-

lution of Problem $\mathbf{S}_L^R$ and the actual results[5], considering an actual ESS with an integrated primary controller. As shown in Figures 3.9(e) and 3.9(f), the actual transformer power deviates from the scheduled power at time 14:00, presenting high power violations, due to the reduction of the ESS charging power. As shown in Figures 3.9(g) and 3.9(h), the primary controller limits the ESS charging power because the actual ESS SoC reached its maximum value before the scheduled SoC due to the reduced actual losses. As a result, the ESS relaxation violation causes a mismatch between scheduled and actual operation of the real system, increasing the peak power violations, from 0.34 MW to 0.75 MW, and reducing the actual arbitrage profit, from 15.54 € to 14.78 €, compared to the optimal solution. To protect the transformer, high peak power violations can be reduced by applying RES power curtailments in real operation, but this action is undesirable because it reduces the RES penetration in the power systems.

Algorithms performance. This case study investigates the performance of the proposed algorithms for the 17 net-load curves. Considering the piecewise-linear ESS models, Table 3.10 demonstrates that Problems $\mathbf{S}_L^R$ and $\mathbf{S}_L^{A2}$ yield small execution times compared to the high times of the non-convex Problem $\mathbf{S}_L^E$. However, Problem $\mathbf{S}_L^R$ yields infeasible solutions with an average optimality gap of -37.93% due to the relaxation violation. The maximum time of $\mathbf{S}_L^E$ indicates that the considered time limit of 60-minutes is exceeded for $\mathbf{S}_L^E$ in some scenarios, yielding sub-optimal solutions. Therefore, Algorithm SCA-PL for $\sigma = 0.5$ generated slightly better solutions compared to $\mathbf{S}_L^E$. Table 3.10 also indicates that Algorithm SCA-PL generates solutions with an average execution time of 0.039 minutes, achieving a speedup of 368 (368x) times compared to the average time (14.35 minutes) of Problem $\mathbf{S}_L^E$. Considering the quadratic ESS models, Table 3.10 depicts the small execution times of the convex Problems $\mathbf{S}_Q^R$ and $\mathbf{S}_Q^{A1}$ compared to the high times of the non-convex Problem $\mathbf{S}^X$; however, Problem $\mathbf{S}_Q^R$ generates non-exact solutions. As shown in Table 3.10, Algorithm SCA-GN and Problem $\mathbf{S}^X$ for $N = 20$ yield similar average objective values, presenting a difference of 0.06%. Algorithm SCA-GN generates solutions with an average execution time of 0.051 minutes, achieving a speedup of more than 1176 (1176x) times compared to the average time of Problem $\mathbf{S}^X$.

[5]The actual results are calculated by applying the charging/discharging decisions of the optimization solution in an actual ESS with an integrated primary controller that ensures the ESS power and energy limits.

Table 3.10: Execution times and objective values of the problems that consider piecewise linear and quadratic ESS models.

	Max. time (min)	Avg. time (min)	Avg. obj. value
$\mathbf{S}_L^R$	0.005	0.003	3568.042
$\mathbf{S}_L^E$	60	14.35	5748.723
$\mathbf{S}_L^{A2}(\sigma = 0.5)$	0.053	0.039	5748.514
$\mathbf{S}_Q^R$	0.017	0.007	3217.606
$\mathbf{S}^X(N = 20)$	60	60	6002.267
$\mathbf{S}_Q^{A1}(\sigma = 0.5)$	0.082	0.051	6006.194

3.7 Conclusions

This work developed two convexification algorithms that yield fast and high-quality feasible solutions when the derived solution using relaxed ESS models is not exact. The first algorithm handles general power loss functions, while the second specialized algorithm enhances performance when piecewise-linear loss functions are used. The proposed algorithms are applied to the UC and PSEA problems considering piecewise-linear and quadratic loss functions. Simulation results indicate the capability of the proposed algorithms to yield almost optimal, if not optimal, solutions with significantly lower execution times compared to state-of-the-art solvers that utilize exact ESS models. Specifically, the proposed algorithms reduce the average execution time by 50% for the UC problem, which remains nonconvex even upon relaxation, and achieve a 2-3 orders of magnitude speedup for the PSEA problem, which becomes convex upon relaxation.

Chapter 4

Energy management of photovoltaic and battery storage systems in active distribution grids

The evolution of power distribution grids from passive to active systems creates reliability and efficiency challenges to the distribution system operators. In this chapter, an energy management and control scheme for managing the operation of an active distribution grid with prosumers is proposed. A multi-objective optimization model to minimize (i) the prosumers electricity cost and (ii) the cost of the grid energy losses, while guaranteeing safe and reliable grid operation is formulated. This is done by determining the active and reactive power set-points of the photovoltaic and storage systems integrated in the grid buildings. The resulting optimization model is non-convex, thus a convex second-order cone program is developed by appropriately relaxing the non-convex constraints which yields optimal results in most operating conditions. The convexified model is further utilized to develop an algorithm that yields feasible solutions to the non-convex problem under any operating conditions. Moreover, a second novel algorithm to find the operating point that provides fairness between the prosumers and the grid costs is proposed. Simulation results demonstrate the effectiveness and superiority of the proposed scheme in managing an industrial distribution grid compared to a self-consumption approach.

4.1 Introduction

The integration of PV systems into the power system is expected to continue, with the aim to achieve full decarbonization of Europe's energy supply by 2050, according to the climate and energy strategy of the European Commission [2]. However, in cases in which massive PVs are integrated within a distribution grid, the stability and power quality of the grid is threatened mainly due to the uncontrollability of PV generation [44]. BESSs can be used along with PV systems to compensate the negative effects of intermittent PV generation. BESSs constitute an emerging technology that enables optimized management of the energy produced by the PVs that can be utilized for peak shaving, load levelling, and reactive power support. Moreover, BESSs create new energy market opportunities for prosumers (users who consume, produce, store and sell energy), who are able to optimize their electricity management according to the electricity market price information [45]. However, since the prosumer actions can affect the safe operation of the LV distribution grid, the DSO and prosumers should be coordinated. This chapter aims to develop an energy management and control strategy to maximize the prosumers profits in active distribution grids with massive integration of PVs-BESSs, while maintaining the safe, reliable and cost-effective grid operation. In the proposed strategy, power flow constraints are integrated to ensure operating conditions within regulation limits, while reactive power support is provided by the PVs-BESSs.

Energy management and control strategies for voltage control in MV distribution grids are presented in [46, 47]. These strategies control the active and reactive power of the distributed generation to guarantee a safe and reliable grid operation. Similarly, strategies for voltage control in LV distribution grids determine the active and reactive power set-points of PV inverters in residential systems [48, 49]. In addition to PV inverters, BESS inverters can also provide voltage control in LV and MV distribution grids by controlling their active and reactive power set-points [50–53]. These works do not consider the profit maximization of the prosumers at the building level in energy market environments. Multi-objective optimization schemes based on the weighted sum method for the system operation are presented in [46–49]; however, none of these works demonstrates the Pareto front to examine the trade-off of different objectives.

Energy management schemes at the building level to minimize the prosumer

electricity cost under a time-based pricing are proposed in [54, 55]. These do not consider reactive power support and the grid safety limits are ignored. Furthermore, energy management schemes at the grid level are presented in [56–60], where works in [56, 57, 60] optimize the electricity usage of the prosumers in LV distribution grids, while [58, 59] minimize the operational cost of multiple microgrids which are connected to the MV distribution grid. Note that reactive power support is not provided by the PV-BESS systems in [56, 57, 59] and the safe and reliable grid operation is not considered in [58, 60], since power flow constraints are ignored.

This chapter proposes a centralized energy management and control (CEMC) scheme to minimize (i) the prosumers electricity cost and (ii) the cost of the grid energy losses, while satisfying the safe and reliable grid operation. Towards this direction, a multi-objective optimization model to determine the active and reactive power set-points of the PV-BESS systems by minimizing the considered objectives is formulated. The safe grid operation is maintained through the integration of the power flow constraints in the optimization model, and reactive power support provided by PV-BESS inverters has a vital role in achieving reduced power losses and voltage regulation.

The resulting optimization model is non-convex, hence the underlying problem is challenging to solve; thus, convexification is used to transform the non-convex model to a convex SOCP. Specifically, a convex relaxation of the power flow constraints as well as a convex relaxation of the BESS power losses are used. Also, complementarity constraints that support different pricing schemes in the objective function are shown to hold in the considered problem and are eliminated from the formulation. The convex SOCP model allows computing optimal solutions under normal operating conditions; it can yield, however, infeasible solutions under "extreme" operating conditions. Therefore, an algorithm to provide a feasible solution when the relaxed SOCP model is non-exact is developed. In addition, a second novel algorithm to provide fairness between the prosumers and grid costs by minimizing the absolute difference between the gain losses of the two objectives[1] is proposed.

The effectiveness of the proposed CEMC scheme is compared to a self-consumption scheme, and simulation results validate the prosumers and grid cost-effective op-

[1]We define the gain loss of an objective as the difference between the value of the particular objective, obtained when the two objectives are conflicting, and its minimum value, obtained when the other objective is not present in the formulation.

eration, as well as the grid reliability. Moreover, the performance of the proposed convex BESS model is compared with other BESS models, presented in the literature, in terms of energy losses and computational speed.

The rest of the chapter is organized as follows. Section 4.2 describes the system architecture, while Section 4.3 formulates the considered problem. The proposed solution methodology and the simulation results are presented in Sections 4.4 and 4.5, respectively. Conclusions are given in Section 4.6.

4.2 System architecture

We consider an industrial LV distribution grid that connects the industrial buildings (the prosumers) to an LV feeder through the distribution lines, as shown in Figure 4.1. The power grid under consideration is radial, hence its graph is represented by a tree. Let the tree graph $\mathcal{G} = (\mathcal{N}, \mathcal{E})$ denote the power grid, where $\mathcal{N} = \{1, ..., N\}$ denote the set of grid buses and $\mathcal{E} = \{1, ..., E\}$ the set of grid lines that connect two buses. The LV feeder bus is the root of the tree. Let $\mathcal{B} \in \mathcal{N}$ denote the set of buses that are connected to the buildings; $\mathcal{M}_k \in \mathcal{N}$ the set of all buses that are children of bus k; $\mathcal{T} = \{1, ..., T\}$ the considered time horizon and ΔT the time-slot length in hours. For example, $\Delta T = 1/4$ denotes 15-minute time intervals. The active and reactive power flows of the grid line $(i, k) \in \mathcal{E}$ are given by $P_{t,ik}$ and $Q_{t,ik}$, $t \in \mathcal{T}$, with positive/negative values denoting direct/reverse power flows, respectively. Furthermore, the active and reactive power exchange between the building at bus $k \in \mathcal{B}$ and the grid are denoted by $P^G_{t,k}$ and $Q^G_{t,k}$, with positive/negative values denoting power consumption/generation of the buildings, respectively. The square of the voltage at each bus $n \in \mathcal{N}$ is denoted by v_n.

Three building models are considered in this chapter: (i) the *PV-BESS prosumer* consisting of an AC-coupled PV-BESS system, and a load; (ii) the *PV prosumer* comprising of a PV and a load; and (iii) the *consumer* which includes only a load. Thus, $P^G_{t,k}$ and $Q^G_{t,k}$ are set according to the building model. The PV-BESS prosumer model is illustrated in Figure 4.2. Note that $P^G_{t,k}$ and $Q^G_{t,k}$ can be adjusted by controlling the PV active and reactive power, $P^P_{t,k}$ and $Q^P_{t,k}$, and the BESS active and reactive power, $P^B_{t,k}$ and $Q^B_{t,k}$. The building load, $P^L_{t,k}$ and $Q^L_{t,k}$, must always be supplied by the power grid and/or the PV-BESS system, as indicated by the arrows in Figure 4.2, denoting the power flow directions. Note that $P^B_{t,k}$ denotes discharging (charging

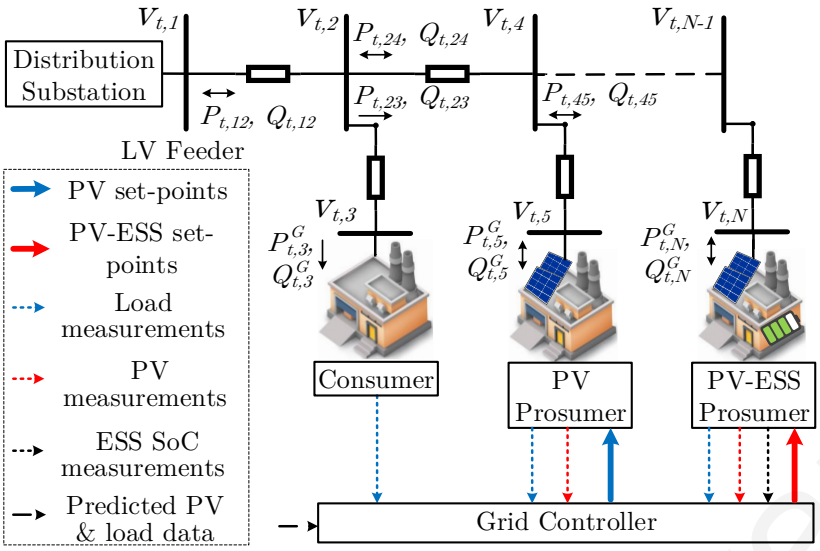

Figure 4.1: Energy management and control of an industrial LV distribution grid.

resp.) power when $P^B_{t,k} \geq 0$ ($P^B_{t,k} < 0$), and $Q^P_{t,k}$ and $Q^B_{t,k}$ denote reactive power production (consumption) when they are positive (negative). Moreover, the PV prosumer and the consumer models are supported by setting $P^B_{t,k} = Q^B_{t,k} = 0$ and $P^B_{t,k} = Q^B_{t,k} = P^P_{t,k} = Q^P_{t,k} = 0$, respectively.

Under the proposed system structure, a grid-level controller (GC) is utilized to realize the CEMC scheme in a centralized manner, as described in Sections 4.3 and 4.4. As shown in Figure 4.1, the GC regulates the power flows through the distribution grid, based on the predicted PV generation and load demand of prosumers, by setting the grid-buildings power exchange through the scheduling of PVs-BESSs power set-points. The prosumers execute the control signals sent by the GC regarding the PVs-BESSs active and reactive power set-points through their inverters. Due to the difference between predicted and actual PV generation, the PV inverters are allowed to operate at their maximum power point based on the actual available PV generation, except from the cases where PV power curtailments are applied by the GC. In these cases, the PV generation is limited to the PV active power set-point defined by the GC through the online reconfiguration of the inverter maximum power. The proposed control architecture is applied in a model predictive control (MPC) fashion, where at the end of every MPC control-step the GC defines the next PVs-BESSs power set-points. To achieve this, in every MPC control-step the GC uses the latest BESSs SoC measurements and updates the predicted PV and load data using the latest actual PV generation and load demand measurements of the buildings.

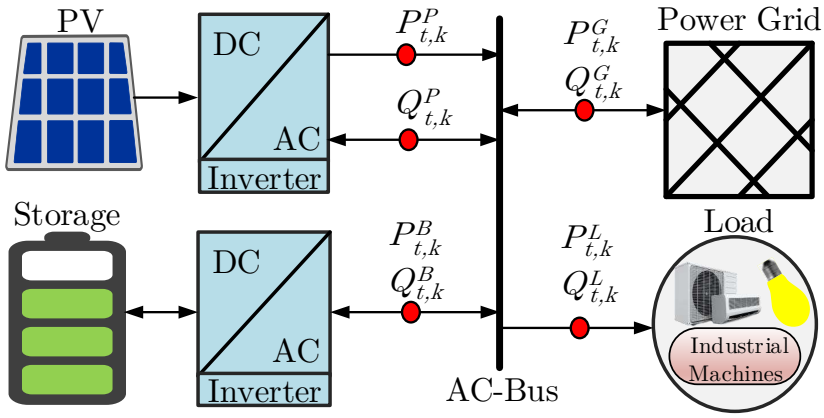

Figure 4.2: The PV-BESS prosumer model.

4.3 Problem statement

This section contains the formulation of the optimization problem associated with the proposed CEMC scheme according to the system architecture described in Section 4.2. In addition, the objective function and the constraints of the problem are presented.

4.3.1 Multi-objective function

The considered CEMC scheme is a multi-objective optimization problem with two objective functions. The first objective describes the prosumers electricity cost in € by incorporating the cost of buying and selling energy

$$F_1(\mathbf{P}^b, \mathbf{P}^s) = \sum_{t\in\mathcal{T}} \sum_{k\in\mathcal{B}} (c^b_t P^b_{t,k} - c^s_t P^s_{t,k}) \Delta T, \tag{4.1a}$$

subject to the conditions

$$P^b_{t,k}, P^s_{t,k} \geq 0, \quad \forall t, k \in \mathcal{B}, \tag{4.1b}$$

$$P^b_{t,k} \perp P^s_{t,k}, \quad \forall t, k \in \mathcal{B}, \tag{4.1c}$$

where the variables $P^b_{t,k}$ and $P^s_{t,k}$ denote the buying and selling power of the building at bus k at time t in kW, respectively, and the parameters c^b_t and c^s_t denote the corresponding cost coefficients in €/kWh such that $c^b_t \geq c^s_t$. $\mathbf{P}^b$ and $\mathbf{P}^s$ are the vector-forms of the variables $P^b_{t,k}$ and $P^s_{t,k}$, for all $k \in \mathcal{B}$ and $t \in \mathcal{T}$, respectively. Note also that

$$P^G_{t,k} = P^b_{t,k} - P^s_{t,k}, \quad k \in \mathcal{B}, \forall t \in \mathcal{T}. \tag{4.2}$$

The variables $P^b_{t,k}$ and $P^s_{t,k}$ are used to support pricing schemes where the cost of buying and selling power can be different, while satisfying constraint (4.2). The non-convex complementarity constraint in (4.1c) restricts the ability to simultaneously buy and sell power to the grid [61]. Section 4.4.1 indicates when the complementarity constraint can be eliminated.

The second objective quantifies the cost of energy losses at the grid lines in € and is given by

$$F_2(\mathbf{L}) = \sum_{t\in\mathcal{T}} \sum_{(i,k)\in\mathcal{E}} (r_{ik} l_{t,ik} c^b_t)\Delta T, \tag{4.3}$$

where $l_{t,ik}$ denotes the square of the current flow in line $(i,k) \in \mathcal{E}$ at time $t \in \mathcal{T}$, and r_{ik} denotes the line resistance. $\mathbf{L}$ is the vector-form of $l_{t,ik}$, for all $t \in \mathcal{T}$ and $(i,k) \in \mathcal{E}$.

The two objectives of the proposed CEMC scheme are transformed into an aggregated single objective by employing the widely used weighted sum method [21, 46–49]

$$F(w) = (1-w)F_1(\mathbf{P}^b, \mathbf{P}^s) + wF_2(\mathbf{L}), \tag{4.4}$$

where $w \in [0,1]$ is a weighting parameter that controls the tradeoff between the two objectives. Note that the two objectives are conflicting because the buildings-grid power exchange needs to be restrained in order to minimize the grid losses cost, which negatively affects the prosumer profits.

More sophisticated multi-objective optimization methods can also be employed for the considered biobjective problem, such as the adaptive weighted sum and normal boundary intersection (NBI) methods [62–64]. Using the NBI method a "knee" solution, which presents a good sense of "compromise" between the objectives, can be implicitly obtained without constructing the Pareto front [62]. In this chapter we explicitly find the tradeoff by minimizing the absolute difference between the gain losses of the two objectives.

4.3.2 Constraints

Power flow constraints

The power flow equations are conventionally formulated as sine and cosine functions of the voltage and current angles resulting in non-convex optimization problems. For radial grids, the branch-flow model [46, 65, 66] can equivalently be used; this

eliminates the voltage and current angles, yielding the equations

$$P_{t,ik} = r_{ik} l_{t,ik} + P^G_{t,k} + \sum_{m \in \mathcal{M}_k, m \neq i} P_{t,km}, \quad \forall t, (i,k) \in \mathcal{E}, \tag{4.5a}$$

$$Q_{t,ik} = x_{ik} l_{t,ik} + Q^G_{t,k} + \sum_{m \in \mathcal{M}_k, m \neq i} Q_{t,km}, \quad \forall t, (i,k) \in \mathcal{E}, \tag{4.5b}$$

$$\begin{aligned} v_{t,k} &= v_{t,i} - 2(r_{ik} P_{t,ik} + x_{ik} Q_{t,ik}) \\ &+ (r^2_{ik} + x^2_{ik}) l_{t,ik}, \quad \forall t, (i,k) \in \mathcal{E}, \end{aligned} \tag{4.5c}$$

$$l_{t,ik} v_{t,i} = P^2_{t,ik} + Q^2_{t,ik}, \quad \forall t, (i,k) \in \mathcal{E}. \tag{4.5d}$$

Eq. (4.5a) defines the active power flow through line (i,k) as the summation of the line power losses, the power exchange $P^G_{t,k}$ at bus k, if $k \in \mathcal{B}$, and the power flows through the connected lines. Similarly, the reactive power flow is defined in Eq. (4.5b), where x_{ik} is the line reactance. Eqs. (4.5c)-(4.5d) associate the power flows with the bus voltages and line currents. Lower/upper limits of the square of the voltage, $\underline{v}_j$ and $\overline{v}_j$, are set as

$$\underline{v}_j \leq v_{t,j} \leq \overline{v}_j, \quad \forall t, j \in \mathcal{N}. \tag{4.6}$$

For example, if the voltages must vary between -10% and +10% from their nominal value, then $\underline{v}_j = 0.9^2$ and $\overline{v}_j = 1.1^2$ p.u. Despite the elimination of the sine and cosine functions, the branch-flow model is still non-convex due to the presence of the constraint (4.5d).

Buildings active power management

The active power balance of a building, as illustrated in Figure 4.2, is given by

$$P^P_{t,k} + P^B_{t,k} + P^G_{t,k} = P^L_{t,k}, \quad \forall t, k \in \mathcal{B}, \tag{4.7}$$

where $P^L_{t,k}$ denotes the building predicted active load demand in kW. PV power curtailments are applied when the PV power differs from the predicted PV generation, $\overline{P}^P_{t,k}$, and are set as

$$0 \leq P^P_{t,k} \leq \overline{P}^P_{t,k}, \quad \forall t, k \in \mathcal{B}. \tag{4.8}$$

The BESS SoC in kWh, $C^B_{t,k}$, is varied according to the discharging/charging power and the BESS power losses, $P^{loss}_{t,k}$, as expressed by

$$C^B_{t+1,k} = C^B_{t,k} + \Delta T(-P^B_{t,k} - P^{loss}_{t,k}), \quad \forall t, k \in \mathcal{B}. \tag{4.9}$$

The bounds of the BESS SoC, $\underline{C}_k^B$ and $\overline{C}_k^B$, and the discharging/charging power limitations, $\overline{P}_k^B$ and $\underline{P}_k^B$, are given by

$$\underline{C}_k^B \leq C_{t,k}^B \leq \overline{C}_k^B, \quad C_{0,k}^B = I_k^B, \quad \forall t, k \in \mathcal{B}, \tag{4.10a}$$

$$-\underline{P}_k^B \leq P_{t,k}^B \leq \overline{P}_k^B, \quad \forall t, k \in \mathcal{B}, \tag{4.10b}$$

where I_k^B denote the initial SoC value.

BESS power losses

Two linear power losses models, $P_{t,k}^{loss,c}$ and $P_{t,k}^{loss,d}$, are used to represent the BESS charging and discharging power losses, respectively, and formulated as

$$P_{t,k}^{loss,d} = e_k^d P_{t,k}^B, \quad P_{t,k}^{loss,c} = (-e_k^c) P_{t,k}^B \quad \forall t, k \in \mathcal{B}. \tag{4.11}$$

These models are dependent on the BESS charging/discharging power and the associated positive losses coefficients, e_k^c and e_k^d, respectively. Note that $e_k^d = 1/\eta_k^d - 1$ and $e_k^c = 1 - \eta_k^c$, where η_k^c and η_k^d are the charging/discharging (one-way) efficiency, respectively. $P_{t,k}^{loss,d}$ provides positive (negative) power losses when $P_{t,k}^B \geq 0$ ($P_{t,k}^B < 0$). In contrast, $P_{t,k}^{loss,c}$ provides positive (negative) power losses when $P_{t,k}^B < 0$ ($P_{t,k}^B \geq 0$). Thus, the BESS power losses are defined as the maximum of the two power losses models, that is

$$P_{t,k}^{loss} = \max(P_{t,k}^{loss,d}, P_{t,k}^{loss,c}), \quad \forall t, k \in \mathcal{B}. \tag{4.12}$$

Note that constraint (4.12) is non-convex, and logical constraints with binary variables are needed to represent it. Constraints (4.9)-(4.12) represent the exact version of the piecewise linear ESS model presented in Section 3.3.

Buildings reactive power management

The reactive power balance in the building, as shown in Figure 4.2, is set as

$$Q_{t,k}^G + Q_{t,k}^P + Q_{t,k}^B = Q_{t,k}^L, \quad \forall t, k \in \mathcal{B}, \tag{4.13}$$

where $Q_{t,k}^L$ denotes the building predicted reactive power demand in kVar. The PV-BESS inverter reactive power, $Q_{t,k}^P$ and $Q_{t,k}^B$ in kVar, is restricted by the inverter operation in active power, $P_{t,k}^P$ and $P_{t,k}^B$ in kW, and its maximum apparent power, $\overline{S}_k^P$ and $\overline{S}_k^B$ in kVA, according to the SOCP constraints:

$$(P_{t,k}^B)^2 + (Q_{t,k}^B)^2 \leq (\overline{S}_k^B)^2, \quad \forall t, k \in \mathcal{B}, \tag{4.14a}$$

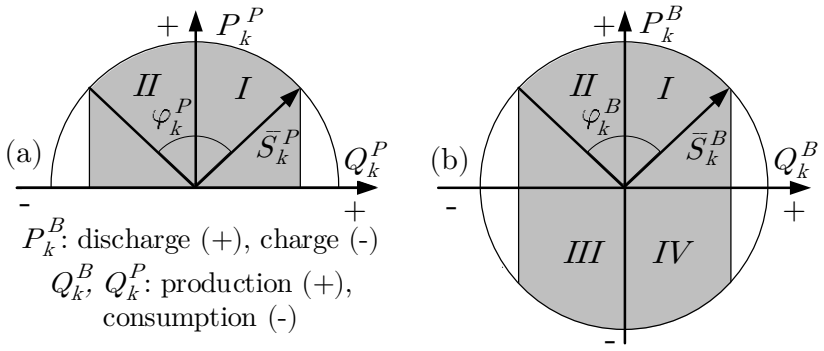

Figure 4.3: The operating regions of (a) the PV and (b) the BESS inverters are given by the shaded area.

$$(P_{t,k}^P)^2 + (Q_{t,k}^P)^2 \leq (\bar{S}_k^P)^2, \quad \forall t, k \in \mathcal{B}. \tag{4.14b}$$

The inverter limits in reactive power are given by

$$-\bar{S}_k^B \sin(\varphi_k^B) \leq Q_{t,k}^B \leq \bar{S}_k^B \sin(\varphi_k^B), \quad \forall t, k \in \mathcal{B}, \tag{4.15a}$$

$$-\bar{S}_k^P \sin(\varphi_k^P) \leq Q_{t,k}^P \leq \bar{S}_k^P \sin(\varphi_k^P), \quad \forall t, k \in \mathcal{B}, \tag{4.15b}$$

where the angle coefficients φ_k^P and φ_k^B are defined by the PV and BESS inverter power factor limits. Figure 4.3 depicts the feasible operating regions of the inverters in terms of active and reactive power.

The considered MPC optimization problem that is solved by the GC at the end of every MPC control-step is summarized as

$$\mathbb{P}_{\mathrm{O}}(w): \begin{cases} \min \text{ Objective (4.4)} \\ \text{s.t.: Constraints (4.1b)} - \text{(4.1c)}, \text{(4.2)}, \text{(4.5a)} - \text{(4.15b)}, \end{cases}$$

with decision variables the active and reactive powers, $P_{t,k}^G$, $P_{t,k}^b$, $P_{t,k}^s$, $P_{t,k}^P$, $P_{t,k}^B$, $Q_{t,k}^G$, $Q_{t,k}^P$, $Q_{t,k}^B$, $\forall t \in \mathcal{T}$, $k \in \mathcal{B}$, the BESS power losses and SoC, $P_{t,k}^{loss}$, $P_{t,k}^{loss,d}$, $P_{t,k}^{loss,c}$, $C_{t,k}^B$, $\forall\, t \in \mathcal{T}$, $k \in \mathcal{B}$, the power flows and the square of the line currents, $P_{t,ik}$, $Q_{t,ik}$, $l_{t,ik}$, $\forall\, t \in \mathcal{T}$, $(i,k) \in \mathcal{E}$, as well as the square of the bus voltages, $v_{t,j}$, $\forall t \in \mathcal{T}$, $j \in \mathcal{N}$. Note that decision variables $P_{t,k}^P$, $P_{t,k}^B$, $Q_{t,k}^P$, $Q_{t,k}^B$ denote the active and reactive power set-points submitted to the PV-BESS inverters according to the system architecture of Section 4.2. Problem $\mathbb{P}_{\mathrm{O}}(w)$ considers a single-phase system and can be used for balanced systems, using the single-phase equivalent [46]. Problem $\mathbb{P}_{\mathrm{O}}(w)$ is non-convex, and hence challenging to solve due to the presence of the non-convex constraints (4.1c), (4.5d) and (4.12).

4.4 Solution methodology

In this section the non-convex problem $\mathbb{P}_O(w)$ is relaxed to a convex SOCP optimization problem and an algorithm to obtain feasible solutions under any operating condition is developed. Moreover, a second algorithm to define the best trade-off between the two conflicting objectives is proposed.

4.4.1 Convexifying Problem $\mathbb{P}_O(w)$

Relaxation of the power flow constraints

A convex SOCP relaxation of the non-convex constraint in (4.5d) is proposed in [46, 65, 66], yielding

$$l_{t,ik} v_{t,i} \geq P_{t,ik}^2 + Q_{t,ik}^2, \quad \forall t, (i,k) \in \mathcal{E}. \tag{4.16}$$

A sufficient condition for the relaxation exactness, where the equality is attained in Eq. (4.16), requires to have a strictly increasing objective function in the line currents ($l_{t,ik}$) [66]. Although the second objective, $F_2(\mathbf{L})$, is strictly increasing in $l_{t,ik}$, the presence of the first objective, $F_1(\mathbf{P}^b, \mathbf{P}^s)$, in objective (4.4), might affect the relaxation exactness.

Relaxation of the BESS power losses

The non-convex constraint in (4.12) is relaxed to the convex constraint:

$$P_{t,k}^{loss} \geq \max(P_{t,k}^{loss,d}, P_{t,k}^{loss,c}), \quad \forall t, k \in \mathcal{B}, \tag{4.17}$$

which can be represented by the affine constraints:

$$P_{t,k}^{loss} \geq e_k^d P_{t,k}^B, \quad \forall t, k \in \mathcal{B}, \tag{4.18a}$$

$$P_{t,k}^{loss} \geq -e_k^c P_{t,k}^B, \quad \forall t, k \in \mathcal{B}. \tag{4.18b}$$

Upper bounds on the maximum power losses, defined by the BESS maximum charging/discharging power and losses coefficients, are set as

$$P_{t,k}^{loss} \leq e_k^c \underline{P}_k^B + \alpha_k (P_{t,k}^B + \underline{P}_k^B), \quad \forall t, k \in \mathcal{B}, \tag{4.19}$$

where constant $\alpha_k = (e_k^d \overline{P}_k^B - e_k^c \underline{P}_k^B)/(\overline{P}_k^B + \underline{P}_k^B)$, $\forall k \in \mathcal{B}$. Figure 4.4 shows the feasible region of the power losses defined by Eqs. (4.18a)-(4.19). Note that the minimization of the function $F_1(\mathbf{P}^b, \mathbf{P}^s)$ is an incentive to satisfy the relaxation exactness, because

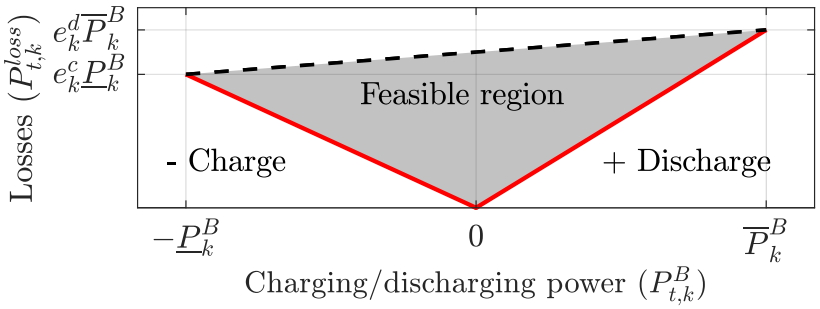

Figure 4.4: BESS power losses convex relaxation. The losses are given as function of the charging/discharging power. The red solid lines show the losses when the relaxation is exact, and the dashed line provides upper bounds.

higher power losses cause prosumers profit losses. Constraints (4.9)-(4.10b), (4.18a)-(4.19) represent the relaxed version of the ESS model presented in Section 3.3.

Elimination of complementarity constraints

According to (4.1c), the variables $P^b_{t,k}$ and $P^s_{t,k}$ should be complementary to each other. We now show that the structure of Problem $\mathbb{P}_O(w)$ automatically ensures that buying and selling power at the same time does not occur, hence the non-convex complementarity constraint (4.1c) can be eliminated.

Because $c^s_t \leq c^b_t$ we can write that $c^b_t = c^s_t + c$ for $c \geq 0$. It is also true that variables $P^b_{t,k}$ and $P^s_{t,k}$ appear as the difference $P^G_{t,k} = P^b_{t,k} - P^s_{t,k}$ in all constraints; they only appear separately in the first objective (4.1a) in which we have that:

$$\sum_{t\in\mathcal{T}}\sum_{k\in\mathcal{B}}(c^b_t P^b_{t,k} - c^s_t P^s_{t,k})\Delta T = \sum_{t\in\mathcal{T}}\sum_{k\in\mathcal{B}}(c^s_t P^G_{t,k} + c P^b_{t,k})\Delta T.$$

This implies that for a fixed positive or negative value of $P^G_{t,k}$ we aim to minimize $P^b_{t,k}$. Hence, when $P^G_{t,k} \geq 0$ and $P^G_{t,k} < 0$ the best objective is obtained for $P^G_{t,k} = P^b_{t,k}$, $P^s_{t,k} = 0$ and $P^G_{t,k} = -P^s_{t,k}$, $P^b_{t,k} = 0$, respectively. This argument shows that the complementarity constraint is automatically satisfied for Problem $\mathbb{P}_O(w)$.

Taking all convexifications into account yields:

$$\mathbb{P}_R(w): \begin{cases} \text{min Objective (4.4)} \\ \text{s.t.: Constraints (4.1b), (4.2), (4.5a) – (4.5c),} \\ \text{(4.6) – (4.10b), (4.13) – (4.15b), (4.16), (4.18a) – (4.19).} \end{cases}$$

Problem $\mathbb{P}_R(w)$ is a relaxed version of Problem $\mathbb{P}_O(w)$; hence, it provides a lower-bound solution to the latter. Due to the presence of (4.14a), (4.14b) and (4.16) the

Algorithm 3 : Feasible Solution to Problem $\mathbb{P}_O(w)$

1: **Input:** w.
2: Solve $\mathbb{P}_R(w)$ to obtain $\mathbf{x}_w$.
3: **if** $\mathbb{P}_R(w)$ is feasible **then**
4: Return $\mathbf{x}^* = \mathbf{x}_w$.
5: **else**
6: **Init.** $w_l = w$, $w_u = 1$.
7: **while** $(w_u - w_l) \geq \sigma$ **do**
8: Set $w = (w_u + w_l)/2$;
9: Solve $\mathbb{P}_R(w)$ to obtain $\mathbf{x}_w$;
10: **if** $\mathbb{P}_R(w)$ is feasible **then**
11: Set $w_u = w$, $\hat{\mathbf{x}} = \mathbf{x}_w$, $\hat{w} = w$.
12: **else**
13: Set $w_l = w$.
14: Return $\hat{\mathbf{x}} = \mathbf{x}_w$ and $\hat{w}$

problem is a convex SOCP; hence, it can be fast and reliably solved for real-size distribution grids. Hereafter, the solution of Problem $\mathbb{P}_R(w)$ will be denoted with $\mathbf{x}_w$.

4.4.2 Obtaining feasible solutions to Problem $\mathbb{P}_O(w)$

The solution of Problem $\mathbb{P}_R(w)$ for a given w results in three cases with regards to the exactness of the non-convex constraints (4.5d) and (4.12) that need to be examined.

1. If both constraints (4.16) and (4.17) are tight (exact relaxation), the solution of Problem $\mathbb{P}_R(w)$ is optimal for $\mathbb{P}_O(w)$.

2. If constraint (4.16) is tight but (4.17) is not, the solution of Problem $\mathbb{P}_R(w)$ is feasible and provides an upper-bound for $\mathbb{P}_O(w)$.

3. If constraint (4.16) is loose (non-exact relaxation), the solution of Problem $\mathbb{P}_R(w)$ is infeasible for $\mathbb{P}_O(w)$.

Algorithm 3 summarizes the proposed procedure to find a feasible solution for Problem $\mathbb{P}_O(w)$ for a given w. Initially, Problem $\mathbb{P}_R(w)$ is solved (Line 2); the obtained solution is the optimal solution for Problem $\mathbb{P}_O(w)$ if it satisfies constraint (4.16) (Lines 3-4). Otherwise, the bisection method is employed to find the smallest weight

$\hat{w} > w$ for which the solution of $\mathbb{P}_R(w)$ is tight for constraint (4.16) (Lines 5-13). The algorithm is based on the observation that higher values of w benefit the second objective, $F_2(\mathbf{L})$, causing to have a strictly increasing objective function in the line currents ($l_{t,ik}$), which is a sufficient condition for the tightness of the relaxed power flow constraint (4.16) [65, 66]. The simulation results in Section 4.5 suggest that the solution of $P_R(w)$ is non-optimal only under "extreme" operating conditions with high reverse-power flows in the grid. Even under these conditions, Algorithm 3 yields close-to-optimal results. In Algorithm 3, the bisection method is used to provide fast convergence to the operating point $\hat{w}$, providing a good quality feasible solution, $\hat{\mathbf{x}}$, for weight w. This method halves the searching space ($w_u - w_l$) at each iteration, converging to $\hat{w}$ in $\log_2((1-w)/\sigma)$ iterations, where σ is the bisection tolerance.

4.4.3 Best objective trade-off solution

Algorithm 3 solves Problem $\mathbb{P}_O(w)$ when w is known. This section proposes a novel algorithm, Algorithm 4, to provide a solution to Problem $\mathbb{P}_O$ when w is undefined. This is achieved by finding the operating point, w^*, for which Problem $\mathbb{P}_R(w^*)$ is feasible and the absolute difference of the gain losses of the two objectives is minimized.

Let $\mathbf{P}^b_w$, $\mathbf{P}^s_w$ and $\mathbf{L}_w$ denote the vectors $\mathbf{P}^b$, $\mathbf{P}^s$ and $\mathbf{L}$ derived from the solution of $\mathbb{P}_R(w)$, for $w \in [0,1]$. Then, $\underline{F}_1 = F_1(\mathbf{P}^b_0, \mathbf{P}^s_0)$ and $\underline{F}_2 = F_2(\mathbf{L}_1)$ denote the minimum values of the objectives in Eq. (4.4), $\forall\, w \in [0,1]$. The *prosumers gain loss*, G^p, and *grid gain loss*, G^g, are defined as

$$G^p(w) = F_1(\mathbf{P}^b_w, \mathbf{P}^s_w) - \underline{F}_1, \tag{4.20}$$

$$G^g(w) = F_2(\mathbf{L}_w) - \underline{F}_2. \tag{4.21}$$

G^p and G^g indicate the prosumers electricity cost and grid losses cost increments compared to the minimum values, respectively. Algorithm 4 aims to find the operating point w^* that minimizes $|G^p(w) - G^g(w)|$. Ideally, Algorithm 4 provides an operating point that equalizes the gain losses of the two objectives, i.e., $G^p(w^*) = G^g(w^*)$.

Note that $G^p(w) \in [0, G^p(1)]$ and $G^g(w) \in [0, G^g(0)]$, for $w \in [0,1]$. In addition, $G^p(w)$ is a monotonically increasing function and $G^g(w)$ is a monotonically decreasing function of w. Hence, it can be easily shown that $|G^p(w) - G^g(w)|$ is a unimodal function of w. For this reason, the bisection method is employed to find the minimal

Algorithm 4 : Trade-off Solution for Problem $\mathbb{P}_O$

Init. $w_l = 0$, $w_u = 1$.
Solve $\mathbb{P}_R(w_l)$ to obtain $\underline{F}_1$.
Solve $\mathbb{P}_R(w_u)$ to obtain $\underline{F}_2$.
while $(w_u - w_l \geq \sigma)$ **do**
    Set $w = (w_u + w_l)/2$.
    Solve $\mathbb{P}_R(w)$ to obtain $\mathbf{x}_w$, $G^p(w)$, $G^g(w)$.
    if $(G^p(w) > G^g(w))$ **and** ($\mathbb{P}_R(w)$ is feasible) **then**
        Set $w_u = w$, $\mathbf{x}^* = \mathbf{x}_w$, $w^* = w$.
    else
        Set $w_l = w$.
Return $\mathbf{x}^*$, w^*, $G^p(w^*)$ and $G^g(w^*)$.

value of $|G^p(w) - G^g(w)|$ as shown in Algorithm 4. Note that if $w^* > \hat{w}$, where $\hat{w}$ is the value returned by Algorithm 3, then $G^p(w^*) = G^g(w^*)$, otherwise $w^* = \hat{w}$ and $G^p(w^*) > G^g(w^*)$. The reason for this is that Problem $\mathbb{P}_R(w)$ is feasible for $w \in [\hat{w}, 1]$, hence equalization of the gain losses occurs when $w^* > \hat{w}$.

4.5 Simulation results

To evaluate the performance of the proposed CEMC scheme, we have modified an industrial LV distribution grid of the Cyprus power system to consider a balanced system with 6 PV-BESS prosumers, 4 PV prosumers and 5 consumers, as shown in Figure 4.5. Towards this direction, we assume that (a) the load is uniformly distributed among the three phases, and (b) the three phases are decoupled [65]. The grid configuration and parameters have been provided by the Electricity Authority of Cyprus (Cyprus DSO). The positive-sequence impedances of the considered grid, where the line-to-line voltage is 400 volts, are given in Table 4.1. The voltage limits are set to 0.9 and 1.1 p.u ($\underline{v}_j = 0.9^2$ and $\overline{v}_j = 1.1^2$ p.u), while the substation voltage is fixed at 1 p.u (node 2 of Figure 4.5) [65].

The consumption building profiles have been synthesized considering the normalized active power consumption of three industrial buildings, as shown in Figure 4.6a. The power factor value of each building is set to 0.97. Similarly, the generation profile of the PV systems is synthesized based on two real-life normalized generation

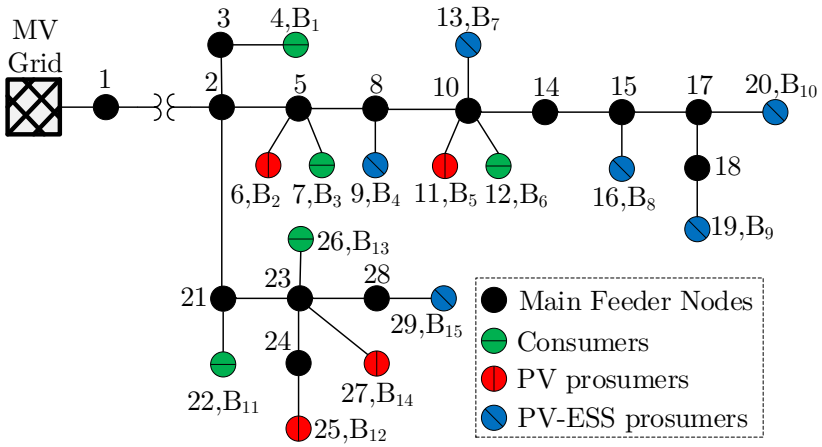

Figure 4.5: Industrial LV distribution grid.

Table 4.1: Line Impedances

Line	R (Ω)	X (Ω)	Line	R (Ω)	X (Ω)	Line	R (Ω)	X (Ω)
2-3	0.0056	0.0294	10-12	0.0439	0.0280	2-21	0.0152	0.0801
3-4	0.0080	0.0051	10-13	0.0247	0.0104	21-22	0.0060	0.0060
2-5	0.0083	0.0435	10-14	0.0220	0.0545	21-23	0.0172	0.0906
5-6	0.0445	0.0283	14-15	0.0520	0.1291	23-24	0.0273	0.0678
5-7	0.0352	0.0224	15-16	0.0861	0.0548	24-25	0.0230	0.0146
5-8	0.0237	0.0588	15-17	0.0185	0.0460	23-26	0.0354	0.0225
8-9	0.0417	0.0266	17-18	0.0106	0.0263	23-27	0.0303	0.0193
8-10	0.0244	0.0607	18-19	0.0632	0.0403	23-28	0.0593	0.1472
10-11	0.0421	0.0268	17-20	0.0621	0.0395	28-29	0.0353	0.0225

profiles, PV_1 for a sunny day and PV_2 for a partially cloudy day (Figure 4.6b). The day ahead electricity price is also presented in Figure 4.6c. Table 4.2 presents the load, PV and storage characteristics of the 15 buildings. For example, building B_4 uses load profile LP_2 with peak load demand, PV rated power, BESS capacity and BESS charging-discharging power equal to 16 kW, 16 kW, 15 kWh and 7 kW, respectively. Note that the power factor of the PV/BESS inverters is 0.9 ($\varphi_k^P = \varphi_k^B = 25.8°$), and the one-way efficiency of all BESSs is 96% ($\eta_k^c = 0.96$, $\eta_k^d = 0.96$). Thus, the losses coefficients in Eq. (4.11) are set as $e_k^c = 0.04$ and $e_k^d = 0.0416$ $\forall k \in \mathcal{B}$.

The proposed CEMC scheme is coded in Matlab, while Problem $\mathbb{P}_R$ is solved using the optimization solver Gurobi [43] on a personal computer with 8GB RAM and Intel Core-i5 3.2GHz. The horizon is set to one day with 15-minute time intervals, and the derived solution is applied in a rolling-horizon fashion. In Algorithms 3 and

Table 4.2: Buildings Data

	Load (Prof., kW)	PV (kW)	Storage (kWh, kW)		Load (Prof., kW)	PV (kW)	Storage (kWh, kW)
$\mathbf{B_1}$	LP_2, 35	0	0, 0	$\mathbf{B_9}$	LP_3, 20	20	20, 10
$\mathbf{B_2}$	LP_3, 15	15	0, 0	$\mathbf{B_{10}}$	LP_1, 22	22	25, 15
$\mathbf{B_3}$	LP_1, 17	0	0, 0	$\mathbf{B_{11}}$	LP_2, 30	0	0, 0
$\mathbf{B_4}$	LP_2, 16	16	15, 7	$\mathbf{B_{12}}$	LP_1, 21	21	0, 0
$\mathbf{B_5}$	LP_1, 20	20	0, 0	$\mathbf{B_{13}}$	LP_3, 18	0	0, 0
$\mathbf{B_6}$	LP_2, 15	0	0, 0	$\mathbf{B_{14}}$	LP_2, 20	20	0, 0
$\mathbf{B_7}$	LP_3, 18	18	20, 10	$\mathbf{B_{15}}$	LP_1, 25	25	25, 15
$\mathbf{B_8}$	LP_2, 19	19	20, 10	-	-	-	-

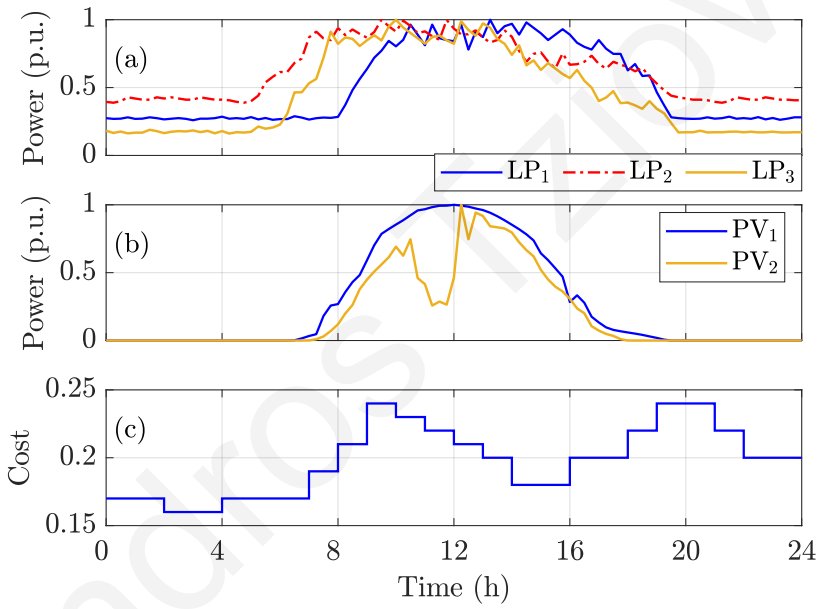

Figure 4.6: (a) Load profiles. (b) PV profiles. (c) Day-ahead electricity pricing (Euro/kWh).

4, we set $\sigma = 0.001$, resulting in a maximum of ten iterations.

The performance analysis and evaluation consider the trade-off between the objectives of the prosumers and the grid (Section 4.5.1), compare the proposed CEMC scheme with a self-consumption scheme for a single operating scenario (Section 4.5.2), and provide aggregate results on the performance of the two schemes under different normal operating conditions (Section 4.5.3). Sections 4.5.1 to 4.5.3 assume perfect knowledge of PV generation and load demand, the predicted and actual PV generation and load demand are the same, while Section 4.5.4 investigates the performance of the proposed CEMC scheme considering PV uncertainty. Interestingly, both the power flow and the BESS convex relaxations are always exact in

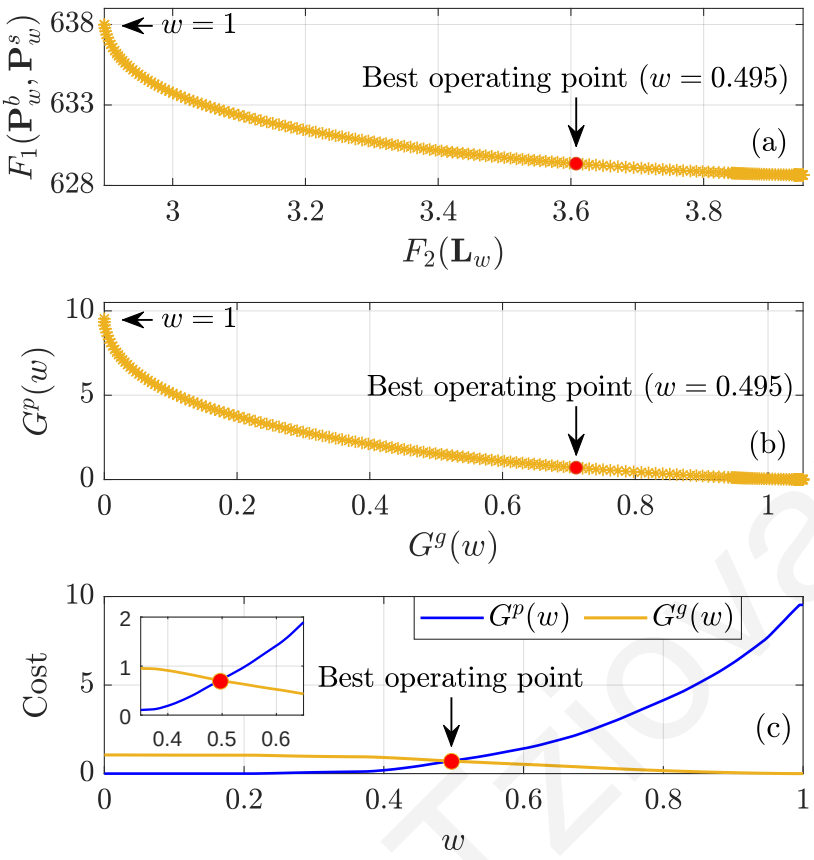

Figure 4.7: Objectives trade-off: (a) Pareto front: Prosumers daily electricity cost and grid losses cost (€), (b) Prosumers and grid gain losses (€), and (c) Prosumers and grid gain losses as a function of w.

the aforementioned case studies; hence, further experimentation is undertaken under "extreme" operating conditions to understand when the convex relaxations are violated (Section 4.5.5).

4.5.1 Objectives trade-off

The trade-off between the two objectives in (4.4) is presented in Figure 4.7(a) by solving Problem $\mathbb{P}_O(w)$ using Algorithm 3 for $w \in \{0, 0.005, 0.01, ..., 1\}$, constructing the Pareto front of the two objectives. The figure indicates the Pareto optimal points, operating points, for each value of w where it is impossible to reduce the prosumers electricity cost, $F_1(\mathbf{P}^b_w, \mathbf{P}^s_w)$, without increasing the grid losses cost, $F_2(\mathbf{L}_w)$, and vice versa. Note that the solution of Problem $\mathbb{P}_R(w)$ (Step 2 of Algorithm 3) has generated tight solutions in all cases implying optimal results for $\mathbb{P}_O(w)$. Figure 4.7(b) demonstrates the trade-off between the prosumers and grid gain losses, $G^p(w)$ and $G^g(w)$, while Figure 4.7(c) illustrates the values of the prosumers and grid gain

losses as a function of w. Interestingly, both Figures 4.7(b) and 4.7(c) indicate that the maximum $G^p(w)$, observed for $w = 1$, is several times higher than the maximum $G^g(w)$, observed for $w = 0$. Note that the minimum values of the two gain losses are observed for $w = 0$ and $w = 1$ ($G^p(0) = G^g(1) = 0$), where the corresponding objectives are given full priority. Figures 4.7(b) and 4.7(c) also show that the best operating point, obtained from Algorithm 4, is at $w^* = 0.495$, where the prosumers gain loss, $G^p(w)$, and grid gain loss, $G^g(w)$, are equal, i.e., $G^p(w) = G^g(w)$. In this sense, this point provides fairness between the prosumers and the grid operator since they suffer from the same gain losses.

The execution time needed to derive all 201 operating points and hence construct the Pareto front is 378.7 sec, resulting in an average time of 1.88 sec to solve Problem $\mathbb{P}_R(w)$ for a single point. Nonetheless, in each MPC control-step of the CEMC scheme the GC does not need to construct the Pareto front; it only needs to find the best operating point according to Algorithm 4. The execution time of Algorithm 4 is 16.4 sec on average which is very small compared to the 15-minute control-step of the MPC.

4.5.2 Performance evaluation

The performance of the proposed CEMC scheme is evaluated and compared with a self-consumption (SC) scheme in a single operating scenario using PV_2 when w is undefined. In the SC scheme, each PV-BESS prosumer operates in self-consumption mode, in which the BESS is charged when the building net load[2] is negative, and discharged otherwise; reactive power support is not provided.

The response of the grid operation based on the SC scheme and the proposed CEMC scheme are presented in Figures 4.8 and 4.9, respectively. Figures 4.8(a) and 4.9(a) depict the buildings-grid active power exchange for the 6 PV-BESS prosumers. As can be seen, the CEMC scheme maximizes the prosumers profits by (i) absorbing power to charge the BESSs when electricity prices are low (periods $2-4$ am and $2-4$ pm), and (ii) injecting power to the grid by discharging the BESSs when electricity prices are high (periods $9-10$ am and $7-9$ pm). The reactive power exchange for the 6 PV-BESS prosumers is shown in Figures 4.8(b) and 4.9(b). In the SC scheme, the prosumers import reactive power to satisfy their load demand, while in the CEMC

[2]The net load is defined as the difference between the load demand and the PV generation.

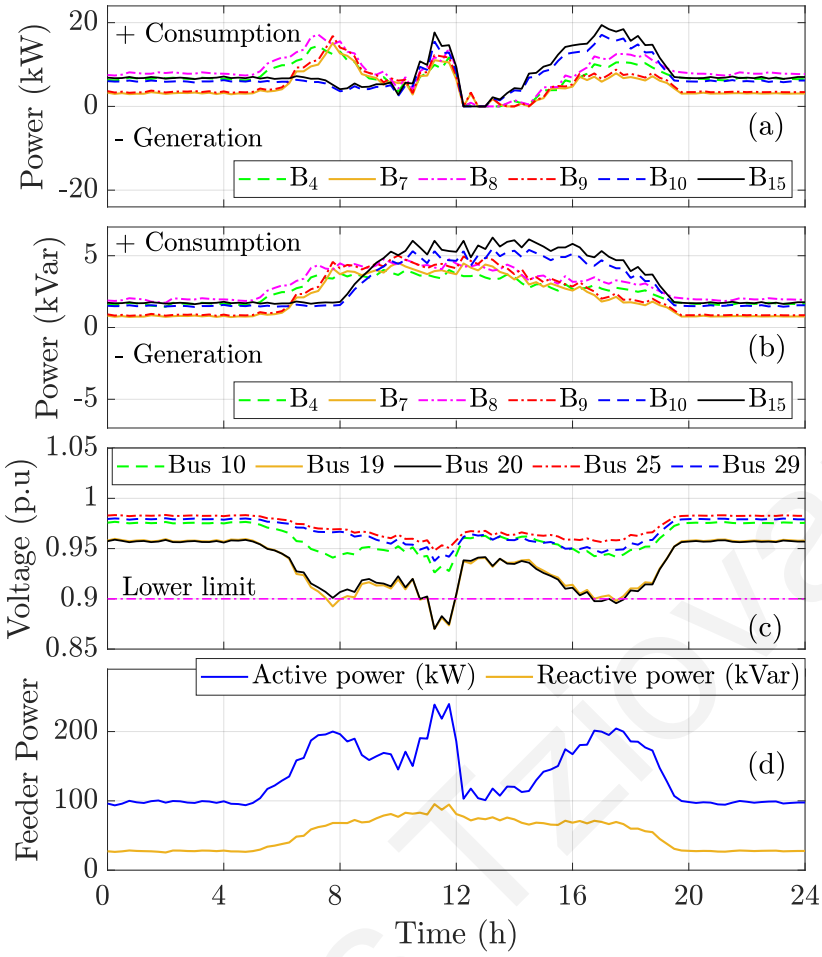

Figure 4.8: Grid operation using the self-consumption (SC) scheme: (a) Active power exchange, (b) Reactive power exchange of the PV-BESS prosumers, (c) Voltages at five critical grid buses, (d) Feeder imported power.

scheme they export reactive power to the grid through the PV-BESS inverters to provide reactive power support. Figures 4.8(c) and 4.9(c) present the voltages of five critical nodes of the grid. As can be seen, the SC scheme experiences multiple voltage violations at buses 19 and 20, dropping below the safety limit of 0.9 p.u. In contrast, the CEMC scheme maintains the voltages close to their nominal values (1 p.u.) at all buses. Figures 4.8(d) and 4.9(d) demonstrate the imported active and reactive power from the LV feeder. As expected from the reactive power support, the CEMC scheme dramatically reduces the reactive power compared to the SC scheme. Specifically, the CEMC scheme achieves 67% peak reduction and 79.3% total energy reduction. The peak active power is also reduced by 8.22%.

Table 4.3 presents the daily electricity cost of the six PV-BESS prosumers using the two schemes. The proposed CEMC scheme reduces the total daily electricity cost of the prosumers from €192.1 to €180.1 (6.2% reduction), the total grid losses

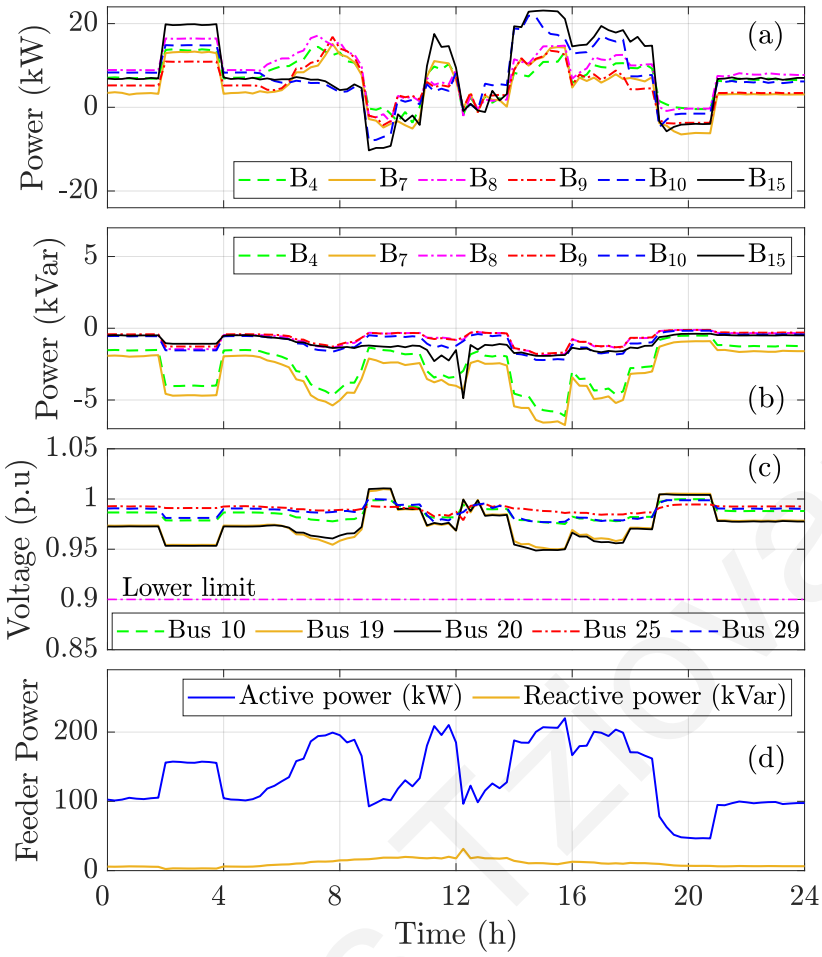

Figure 4.9: Grid operation using the proposed CEMC scheme: (a) Active power exchange, (b) Reactive power exchange of the PV-BESS prosumers, (c) Voltages at five critical grid buses, (d) Feeder imported power.

Table 4.3: Prosumers Daily Electricity Cost (€)

Buildings	$\mathbf{B_4}$	$\mathbf{B_7}$	$\mathbf{B_8}$	$\mathbf{B_9}$	$\mathbf{B_{10}}$	$\mathbf{B_{15}}$
SC scheme	32.87	23.03	39.03	25.59	33.51	38.08
CEMC scheme	31.39	21.01	37.13	23.75	31.30	35.49
Cost reduction	4.5%	8.8%	4.9%	7.2%	6.6%	6.8%

from 19.64 kWh to 19.03 kWh (3.1% reduction), and the grid losses cost from €3.98 to €3.61 (9.3% reduction), on average.

4.5.3 Aggregate performance evaluation

The performance of the proposed CEMC scheme is evaluated and compared with the SC scheme under different normal operating conditions when w is undefined.

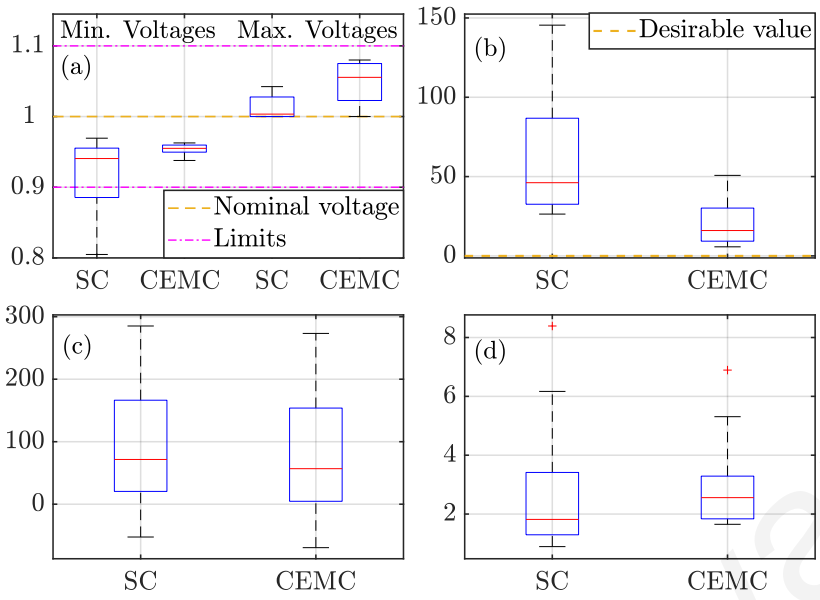

Figure 4.10: Aggregate results of the SC and CEMC schemes: (a) Minimum and maximum bus voltages in p.u, (b) Maximum imported reactive power of the feeder in kVar, (c) Total daily cost of the PV-BESS prosumers in €, (d) Cost of the grid losses in €.

Twelve scenarios are carried out that involve combinations between (i) low, medium and high loads, (ii) sunny and cloudy days, and (iii) working and non-working days. The load values of Table 4.2 are considered to represent medium loads. The low (resp. high) loads are obtained by decreasing (resp. increasing) the medium loads by 30%. The load profiles of the working days are indicated in Figure 4.6; the base load of these profiles is considered as the load demand of the non-working days.

The results using the two schemes are demonstrated in Figure 4.10, in box-plot form[3]. Figure 4.10(a) shows the minimum and maximum bus voltages of the considered LV distribution grid. A 11.1% minimum voltage violation can be observed for the SC scheme; no violations are observed for the CEMC scheme. Figure 4.10(b) illustrates that the CEMC scheme achieves considerable reduction of the maximum imported reactive power of the feeder. Specifically, the feeder maximum and median reactive power values are reduced by 65.1% and 65.5%, respectively.

[3]The bottom and top of each box indicate the first and third quartiles (25% and 75%) of a ranked data set, while the horizontal line inside the box indicates the median value (second quartile). The horizontal lines outside the box indicate the lowest/highest datum still within 1.5 inter-quartile range of the lower/upper quartile; for normally distributed data this corresponds to approximately 0.35%/99.65%.

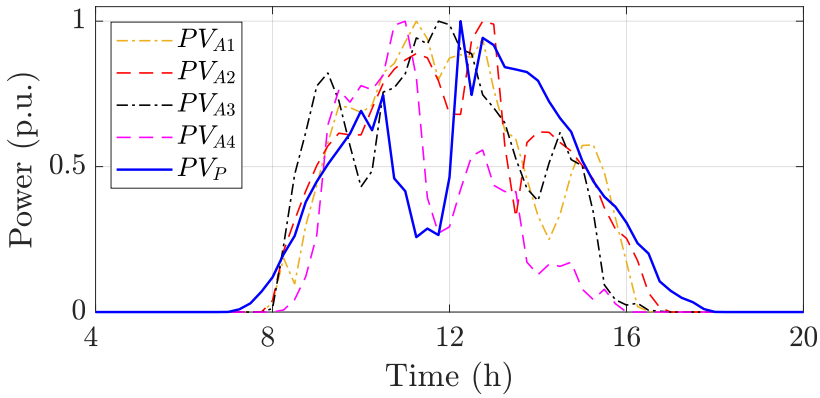

Figure 4.11: PV curves used for performance evaluation under PV uncertainty. PV_{A1}, PV_{A2}, PV_{A3} and PV_{A4} are the actual PV curves in four different cases, while PV_P is the predicted PV curve in all cases.

Figures 4.10(c) and 4.10(d) present the total electricity cost of the PV-BESS prosumers and the grid losses cost, respectively. As can be observed, the CEMC scheme achieves a 20.6% reduction of the median electricity cost compared to the SC scheme (€56.83 compared to €71.58), in exchange for a small increase in the grid losses cost (€2.55 compared to €1.81). This is because the SC scheme reduces the grid-buildings power exchange leading to low grid losses.

4.5.4 Performance evaluation considering PV uncertainty

This section investigates the performance of the proposed CEMC scheme considering PV uncertainty for the scenario of Section 4.5.2. Figure 4.11 depicts the predicted and actual PV generation for four different cases. PV_{A1} - PV_{A4} are real-life, normalized, partially-clouded, PV generation curves that are used as the actual, but unknown, PV generation profile of each considered case. Moreover, PV_P indicates the predicted PV generation (same with PV_2 in Figure 4.6), used in all cases. Under the proposed control architecture, we examine the effectiveness of three CEMC variations:

- **CEMC**^{NU}: considers PV_P with no updates.
- **CEMC**^{U}: updates the PV_P curve for the examined MPC control-step t such that:
  $PV_P(t+1) \leftarrow 0.5(PV_A(t) + PV_P(t+1))$.
- **CEMC**^{p}: assumes perfect information such that:
  $PV_P(t) \leftarrow PV_A(t),\ \forall t$.

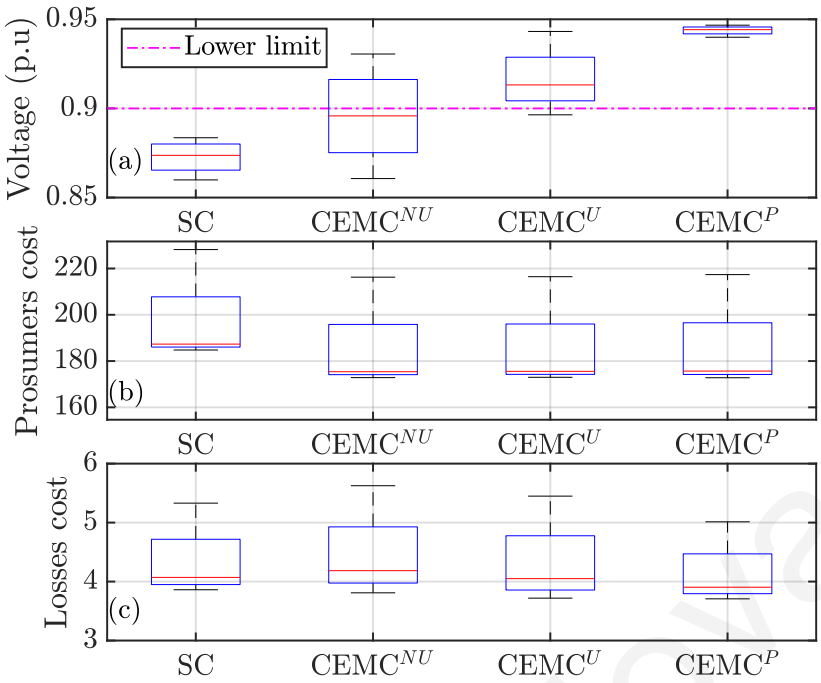

Figure 4.12: Aggregate results of the SC, CEMC^{NU}, CEMC^{U} and CEMC^{P} schemes considering PV uncertainty: (a) Minimum voltage in p.u, (b) Total daily cost of the PV-ESS prosumers in €, (c) Cost of the grid losses in €.

The three schemes are compared against the SC scheme. Note that although the CEMC^{P} scheme is unrealizable as it assumes knowledge of future information, it is used for comparison purposes as it provides the optimal performance.

Figure 4.12(a) depicts the minimum voltages of the SC, CEMC^{NU}, CEMC^{U} and CEMC^{P} schemes in box-plot form for the four PV generation cases. Interestingly, voltage violations of the lower limit are presented in the SC scheme for all cases, while the CEMC^{NU} scheme generates significantly better results even with the large error between the predicted and actual PV generation. However, the CEMC^{U} scheme increases the minimum voltages, eliminating almost all violations, because the updating of the predicted PV generation in each MPC control-step corrects the reactive power support. As expected, the best results are provided under perfect knowledge of the PV generation (CEMC^{P}), avoiding all voltage violations. As depicted in Figure 4.12(b), the CEMC^{NU}, CEMC^{U} and CEMC^{P} schemes reduce the total daily cost of the PV-BESS prosumers compared to the SC scheme, while the three CEMC schemes result to similar costs. As shown in Figure 4.12(c), the CEMC^{NU} yields slightly higher grid losses costs compared to the SC scheme; however, the grid losses costs are reduced in the CEMC^{U} and CEMC^{P} schemes, where the latter generates the lowest grid losses costs. It is interesting to observe that the CEMC^{U} scheme handles well the PV

generation uncertainty by avoiding almost all violations, despite using a very simple approach to update the predicted PV generation. Utilizing more sophisticated prediction schemes can yield even better performance.

4.5.5 Exactness of convex relaxations

An interesting observation that has emerged from the simulation results of Sections 4.5.1 to 4.5.4 is that the considered relaxations are always exact. Hence, in this section further experimentation is conducted to investigate the exactness of both the power flow and the BESS relaxations under the following "extreme" operating scenario: (i) PV generation: PV_1; (ii) Load demand: medium non-working day reduced by 80%; (iii) reduced upper limits of the voltages (1.1 − 1.01 p.u.); and (iv) no reactive power support ($Q^P_{t,k} = Q^B_{t,k} = 0,\ \forall t,k$). These scenario characteristics aim to increase the reverse power flow through the grid, cause the binding of the upper-bound voltage constraints, and apply PV curtailments, rather than reactive power support, for voltage control, in an effort to produce loose relaxation solutions. Perfect knowledge of PV generation and load demand is considered.

Exactness of the power flow relaxation

Table 4.4 presents (i) the operating point $\hat{w}$, (ii) the operating point w^*, (iii) the prosumers and grid gain losses, and (iv) the applied PV power curtailments, for different upper limit values of the voltage ($\overline{V} = \sqrt{\overline{v}_j}, \forall j \in \mathcal{N}$). As explained in Section 4.4.3, the gain loss equalization, $G^p(w^*) = G^g(w^*)$, is attained when $w^* > \hat{w}$, which holds for $\overline{V} \geq 1.07$ p.u in this case. Note also that $G^p(w^*) > G^g(w^*)$, when $w^* = \hat{w}$, which is the case for $\overline{V} \leq 1.05$ p.u. Interestingly, the difference between $G^p(w^*)$ and $G^g(w^*)$ increases considerably as $\overline{V}$ drops below 1.05 p.u., due to the BESS set-points and the PV curtailments that are applied to maintain the voltages within bounds. Algorithm 4 ensures the exactness of the power flow relaxation.

The solution quality of $\mathbb{P}_O(w)$, obtained from Algorithm 3, is examined with respect to the lower bounds obtained from the solution of the relaxed problem $\mathbb{P}_R(w)$ for varying w. Figure 4.13 displays the prosumers electricity cost, $F_1(\mathbf{P}^b_w, \mathbf{P}^s_w)$, the grid losses cost, $F_2(\mathbf{L}_w)$, and the objective value, Eq. (4.4), derived from the solution of $\mathbb{P}_O(w)$ and $\mathbb{P}_R(w)$ when $\overline{V} = 1.03$. The graphs can be "separated" in two different regions. For $w \geq 0.84$, an exact relaxation is obtained from the solution

Table 4.4: "Extreme" Operating Conditions - Results

$\overline{V}$ (p.u)	$\hat{w}$	w*	G^p(w*)	G^g(w*)	PV curtailments
1.1	0.01	0.60	€2.77	€2.77	0 kWh
1.07	0.35	0.60	€2.77	€2.77	0 kWh
1.05	0.55	0.55	€3.92	€2.60	0 kWh
1.03	0.84	0.84	€30.3	€1.39	88.2 kWh
1.01	0.91	0.91	€89.1	€0.53	350 kWh

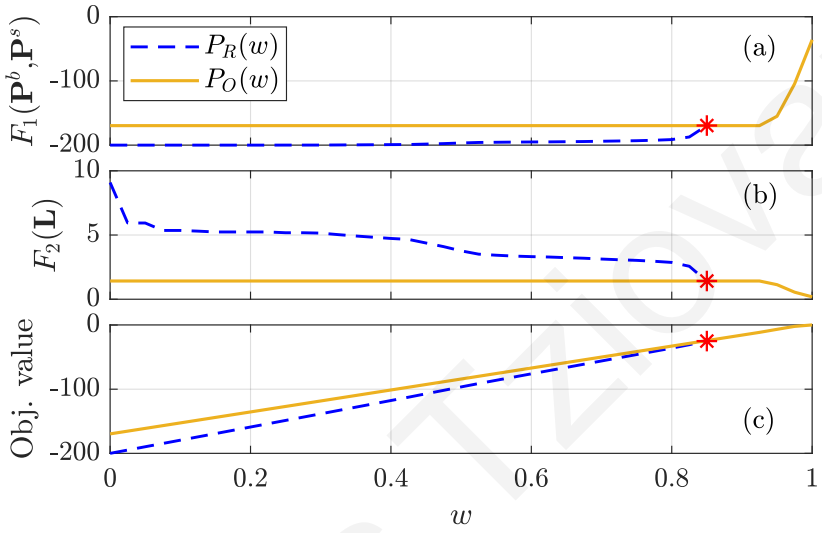

Figure 4.13: Results for $\overline{V} = 1.03$: (a) prosumers electricity cost (€), (b) grid losses cost (€) and (c) objective function value.

of $\mathbb{P}_R(w)$ which is also optimal for $\mathbb{P}_O(w)$. As the solution of $\mathbb{P}_R(w)$ yields a non-exact relaxation for $w < 0.84$, Algorithm 3 is employed to obtain a feasible solution to $\mathbb{P}_O(w)$. To examine the quality of the solution to $\mathbb{P}_O(w)$, the optimality gap is considered

$$\text{Optimality Gap} = \frac{F_{\mathbb{P}_O}(w) - F_{\mathbb{P}_R}(w)}{F_{\mathbb{P}_R}(w)} \times 100\%, \tag{4.22}$$

where $F_{\mathbb{P}_O}(w)$ and $F_{\mathbb{P}_R}(w)$ denote the objectives values derived from the solution of Problems $\mathbb{P}_O(w)$ and $\mathbb{P}_R(w)$. Interestingly, the maximum optimality gap is only 15.1% for $w = 0$ and is reduced as w increases. The reason is that increasing w makes the second objective of minimizing the grid losses cost more important, which causes the reduction of the power flows in the grid. This is achieved by utilizing the BESSs and applying PV power curtailments, also contributing to the reduction of the voltage limits violation. The effect of these actions becomes more important as w increases, causing the gradual reduction of the optimality gap and eventually leading to the exactness of the power flow relaxation.

Exactness of the BESS relaxation

The exactness of the relaxed version of the proposed BESS model, constraints (4.18a) - (4.19), is examined and compared with two BESS models employed in [33, 34, 40], presented in the Appendix. The first is the *exact non-convex BESS model* and the second is the relaxed version of the first model, the *relaxed convex BESS model*. To investigate the performance of these two BESS models in the CEMC scheme, we define the following problems:

- **Problem** $\mathbb{P}_E(w)$ is obtained by replacing the proposed BESS model, constraints (4.18a) - (4.19), with the *exact non-convex BESS model*, Eqs. (A.1) - (A.4), in Problem $\mathbb{P}_R(w)$. Problem $\mathbb{P}_E(w)$ is a non-convex SOCP with complementarity constraints.

- **Problem** $\mathbb{P}_C(w)$ is obtained by replacing the proposed BESS model, constraints (4.18a) - (4.19), with the *relaxed convex BESS model*, Eqs. (A.1) - (A.3), in Problem $\mathbb{P}_R(w)$. Problem $\mathbb{P}_C(w)$ is a convex SOCP.

Solutions to the two literature based BESS models are obtained by replacing Problem $\mathbb{P}_R(w)$ with $\mathbb{P}_E(w)$ and $\mathbb{P}_C(w)$ in Algorithm 4, respectively. The complementarity constraints (A.4) in Problem $\mathbb{P}_E(w)$ are handled by the optimization solver as SOS-1 constraints, where at most one variable in the specified list is allowed to take a non-zero value, indicated as SOS-1$(P^d_{t,k}, P^c_{t,k})$, $\quad \forall t, k \in \mathcal{B}$, [43].

Figure 4.14(a) presents the total BESS energy losses[4] in kWh obtained by solving Problems $\mathbb{P}_R(w)$, $\mathbb{P}_E(w)$ and $\mathbb{P}_C(w)$, employing Algorithm 4, for different values of the voltage upper limit ($\overline{V}$). The results indicate that the two relaxed BESS models, associated with Problems $\mathbb{P}_R(w)$ and $\mathbb{P}_C(w)$, are exact for $\overline{V} \geq 1.05$ yielding the same losses with Problem $\mathbb{P}_E(w)$, while are non-exact for $\overline{V} \leq 1.04$. Interestingly, the proposed relaxed BESS model generates lower losses for $\overline{V} \leq 1.04$ compared to the relaxed literature-based BESS model. As can be seen in Figure 4.14(b), the non-exactness of the BESS relaxations occurs only when PV power curtailments are applied. Note that power curtailments are presented for $\overline{V} \leq 1.04$ to satisfy the voltage upper limits. Consequently, extra BESS energy losses are introduced as an alternative power curtailment form by violating the BESS relaxation exactness.

[4]The total BESS energy losses for Problems $\mathbb{P}_E(w)$ and $\mathbb{P}_C(w)$ are defined in the Appendix. For Problem $\mathbb{P}_R(w)$, the total BESS energy losses are calculated as $\sum_{t\in\mathcal{T}} \sum_{k\in\mathcal{B}} (P^{loss}_{t,k})\Delta T$.

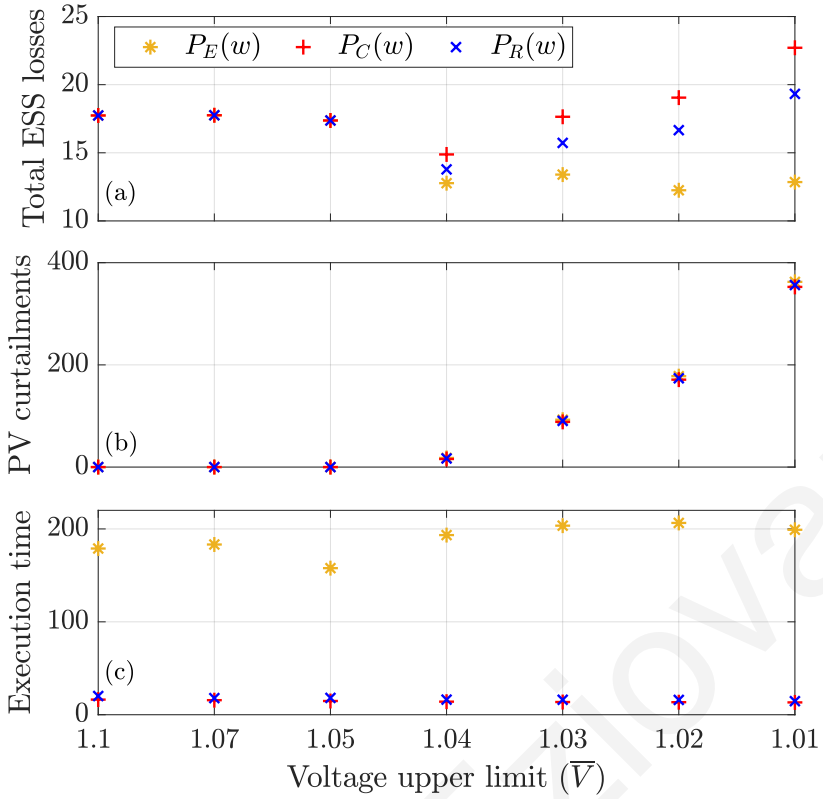

Figure 4.14: Results for different BESS models: (a) total BESS energy losses (kWh), (b) PV curtailments (kWh) and (c) execution time of Algorithm 4 (sec).

Figure 4.14(c) demonstrates the execution time of Algorithm 4 in sec for Problems $\mathbb{P}_R(w)$, $\mathbb{P}_E(w)$ and $\mathbb{P}_C(w)$. As expected, the execution time of the non-convex SOCP problem (Problem $\mathbb{P}_E(w)$) is considerably higher (10-16 times higher) compared to the times of the convex SOCP problems ($\mathbb{P}_R(w)$ and $\mathbb{P}_C(w)$), which have similar execution times.

4.6 Conclusions

This chapter proposes an energy management and control scheme for managing the operation of an active distribution grid with prosumers. A non-convex multi-objective optimization model to minimize (i) the prosumers electricity cost and (ii) the grid energy losses cost, while maintaining the safe and reliable operation of the grid is formulated. The derived optimization problem is relaxed to a convex SOCP model and an algorithm to ensure feasibility under any operating condition is developed. Simulation results suggest that the relaxed optimization problem yields optimal solutions under normal operating conditions, while the associated algorithm

yields close-to-optimal results under "extreme" operating conditions, for which the relaxations are not exact. Moreover, a novel algorithm to find an operating point that provides fairness between the prosumers and the grid costs is proposed. Simulation results indicate the effectiveness and superiority of the proposed scheme in comparison with a self-consumption approach, even under PV generation uncertainty. Future work will explore energy management and control schemes for unbalanced distribution grids.

Chapter 5

Energy management of a flywheel storage system for peak shaving applications

Peak shaving applications provided by energy storage systems enhance the utilization of existing grid infrastructure to accommodate the increased penetration of renewable energy sources. This chapter investigates the provision of peak shaving services from a flywheel energy storage system installed in a transformer substation. A lexicographic optimization scheme is formulated to define the flywheel power set-points by minimizing the transformer power limit violations and the flywheel energy losses. Convex functions that represent the flywheel power losses and its maximum power are derived and integrated in the proposed scheme. A two-level hierarchical control framework is introduced to operate the transformer-flywheel-system in a way that handles prediction errors and modelling inaccuracies. At the higher level, a model predictive controller is developed that solves the lexicographic optimization scheme using linear programming. At the lower-level, a secondary controller corrects the power set-points of the model predictive controller using real-time measurements. A software platform has been developed for integrating the proposed controllers in an experimental setup to test their effectiveness in a realistic testbed setting, and the flywheel system characteristics are experimentally identified. Simulation and experimental results validate and verify the modelling, identification, control and operation of a real flywheel system for peak shaving services.

5.1 Introduction

The increasing penetration of PV generation into the distribution grid along with the load demand growth can cause reverse and direct power flow violations in distribution transformers. As a result, the distribution grids can operate outside of their safely limits, particularly in cases with extensive integration of PVs and electric vehicle charging stations. Nevertheless, the safe and reliable operation of distribution grids can be maintained by ESSs that provide peak shaving services [67]. ESSs enhance the capacity of existing distribution grids to accommodate the load and PV generation growth in order to avoid any violations of the maximum power limit of the distribution transformers [68]. Towards this direction, this chapter develops an energy management and control scheme for a FESS to provide peak shaving services to the distribution grid. Among the different types of ESSs, FESSs are suitable for applications that require short-time power quality services and peak-load regulation, since they are characterized by full depth discharge capability, 85-90% efficiency rate, very long lifetime, environmental friendliness, lower maintenance cost and high charging-discharging abilities compared to BESSs [69,70].

Peak shaving applications are investigated in [71,72] for planning purposes, to examine the location, sizing and cost-benefit of the ESSs. In addition, peak shaving services provided to distribution grids using BESSs are proposed in [73–77] for operational purposes using optimization methods. These services are provided by minimizing the daily peak power [73–76] or the square of the power drawn from the feeder [77]. Also, in [75,76] predicted load uncertainties are addressed using stochastic formulations. Note that weighted multi-objective functions are used in [75–77] where a first objective is associated with peak shaving and a second objective with the health and longevity of a BESS. In these formulations, an improvement in the first objective can deteriorate the second objective; however, the optimal trade-off between the conflicting objectives has not been considered. The BESS health objective can be ignored when using a FESS, because FESSs have very high number of cycles and high charging/discharging rate.

A peak shaving application using a FESS is presented in [78] to reduce the maximum power demand of shore-to-ship cranes. Power smoothing applications in wind power plants using FESSs are presented in [79–81]. These are short-time applications that smooth the power injected to the grid and compensate power disturbances. Note

that FESSs are not suitable for long term energy storage because they suffer from high standby losses, as the self-discharge can reach 20% per hour [69]. However, hybrid wind-FESS energy management schemes are presented in [82, 83] to compensate the main drawback of the FESSs by formulating optimization schemes that minimize the FESS standby losses. Specifically, a model predictive controller and a secondary real-time controller are used in [83], to shift the surplus wind energy and to compensate the wind-power prediction error. The aforementioned works control a FESS using models that are dependent on technical characteristics such as the angular speed and the stator current and voltage. Nevertheless, these characteristics are not always available through commercial FESS interfaces. The available measurements in commercial interfaces are the State-of-Charge (SoC) and the instant charging/discharging rate, while users can command the FESS to maintain a constant charging/discharging power or SoC. In addition, the associated FESS models can lead to non-convex optimization problems which are challenging to solve [82].

This chapter aims to eliminate the power violations of a distribution transformer using a FESS and minimize the FESS power losses for a cost-effective operation of the distribution grid. A novel lexicographic optimization scheme is formulated that derives the FESS power set-points to minimize the transformer power limit violations and the FESS energy losses. Functions that represent the power losses and maximum power of a FESS are derived and integrated in the proposed scheme. In detail, two linear functions that model the FESS power losses based on the charging mode are derived as a function of the charging/discharging power and the SoC. Also, a nonlinear function is derived to associate the FESS maximum charging/discharging power with the SoC due to the rated current limit imposed by the power electronics converter.

A two-level hierarchical control scheme is proposed that minimizes the objectives of the lexicographic optimization problem and deals with demand prediction errors and modelling uncertainties. At the higher-level, a model predictive controller is developed that handles the considered problem by sequentially solving four linear optimization problems. At the lower-level, a secondary controller corrects the control signals using real-time measurements at a shorter time-scale.

The proposed hierarchical control scheme is integrated and validated in an experimental setup. Towards this direction, a software platform based on FIWARE [84] has been developed that enables the monitoring and control of a flywheel system

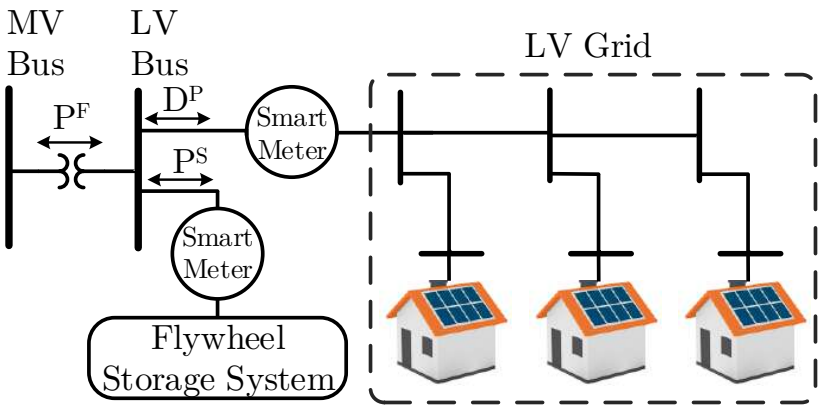

Figure 5.1: Peak shaving services to a LV distribution grid.

in a smart grid environment. Model validation and parameter identification is experimentally performed for the prototype FESS, indicating the high accuracy of the derived functions to estimate the FESS power losses and maximum power. In addition, simulation and experimental results validate the effectiveness of the proposed energy management and control scheme to provide peak shaving services, enabling the active management of smart distribution grids.

The remainder of this chapter is organized as follows. Section 5.2 states the problem and Section 5.3 models the maximum power and power losses of a FESS. The two-level hierarchical solution methodology is then described in Section 5.4. The proposed solution methodology is evaluated both in simulation and experimentally in Sections 5.5 and 5.6, respectively. The practical implementation considerations are stated in Section 5.7. Finally, Section 5.8 concludes the paper.

5.2 Problem statement

This chapter considers the provision of peak shaving services to an MV/LV transformer substation. At the LV side, the substation bus with an installed FESS is connected to an LV distribution grid with consumer and PV installations, as illustrated in Figure 5.1. Peak shaving is achieved by managing the FESS power set-points to minimize in a lexicographic fashion: (i) the transformer peak power violation, (ii) the transformer energy violation, (iii) the SoC energy violations to sustain a minimum desirable SoC in the FESS and (iv) the FESS power losses. The considered problem,

denoted by $\mathbb{P}_{LEX}$, is given by

$$\text{lexmin}\left\{f_V(\mathbf{x}),\ f_E(\mathbf{x}),\ f_U(\mathbf{w}),\ f_L(\mathbf{P}^L)\right\} \quad (\mathbb{P}_{LEX}) \tag{5.1a}$$

$$\text{s.t. } \underline{P}^F - x_t \leq P_t^F \leq \overline{P}^F + x_t, \qquad \forall t \in \mathcal{T}, \tag{5.1b}$$

$$C_t^S + w_t \geq \underline{C}_t^d, \qquad \forall t \in \mathcal{T}, \tag{5.1c}$$

$$P_t^F + P_t^S = D_t^A, \qquad \forall t \in \mathcal{T}, \tag{5.1d}$$

$$C_{t+1}^S = C_t^S + \Delta T(-P_t^S - P_t^L), \qquad \forall t \in \mathcal{T}, \tag{5.1e}$$

$$C_0^S = I^c,\ 0 \leq C_t^S \leq \overline{C}^S, \qquad \forall t \in \mathcal{T}, \tag{5.1f}$$

$$\underline{P}^S \leq P_t^S \leq \overline{P}^S, \qquad \forall t \in \mathcal{T}, \tag{5.1g}$$

$$|P_t^S| \leq g(C_t^S), \qquad \forall t \in \mathcal{T}, \tag{5.1h}$$

$$P_t^L \geq h(C_t^S, P_t^S), \qquad \forall t \in \mathcal{T}, \tag{5.1i}$$

where $\mathcal{T} = \{1, ..., T/\Delta T\}$, T is the time-horizon and ΔT is the time-step duration considered.

In problem $\mathbb{P}_{LEX}$, variable P_t^F denote the transformer power, P_t^S the FESS charging (negative values) and discharging power (positive values), P_t^L the FESS power losses, x_t the transformer maximum power violation, while C_t^S and w_t denote the SoC and the SoC energy violation of the FESS at time t, respectively. $\mathbf{P}^L$, $\mathbf{x}$ and $\mathbf{w}$ are vector forms of P_t^L, x_t and w_t, $\forall t \in \mathcal{T}$, respectively; for example, $\mathbf{x} = [x_1, ..., x_t, ..., x_T]$. Parameters $\underline{P}^F$ [$\overline{P}^F$] and $\underline{P}^S$ [$\overline{P}^S$] denote the minimum [maximum] transformer and FESS power, respectively, $\overline{C}^S$ the maximum SoC, while I^c denotes the initial FESS state. Parameter D_t^A is the actual net load demand of the LV grid defined as

$$D_t^A = D_t^P + \xi_t, \quad \forall t \in \mathcal{T}, \tag{5.2}$$

where D_t^P is the predicted net load of the LV grid and ξ_t is the prediction error at time-step t. D_t^A is generally unknown; hence, the predicted load is used in practical applications.

The first objective of $\mathbb{P}_{LEX}$ is to minimize a function $f_V(\mathbf{x})$ of transformer maximum power violations, while the second objective, $f_E(\mathbf{x})$, is to minimize the transformer energy violations. To achieve this, soft constraint (5.1b) is introduced to restrain the transformer power within its limit; variables x_t obtain non-zero values when transformer power limit violations are unavoidable. The third objective is to minimize the SoC energy violations, $f_U(\mathbf{w})$, to sustain a minimum desirable SoC in the FESS, $\underline{C}_t^d$, according to soft constraint (5.1c). This minimum SoC of the FESS is used in

Section 5.4 to address the transformer power limit violations that are caused by the load demand uncertainty. The fourth objective is to minimize the FESS power losses $f_L(\mathbf{P}^L)$. Note that low priority objectives are optimized as far as they do not affect the optimal solution of higher priority objectives. In Section 5.4, the four objectives are mathematically defined and the reasons for the selected lexicographic order are explained.

In addition to constraints (5.1b) and (5.1c) which relate to the objectives of $\mathbb{P}_{LEX}$, the problem includes six more constraints. The power balance equation (5.1d) aims to select the FESS charging/discharging power to compensate for load demand exceeding the transformer maximum power to avoid transformer power limit violations. The FESS SoC dynamic state equations are defined in (5.1e) - (5.1f) and the charging/discharging power limits in (5.1g). Eq. (5.1e) takes into consideration the FESS power losses defined in (5.1i). Finally, Eq. (5.1h) restricts the maximum charging/discharging power as a function of the SoC.

Problem $\mathbb{P}_{LEX}$ is convex when functions $f_V(\mathbf{x})$, $f_E(\mathbf{x})$, $f_U(\mathbf{w})$, $f_L(\mathbf{P}^L)$ and $h(C_t^S, P_t^S)$ are convex and function $g(C_t^S)$ is concave. Section 5.3 details the modelling and derivation of standard-form convex expressions of the FESS functions $g(C_t^S)$ and $h(C_t^S, P_t^S)$ that appear in Eqs. (5.1h) and (5.1i), respectively. Then, Section 5.4 proposes a two-level hierarchical control scheme to handle Problem $\mathbb{P}_{LEX}$ under demand uncertainty.

5.3 FESS modelling

5.3.1 FESS power losses

A FESS is a kinetic energy storage technology composed of mechanical components, an electrical machine and a power converter. The stored energy in kinetic form is given by

$$C^S(t) = 0.5 J \omega_r^2(t), \quad \forall t \in \mathcal{T}, \quad \Rightarrow \quad C^S \sim \omega_r^2, \tag{5.3}$$

where J is the moment of inertia and ω_r is the angular speed [69]. Notice that the stored energy is analogous to ω_r^2. Power losses occur at all components depending on the operational condition of a FESS. Specifically, windage and bearing friction losses occur in the mechanical components; hysteresis losses, eddy currents and

copper losses occur in the electrical machine; conduction and switching losses occur in the power electronics converter [85]. The windage and eddy currents losses are proportional to ω_r^2; while bearing and hysteresis losses are proportional to ω_r [85]. Therefore, the power losses in a FESS are usually described by polynomial functions of ω_r, such as $c_1\omega_r^2$ [86], and $c_1\omega_r^2 + c_2\omega_r$ [82, 83, 85], where c_1 and c_2 are constants. A more accurate representation considers different FESS power losses functions for the charging and discharging modes [87].

In this chapter, two linear functions are proposed to represent the FESS power losses based on the charging mode. The power losses of each mode are described by a linear function of the charging/discharging power and the SoC as shown in Table 5.1. In Eqs. (5.4b) and (5.4c), P_t^d and P_t^c denote the power losses of the discharging and charging mode, respectively, while $\hat{b}^c$, $\hat{b}^d$, $\hat{c}^c$ and $\hat{c}^d$ are positive constants depended on the FESS structure and characteristics. In the proposed representation, term C^S corresponds to ω_r^2 according to (5.3); thus, the terms $\hat{c}^d C_t^S$ and $\hat{c}^c C_t^S$ represent the polynomial term $c_1\omega_r^2$. Note that $c_1\omega_r^2$ is the dominant power losses term of the polynomial function $c_1\omega_r^2 + c_2\omega_r$, especially at high speeds and with reduced bearing friction losses (since low-friction magnetic bearings are typically used in flywheel applications) [85, 88, 89]. In addition, the terms $\hat{b}^d P_t^S$ and $\hat{b}^d P_t^S$ consider the FESS power losses for the charging and discharging modes. Logical constraints in (5.4a) and (5.4d) are introduced to select the appropriate function based on the charging mode. The power losses parameters in Eqs. (5.4b) - (5.4c) can be experimentally estimated for any real FESS system using the proposed methodology presented in Section 5.6.2. Moreover, when the round-trip efficiency, e^r, and the standby losses per hour, l^s, of a commercial FESS are given by the manufacturer datasheet, e.g, $e^r = 85\%$ and $l^s = 20\%$ [69], then the FESS power losses can be represented using Eqs. (5.4b) - (5.4c) by setting $\hat{b}^c$=$\hat{b}^d$=$(100\% - e^r)/2$ and $\hat{c}^c$=$\hat{c}^d$=l^s.

Incorporating Eqs. (5.4a) - (5.4d) into Problem $\mathbb{P}_{LEX}$ leads to non-convex optimization formulations due to the presence of binary variables. To avoid this issue, notice that when $P_t^S \geq 0$ it is true that $P_t^d \geq P_t^c$ since $\hat{b}^c$, $\hat{b}^d$, $\hat{c}^c$, $\hat{c}^d$ and C_t^S are positive; conversely, when $P_t^S \leq 0$ it is true that $P_t^c \geq P_t^d$. These imply that $h(C_t^S, P_t^S) = \max\{P_t^d, P_t^c\}$. Hence, constraint (5.1i) is convex and can be equivalently represented by affine constraints (5.5a) and (5.5b). Constraints (5.5a) and (5.5b) are binding when $P_t^S \geq 0$ and $P_t^S \leq 0$, respectively.

The derived functions of the FESS power losses enable:

Table 5.1: FESS power losses and FESS maximum power limit

Derived Constraints		Convex Affine Constraints	
$P_t^L = \delta P_t^d + (1-\delta_t)P_t^c$	(5.4a)	$P_t^L \geq \hat{b}^d P_t^S + \hat{c}^d C_t^S, \quad \forall t \in \mathcal{T}$	(5.5a)
$P_t^d = \hat{b}^d P_t^S + \hat{c}^d C_t^S$	(5.4b)	$P_t^L \geq -\hat{b}^c P_t^S + \hat{c}^c C_t^S, \quad \forall t \in \mathcal{T}$	(5.5b)
$P_t^c = -\hat{b}^c P_t^S + \hat{c}^c C_t^S$	(5.4c)	$P_t^S \leq \alpha_i + \beta_i C_t^S, \quad \forall t, \forall i \in \mathcal{N}$	(5.5c)
$\delta_t = \begin{cases} 1, & P_t^S \geq 0 \\ 0, & P_t^S < 0 \end{cases}$	(5.4d)	$P_t^S \geq -\alpha_i - \beta_i C_t^S, \quad \forall t, \forall i \in \mathcal{N}$	(5.5d)
$\lvert P_t^S \rvert \leq \hat{\alpha} + \hat{\beta}\sqrt{C_t^S}$	(5.4e)		

1. Accurate approximation of the FESS losses, capturing the dominant losses term $c_1\omega_r^2$ and the power losses from the charging/discharging modes. The high accuracy of the approximated FESS losses is experimentally validated for a real prototype FESS in Section 5.6.2.

2. Easy integration of commercial FESSs in practical applications because the FESS power losses are dependent on the SoC and charging/discharging power, independent of ω_r and J, which are readily available through a FESS interface.

3. Effective incorporation into mathematical programs as linear constraints that can be efficiently handled by appropriate optimization tools.

5.3.2 FESS maximum power

Constraint (5.4e) aims to restrict the maximum charging/discharging power through function $g(C_t^S)$. The dependence on C_t^S is explained below. The maximum charging/discharging power of a FESS system depends on the rated current limit ($\hat{I}$) of the machine side power electronics converter. For given $\hat{I}$, the rated converter power $\hat{P}$ is directly related to the stator voltage V of the FESS electrical machine [90], and expressed as

$$\hat{P}(t) = 3V(t)\hat{I}, \quad \forall t \in \mathcal{T}, \quad \Rightarrow \quad \hat{P} \sim V. \tag{5.6}$$

In permanent magnet synchronous machines (widely used in FESS applications), the stator voltage is directly related to the angular speed, given a constant magnetic flux, and given by

$$V(t) = K\Phi\omega_r(t), \quad \forall t \in \mathcal{T}, \quad \Rightarrow \quad V \sim \omega_r, \tag{5.7}$$

where K is a machine constant and Φ is the magnetic flux. Thus, V is directly related to ω_r such that $\hat{P} \sim \omega_r$ [91]. Since $C^S \sim \omega_r^2$, according to Eq. (5.3), it can be concluded that the maximum power is directly related to the square root of the SoC, i.e, $\hat{P} \sim \sqrt{C^S}$. Hence, we consider that $g(C_t^S) = \hat{\alpha} + \hat{\beta}\sqrt{C_t^S}$, where $\hat{\alpha}$ and $\hat{\beta}$ are positive constants, such that the maximum FESS power is constrained by (5.4e). The constants $\hat{\alpha}$ and $\hat{\beta}$ can be identified using linear regression either directly based on the maximum power curve provided in the FESS datasheet, or indirectly through measurements obtained from the FESS interface as presented in Section 5.6.2. Function $g(C_t^S)$ is monotonically increasing and concave, such that Eq. (5.4e) is convex. To avoid the introduction of general convex constraints in Problem $\mathbb{P}_{LEX}$, a piecewise linear approximation with N segments is constructed for $g(C_t^S)$. Let the i-th linear segment be $\alpha_i + \beta_i C_t^S$, $\forall i \in \mathcal{N} = \{1, ..., N\}$. Then, the affine constraints (5.5c)-(5.5d) provide the maximum values for $|P_t^S|$.

5.4 Solution methodology

This section presents the proposed methodology for the solution of the peak shaving problem under demand prediction errors, described in Section 5.2.

5.4.1 Control architecture

To deal with demand prediction errors, a two-level hierarchical control architecture is proposed, as shown in Figure 5.2. At the higher level, a model predictive controller (tertiary level control) optimizes the FESS power set-points, P_t^S, over a moving time horizon, $\mathcal{T}$, based on the transformer predicted net load demand, D_t^P, and the measured FESS SoC, I^c. At the lower level, a secondary controller compensates the net load prediction error by revising the FESS set-points at a shorter time-scale. A primary controller is embedded in the FESS (in the plant) that drives the power converters to regulate FESS operation in real time.

The time sequence of events of the considered control architecture is depicted in Figure 5.3. The MPC control step duration is set to T_{MPC}. Measurements are collected every T_m time-units for system monitoring and used as input to the controllers. The MPC controller solves Problem $\mathcal{P}_{LEX}$, using the latest SoC measurement, at the end

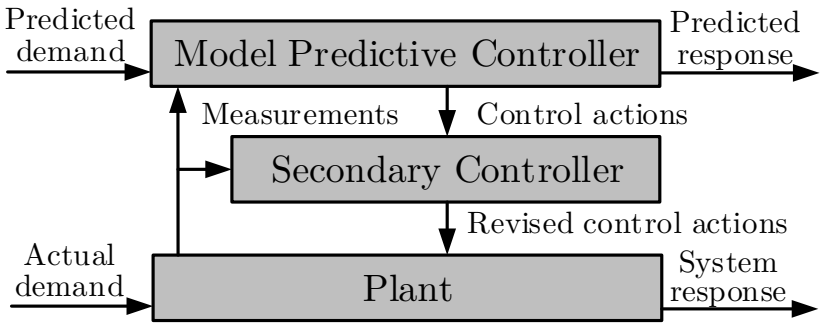

Figure 5.2: Hierarchical level control architecture.

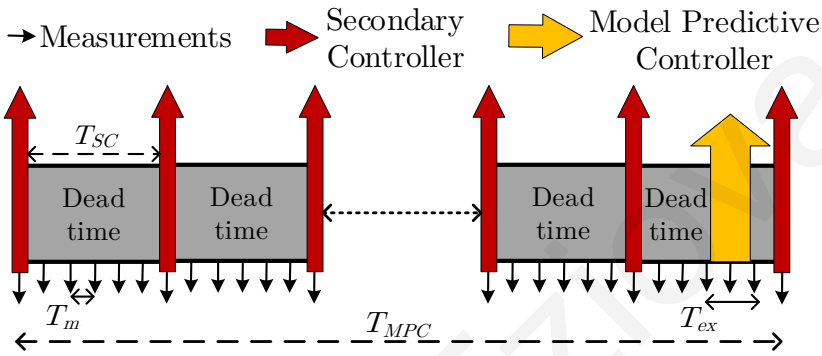

Figure 5.3: Time sequence of events in each cycle of the MPC framework.

of every MPC control-step, aiming to define the next FESS power set-point. The secondary controller updates the MPC-defined FESS set-point every T_{SC} time-units using the latest load measurement.

In multi-level control architectures, the inner loop needs to be significantly faster than the outer loop, $T_{MPC} > T_{SC}$, to decouple the dynamics between the two controllers. In addition, the maximum execution time needed for the solution of the MPC problem, T_{ex}, should be smaller than the MPC control-step such that $T_{MPC} > T_{ex}$. For monitoring both the dynamic and steady state operation of the FESS, measurements with higher sampling rate are required, yielding $T_m < T_{SC} < T_{MPC}$.

5.4.2 Model predictive controller

The MPC controller elaborates on the definition of Problem $\mathbb{P}_{LEX}$ to define a convex lexicographic optimization problem with four objectives. The first and second objectives minimize the transformer maximum power and energy violations, respectively, based on the predicted load. The third objective aims to sustain a minimum desirable SoC in the FESS that can be used by the secondary controller to compensate the transformer power violations due to the load uncertainty. Therefore, the third objec-

tive minimizes the SoC energy violations. The fourth objective minimizes the FESS energy losses. This lexicographic order gives first priority to the transformer safety; thus, the first and second objectives minimize the "expected" violations. The third objective aims to address "unexpected" violations. Last, the cost-effective operation is achieved by minimizing the FESS losses. According to the general principles of lexicographic optimization outlined in Section 2.2.2, the 4-objective Problem $\mathbb{P}_{LEX}$ can be solved by sequentially solving four single-objective problems, $\mathbb{P}_V$, $\mathbb{P}_E$, $\mathbb{P}_U$ and $\mathbb{P}_L$, associated with objectives $f_V(\mathbf{x})$, $f_E(\mathbf{x})$, $f_U(\mathbf{w})$ and $f_L(\mathbf{P}^L)$, respectively.

Problem $\mathbb{P}_V$ aims to eliminate the transformer power limit violations by minimizing the peak power violation of the transformer defined as $f_V(\mathbf{x}) = \max_{t\in\mathcal{T}}\{x_t\}$. Towards this direction, Problem $\mathbb{P}_V$ is defined as:

$$\min \quad f_V(\mathbf{x}) = \max_{t\in\mathcal{T}}\{x_t\} \qquad (\mathbb{P}_V) \tag{5.8a}$$

$$\text{s.t.} \quad \text{Constraints (5.1b), (5.1e)-(5.1g), (5.5a)-(5.5d),} \tag{5.8b}$$

$$P_t^F + P_t^S = D_t^P, \quad \forall t \in \mathcal{T}. \tag{5.8c}$$

Eq. (5.8c) has been used instead of (5.1d) because the actual demand is unknown. Problem $\mathbb{P}_V$ can be converted into a linear program by transforming the objective as: {minimize z, s.t. $0 \le x_t \le z$, $\forall t \in \mathcal{T}$}.

Let x_t^V denote the optimal values of x_t, $\forall t \in \mathcal{T}$, derived from the solution of Problem $\mathbb{P}_V$. Then, Problem $\mathbb{P}_E$ aims to minimize the total energy violations of the transformer yielding the formulation

$$\min \quad f_E(\mathbf{x}) = \sum_{t\in\mathcal{T}} x_t \Delta T \qquad (\mathbb{P}_E) \tag{5.9a}$$

$$\text{s.t.} \quad \text{Constraints (5.1b), (5.1e)-(5.1g), (5.5a)-(5.5d), (5.8c),} \tag{5.9b}$$

$$0 \le x_t \le \max_{t\in\mathcal{T}}\left\{x_t^V\right\}, \quad \forall t \in \mathcal{T}. \tag{5.9c}$$

Note that there is no need to solve Problem $\mathbb{P}_E$ when $\max_{t\in\mathcal{T}}\left\{x_t^V\right\} = 0$ because there are no transformer power limit violations. Simulation results in Section 4.5.2 indicate that the combination of the first and second objectives, $f_V(\mathbf{x})$ and $f_E(\mathbf{x})$, in this lexicographic order provides better results compared to the case that only one objective is used.

Problem $\mathbb{P}_U$ aims to handle demand prediction uncertainty by minimizing the SoC energy violations, w_t, to sustain a minimum desirable SoC, $\underline{C}_t^d$, according to Eq. (5.1c). Parameter $\underline{C}_t^d$ is a function of the predicted demand, D_t^p, that aims to maintain

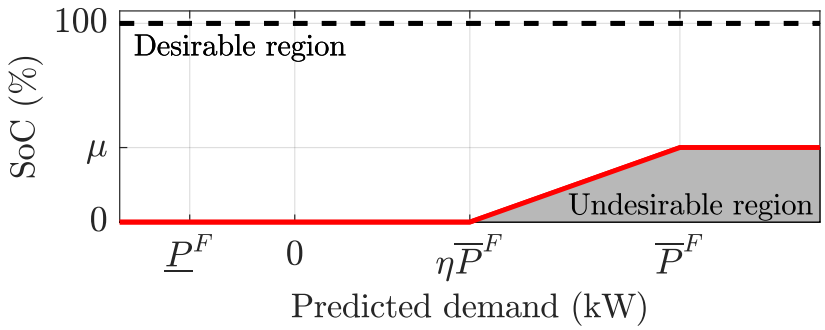

Figure 5.4: Minimum Desirable FESS SoC as a function of the predicted demand.

enough stored energy in the FESS when the transformer operates close to its maximum limit. This amount of stored energy can be utilized by the secondary controller to prevent direct power flow violations due to demand prediction uncertainty. We define $\underline{C}_t^d$ as

$$\underline{C}_t^d = \begin{cases} 0, & \text{if } D_t^P \leq \eta\overline{P}^F, \\ \frac{\mu}{(1-\eta)\overline{P}^F}(D_t^P - \eta\overline{P}^F), & \text{if } \eta\overline{P}^F \leq D_t^P \leq \overline{P}^F, \\ \mu, & \text{otherwise.} \end{cases} \tag{5.10}$$

Notice that $\underline{C}_t^d = 0$ when the predicted demand is small, $D_t^P \leq \eta\overline{P}^F$, to avoid unnecessary FESS energy losses; further increase of the predicted demand increases linearly $\underline{C}_t^d$, until a maximum value μ is reached. The specific definition of $\underline{C}_t^d$ creates a desirable region of the FESS SoC, as shown in Figure 5.4. Hence, Problem $\mathbb{P}_U$ aims to manage demand prediction uncertainty by minimizing the total SoC energy violations, yielding the formulation:

$$\min \quad f_U(\mathbf{w}) = \sum_{t\in\mathcal{T}} w_t \Delta T \qquad (\mathbb{P}_U) \tag{5.11a}$$

$$\text{s.t.} \quad \text{Constraints (5.1b)-(5.1c), (5.1e)-(5.1g),} \tag{5.11b}$$

$$\text{(5.5a)-(5.5d), (5.8c),} \tag{5.11c}$$

$$0 \leq x_t \leq x_t^E, \qquad \forall t \in \mathcal{T}. \tag{5.11d}$$

In Problem $\mathbb{P}_U$, x_t^E denotes the optimal values of variables x_t, $\forall t \in \mathcal{T}$ obtained from the solution of Problem $\mathbb{P}_E$.

Finally, Problem $\mathbb{P}_L$ aims to achieve economic efficiency for the FESS by minimizing its total energy losses while ensuring minimum transformer power violations

Algorithm 5 : FESS power set-point correction every 30 s

1: **Input:** P^S, P^F and $\hat{D}^A$.
2: **if** $(\hat{D}^A - P^S) > \max(P^F, \overline{P}^F)$ **then**
3: Set $P^R = \hat{D}^A - \max(P^F, \overline{P}^F)$;
4: **else if** $(\hat{D}^A - P^S) < \min(P^F, \underline{P}^F)$ **then**
5: Set $P^R = \hat{D}^A - \min(P^F, \underline{P}^F)$;
6: **else**
7: Set $P^R = P^S$;
8: **Output:** P^R.

and minimum total SoC energy violations:

$$\min \quad f_L(\mathbf{P}^L) = \sum_{t \in \mathcal{T}} P_t^L \Delta T \qquad (\mathbb{P}_L) \tag{5.12a}$$

$$\text{s.t.} \quad \text{Constraints (5.1b)-(5.1c), (5.1e)-(5.1g),} \tag{5.12b}$$

$$\text{(5.5a)-(5.5d), (5.8c), (5.11d),} \tag{5.12c}$$

$$0 \leq w_t \leq w_t^*, \quad \forall t \in \mathcal{T}. \tag{5.12d}$$

In Problem $\mathbb{P}_L$, w_t^* denotes the optimal values of variables w_t, $\forall t \in \mathcal{T}$ obtained from the solution of Problem $\mathbb{P}_U$.

In sum, every T_{MPC} the MPC controller sequentially solves Problems $\mathbb{P}_V$, $\mathbb{P}_E$, $\mathbb{P}_U$, and $\mathbb{P}_L$. All four problems can be fast and reliably solved using linear programming.

5.4.3 Secondary controller

Algorithm 5 describes the operation of the secondary controller that compensates the transformer power limit violations by handling the load uncertainty. This controller takes as input the FESS power set point, P^S, and transformer operating power, P^F, predicted from the MPC controller for the current 3-minute time cycle, as well as the latest measurement of the actual net load $\hat{D}^A$. The aim of the secondary controller is to operate the transformer between the minimum and maximum permissible power points defined as $\min(P^F, \underline{P}^F)$ and $\max(P^F, \overline{P}^F)$, respectively. Hence, the secondary controller provides a revised FESS power set-point P^R every T_{SC} s by considering three cases:

1. The transformer is set to operate at the maximum permissible point if this point

is violated considering the MPC-based set-points and the latest measured net load (Lines 2-3).

2. The transformer is set to operate at the minimum permissible point if this point is violated (Lines 4-5).

3. Otherwise, the FESS power set-point remains unaltered (Lines 6-7).

Note that the FESS power and energy limits are ensured by the embedded primary controller in the real FESS. In the simulations, the power and energy limits are ensured in the Plant by projecting[1] parameter P^R to its feasible set defined by Eqs. (5.1e) - (5.1g) and (5.4e).

5.5 Simulation results

The simulation setup is comprised of a FESS installed in a transformer substation with direct and reverse power flow limits of 500 kW and −200 kW, respectively. For comparison purposes two FESSs are considered:

- The *scaled-up prototype FESS* is a 100-times scaled-up version of a real prototype FESS[2]. The scaled-up prototype FESS has a rated capacity of 185 kWh and 600 kW charging/discharging power. Its power losses and maximum power coefficients are $\hat{b}^c = 0.106, \hat{c}^c = 0.394$, $\hat{b}^d = 0.223, \hat{c}^d = 0.419$, $\hat{\alpha} = 0.172$ and $\hat{\beta} = 0.622$. These coefficients correspond to the ones identified experimentally for the real prototype FESS in Section 5.6.2.

- The *commercial FESS* has the same rated capacity and maximum charging/discharging power with the scaled-up prototype FESS. Its power losses and maximum power coefficients are $\hat{b}^d = \hat{b}^c = 0.075$, $\hat{c}^d = \hat{c}^c = 0.2$, $\hat{\alpha} = 0.172$ and $\hat{\beta} = 0.622$. These power losses coefficients correspond to 85% round-trip efficiency and 20% standby losses per hour [69].

Unless otherwise stated, $N = 10$ segments are used for the piecewise linear approximation of the FESS maximum power of both FESSs, according to Eqs. (5.5c) - (5.5d).

[1]The projection of point x_0 on a set C, is defined as the point $x_P \in C$ that is closest to x_0 according to some distance metric $\| \bullet \|$, i.e., $x_P = \text{argmin}\{\|x - x_0\| \, | x \in C\}$. For example, the projection of x_1 on the set $[\underline{x}, \overline{x}]$ is simply $x_P = \max(\underline{x}, \min(\overline{x}, x_1))$ [17].

[2]The real prototype FESS is employed in Section 5.6 for experimental validation.

Section 5.5.1 investigates the performance of the proposed methodology in two 6-hour scenarios, $T = 6$ hours, where *Scenario 1* has no uncertainty, while *Scenario 2* has model and net load demand uncertainty. Section 5.5.2 provides aggregate results on the capability of the proposed controllers to provide peak shaving services under net load demand uncertainty, using historical data from a real distribution grid. The time-horizon is set to $T = 24$ hours. The timing parameters of the control architecture for both sections are set to: $\Delta T = 3$ min, $T_{MPC} = 3$ min, $T_{SC} = 30$ s, $T_m = 5$ s, and $T_{ex} = 10$ s. The solution of Problem $\mathbb{P}_{LEX}$ takes place in the interval [165, 175] s of each MPC control-step. The allowed 10-second interval for the solution of the MPC Problem $\mathbb{P}_{LEX}$ is more than enough, as Problems $\mathbb{P}_V$, $\mathbb{P}_E$, $\mathbb{P}_U$, and $\mathbb{P}_L$ are medium-scale linear programs. These problems are solved using Gurobi [43]. Note that the predicted demand is usually available for 15-minute time intervals [73]; however, this chapter considers $\Delta T = T_{MPC} = 3$ min to provide updated control actions in shorter times, because the model uncertainty and the SC operation can affect the FESS SoC.

5.5.1 Performance evaluation - Synthetic data

Scenario 1

This scenario investigates the capability of the proposed MPC controller to provide peak shaving services to the distribution grid. Because there is no uncertainty, the secondary controller is not utilized in this scenario. Therefore, the control actions of the MPC controller are passed directly to the Plant, without revision by the secondary controller (see Figure 5.2). Regarding the minimum desirable SoC, it is set that $\mu = 15\%$ and $\eta = 70\%$.

Figure 5.5(a) presents the net load demand and the transformer operation using the two FESSs. To induce reverse and direct power violations, the net load is selected to have excessive PV generation and low load demand during noon and the opposite during afternoon hours. The results illustrate that the MPC controller successfully shaves the power peaks to maintain operation within safety limits. In detail, the reverse power violations, observed during [0.5 h, 1.25 h], are eliminated by charging the two FESSs from the excess PV production, as can be seen in Figure 5.5(b). Notice in Figure 5.5(c) that the surplus energy stored and re-injected into the grid is larger for the commercial FESS because it has lower standby losses compared

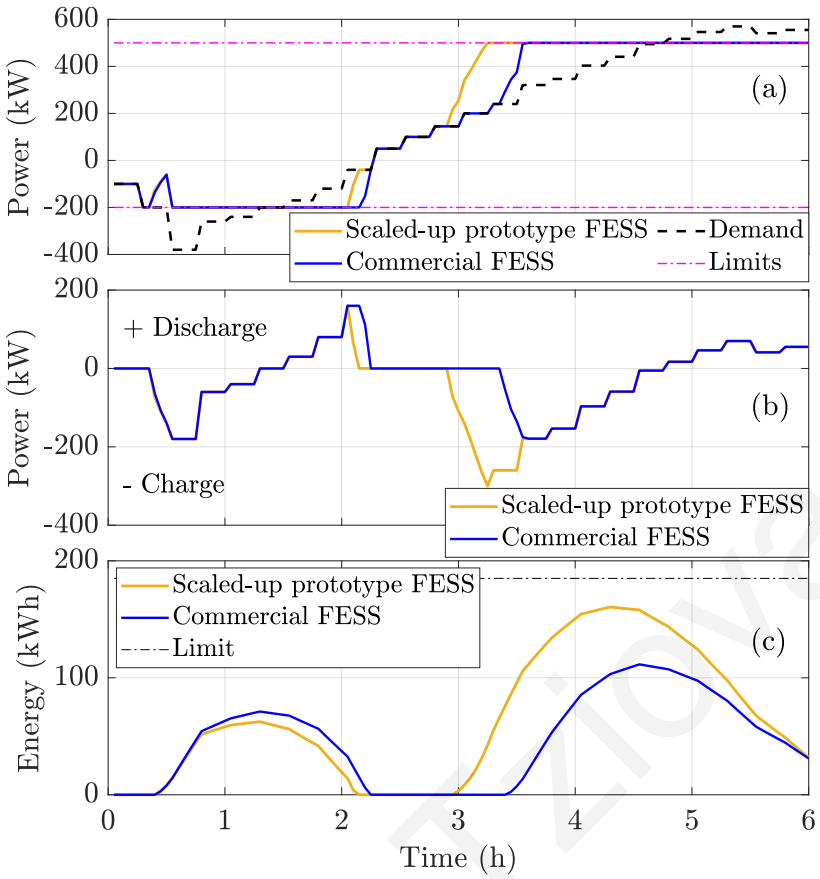

Figure 5.5: Power scheduling using the scaled-up prototype and the commercial FESS: (a) Predicted net load demand and transformer power using the two FESSs, (b) FESS power set-points of the MPC controller, and (c) Stored energy in the prototype and commercial FESS.

Table 5.2: Objectives effectiveness in minimizing power violations

Objectives	Peak power violation	Total energy violations
MinMax	4.1 kW	18.8 kWh
MinEnergy	85.1 kW	5.4 kWh
Lexicographic	4.1 kW	8.3 kWh

to the prototype FESS. Due to the standby losses, the stored energy during [0.5 h, 1.25 h] is not maintained to address direct power violations, observed during [4.75 h, 6 h]. However, direct power violations are eliminated by charging the two FESSs from the grid prior to the violation period and reusing the stored energy to satisfy the excess load demand. As expected, the SoC at $T = 6$ h is 15% due to the minimum desirable SoC.

We further consider a case where the transformer maximum limit is reduced from

500 to 470 kW such that the safety limits cannot be satisfied, considering only the scaled-up prototype FESS. Table 5.2 presents the transformer peak violations and total energy violations under three objectives:

1. *MinMax* minimizes the transformer peak power violation as defined in Eq (5.8a).

2. *MinEnergy* minimizes the total energy violations as defined in Eq (5.9a).

3. *Lexicographic* combines the above two objectives and is defined as lexmin$\{f_V(\mathbf{x}), f_E(\mathbf{x})\}$.

From the results is it evident that the Lexicographic objective is the best as it achieves the smallest possible peak violation (4.1 kW or 0.8% overloading) with only a small increase in the transformer total energy violations (2.9 kWh).

The *Lexicographic* objective is also used to investigate the impact of the piecewise linear approximation of Eq. (5.4e) on the total energy violations when the transformer maximum limit is 470 kW. As shown by the solid orange line of Figure 5.6, there is no impact of N on the total energy violations under the FESS maximum power is 600 kW ($\gamma = 100\%$). For this reason, we re-scale the FESS maximum power limits in Eqs. (5.1g) and (5.4e) by a scaling factor γ, yielding the new constraints

$$\gamma \underline{P}^S \leq P_t^S \leq \gamma \overline{P}^S, \ \forall t \in \mathcal{T},$$
$$|P_t^S| \leq \gamma(\hat{\alpha} + \hat{\beta}\sqrt{C_t^S}), \ \forall t \in \mathcal{T},$$

and examine the performance for $\gamma = \{70\%, 50\%, 30\%\}$. Interestingly, the energy violations are considerably, moderately and marginally reduced when N increases from 2 to 5, 5 to 10 and 10 to 20, respectively. Hereafter, it is considered in all experiments that $N = 10$.

Scenario 2

Scenario 2 extends the simulation setup of Scenario 1 for the scaled-up prototype FESS by considering model and net load demand uncertainty. As a result, both controllers are utilized; the MPC controller computes the FESS power set points using the predicted demand and estimated model, while the secondary controller corrects the provided points based on real-time measurements. Modelling uncertainty is introduced by increasing the FESS power losses by +5%. To introduce demand uncertainty, the predicted demand is computed as the 15-minute piecewise

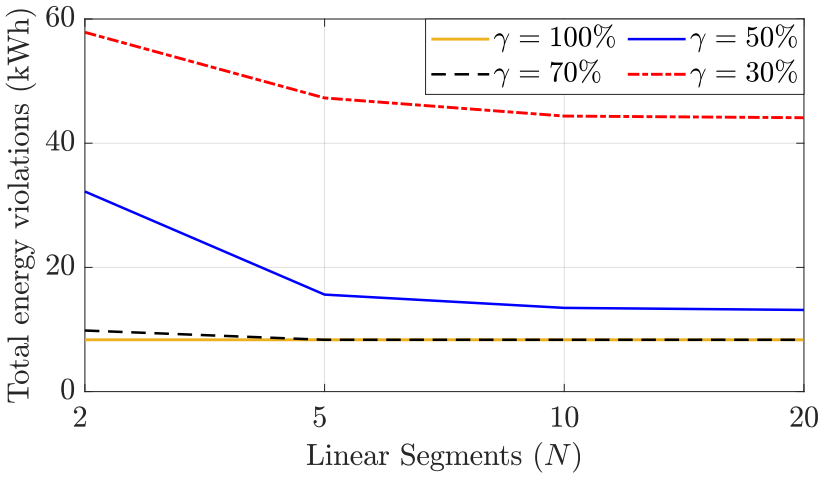

Figure 5.6: Transformer energy violations for different number of segments, N, when the scaling factor γ is equal to 100%, 70%, 50% and 30%.

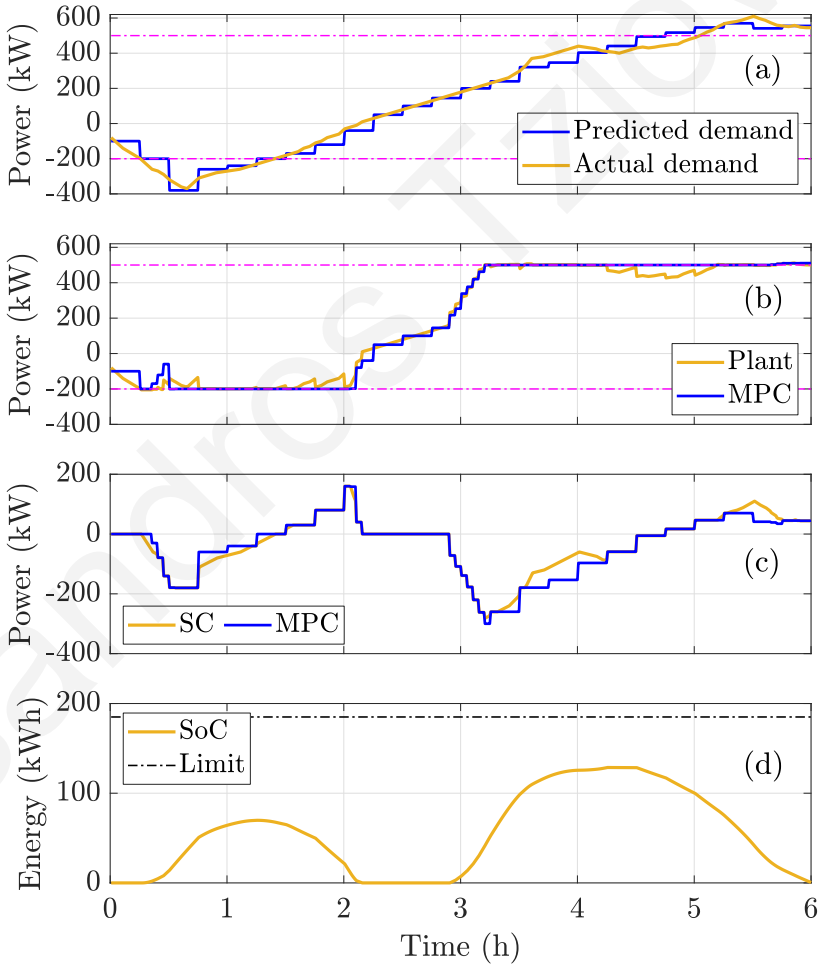

Figure 5.7: Power scheduling using the scaled-up prototype FESS under uncertainty: (a) Actual and predicted net load demand, (b) Actual (Plant) and predicted (MPC) transformer power, (c) FESS power set-points of the MPC and secondary (SC) controllers, and (d) Stored energy in the FESS.

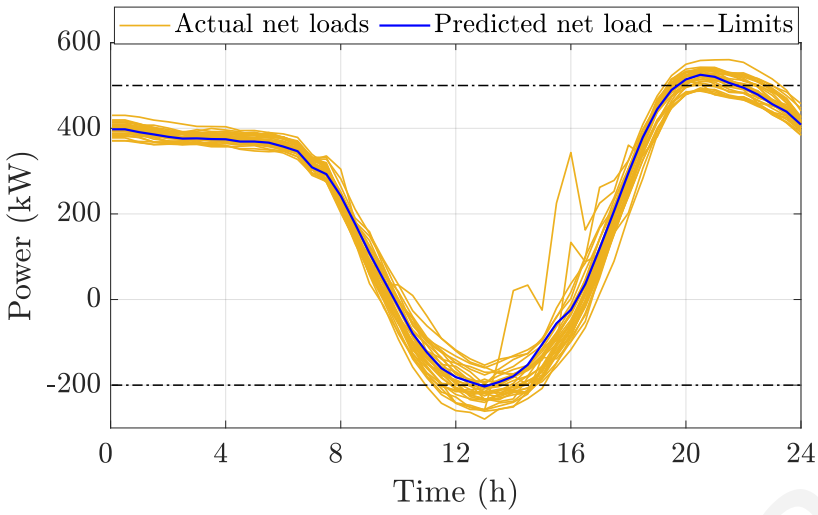

Figure 5.8: Actual and predicted net load curves constructed from historical data of a real distribution grid.

constant approximation of the actual demand; the mean, standard deviation, minimum and maximum demand prediction error is 1.5 kW, 38.6 kW, -91.7 kW and 115 kW, respectively.

Figure 5.7(a) illustrates the actual and predicted demand and Figure 5.7(b) presents the actual and predicted transformer power, produced by the Plant and the MPC controller. Despite the introduced uncertainty, the proposed controllers can still handle well the reverse and direct power violations. This is also indicated in Figure 5.7(c) by the revised FESS power set-points of the secondary controller which correct the set-points of the MPC controller. The minimum desirable SoC is vital in making these corrections; for example, the unpredicted extra demand experienced in the period [5h, 6h] is compensated using the FESS minimum desirable SoC, resulting in almost 0% SoC at the end of the 6-hour scenario.

5.5.2 Performance evaluation - Real data

This section examines the capability of the proposed controllers to provide peak shaving services under net load demand uncertainty, using historical data from a real distribution substation in Larnaca, Cyprus. Figure 5.8 demonstrates 31 actual net load curves that are obtained from the distribution transformer for July 2019, as provided by the Electricity Authority of Cyprus (Cyprus DSO). It also presents a predicted net load curve constructed as the average of the actual net load curves of July 2018. The distribution grid includes mainly residential loads of a rural area and

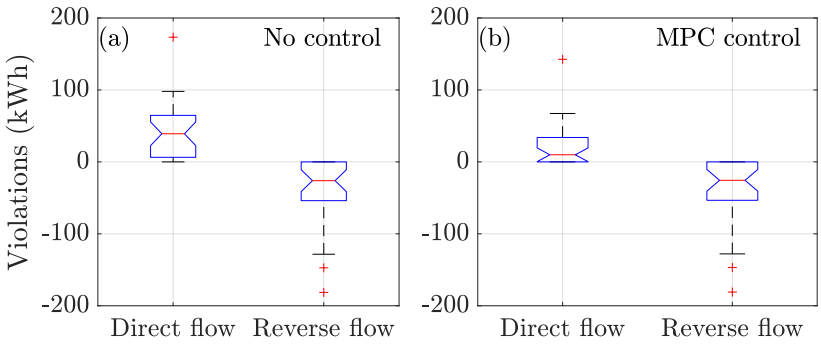

Figure 5.9: Direct and reverse energy violations when (a) the proposed control scheme is not utilized and (b) the MPC controller is used, but the secondary controller is deactivated.

there is intense penetration of large PV parks, causing high reverse and direct power flows during the noon and evening hours, respectively, as can be seen in Figure 5.8. As power violations do not occur in the real distribution transformer, due to its large size, we consider a smaller transformer with peak reverse and direct capability of -200 kW and 500 kW. The performance of the proposed controllers is examined for the commercial FESS using as input the actual and predicted net load curves of Figure 5.8 for the Plant and the MPC, respectively, according to Figure 5.2.

Figures 5.9 (a) and (b) illustrate the energy violations of the 31 actual curves, in box-plot form[3], that are caused due to the direct and reverse power flow violations, when no control and MPC control are used, respectively. Although MPC control achieves better results compared to no control, it still suffers from high energy violations because only the "expected" violations that are covered by the predicted net load curve are addressed. Note that the values of μ and η do not affect the energy violations, because the secondary controller is deactivated.

When both the MPC and secondary controllers are utilized, the reverse energy violations are completely eliminated because the secondary controller stores all the "unexpected" violated energy in the FESS. Nevertheless, the "unexpected" violated energy from the direct power flow is more challenging to be addressed, because the FESS must be charged in advance to provide the violated energy. Figure 5.10 presents the direct energy violations of the actual curves for different values of

[3]The bottom and top of each box indicate the first and third quartiles (25% and 75%) of a ranked data set, while the horizontal line inside the box indicates the median value (second quartile). The horizontal lines outside the box indicate the lowest/highest datum still within 1.5 inter-quartile range of the lower/upper quartile; for normally distributed data this corresponds to approximately 0.35%/99.65%.

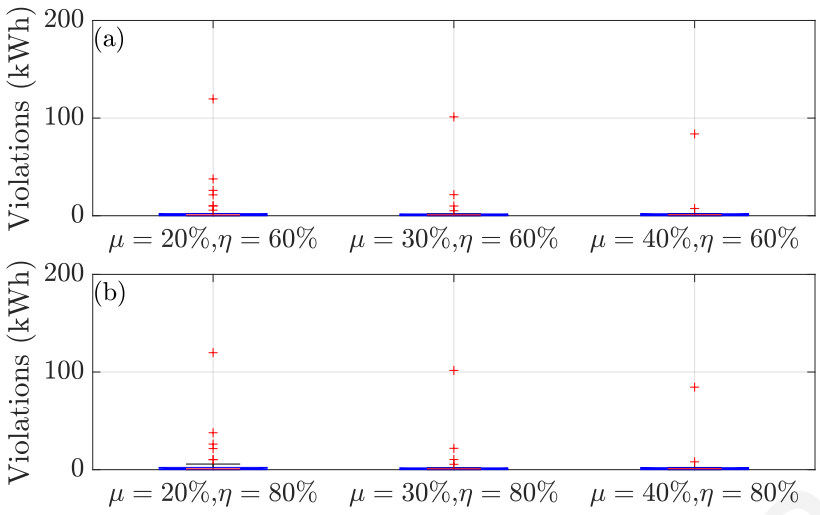

Figure 5.10: Direct energy violations, in box-plot form, for different μ and η when both the MPC and secondary controllers are utilized. The reverse energy violations are eliminated in every case.

μ and η (see Eq. (5.10)). As expected, the energy violations are reduced as the value of μ increases, because more energy is maintained in the FESS to address the "unexpected" violations. In contrast, parameter η has negligible effect on the results; nonetheless, higher values of η are more preferable to avoid unnecessary power losses due to the FESS operation. As shown in Figure 5.10, the proposed controllers compensate well for the "unexpected" energy violations of the considered days for μ = 40%. However, high energy violations are still present in one particular day with total energy violations of 173.3 kWh (see the Direct flow in Figure 5.9 (a)). This amount of energy cannot be compensated by the considered FESS with capacity 185 kWh, efficiency 85% and standby losses 20%. The main conclusions of this section are summarized as:

1. In cases with high net load uncertainty, the utilization of both the MPC and secondary controllers is essential to address the "unexpected" power and energy violations.

2. The violations are reduced by increasing parameter μ; η has negligible effect on the results.

3. The FESS capacity is an important factor that affects the performance of the proposed controllers, since small values impose energy limitations that can lead to transformer power limit violations.

5.6 Experimental validation

In this section, the proposed controllers are evaluated in a realistic experimental setup using a real prototype FESS. Prior to the performance evaluation, the experimental setup is described and used to identify the parameters of the power losses and maximum power FESS functions.

5.6.1 Experimental setup

As shown in Figure 5.11, the experimental setup is comprised of five main modules: (M1) the Physical System, (M2) the Core Context Management, (M3) the Communication Context, (M4) the Processing Context, and (M5) the Visualization Context. The *Physical System* represents the considered smart-grid configuration presented in Figure 5.1. It is comprised of a prototype FESS with 6 kW total rated power and a usable capacity of 1.85 kWh, a 4.05 kW load bank with nine equal controllable switching steps and a 5 kW PV system, connected to the power grid and installed in our power systems laboratory. The FESS is based on two 150 kg flywheels with a rated speed of 14000 RPM and the PV system is based on a commercial Fronius Symo 5.0 inverter associated with a Chroma 62150H PV emulator. Measurements of the various system states (actual load, grid power) are obtained through smart meters while the PV generation and the FESS charging/discharging power and SoC are obtained through the inverter and FESS interfaces.

To enable the interaction between the controllers and the physical system, a software platform based on FIWARE [84] has been developed (modules M2 - M5). FIWARE is a framework of an open source platform modules which can be assembled together to accelerate the development of smart solutions, such as the real-time monitoring and control of a FESS in a smart grid environment. In the developed FIWARE-based software platform, the *Core Context Management* module is responsible for creating and managing context information elements through the Orion Context Broker sub-module, as well as storing, querying and retrieving data using QuantumLeap from the back-end database (CrateDB). The exchange of information between the Core Context Management and the Physical System is achieved through the *Communication Context* module where a Python script has been developed to transfer real-time measurements from the smart meters to the Core Context Management. Measurements are submitted to the Processing Context module and

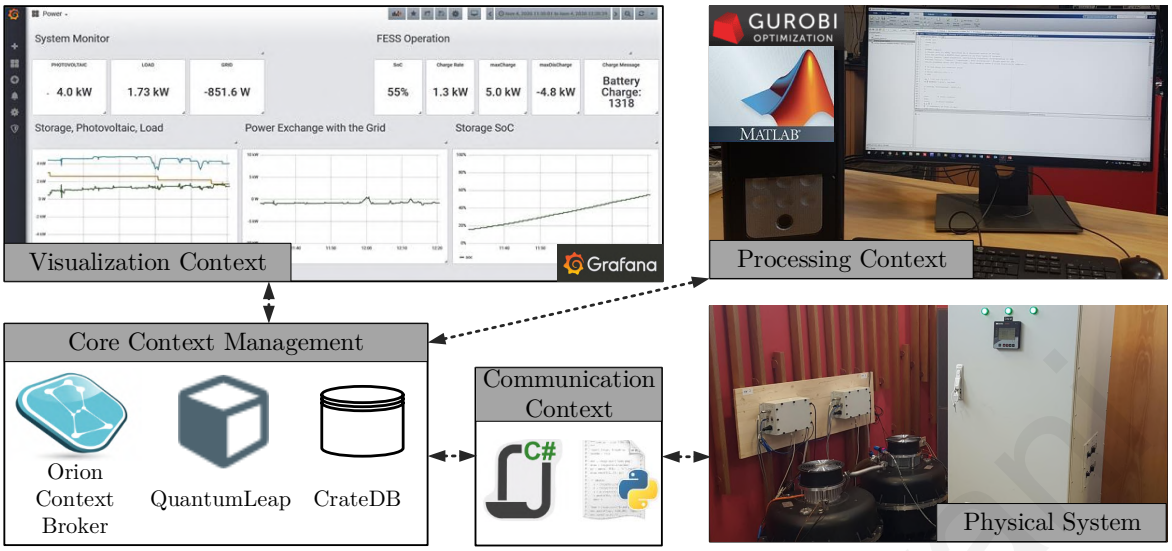

Figure 5.11: Monitoring and control of the FESS for providing distribution grid services using a software platform based on FIWARE.

are displayed graphically on the *Visualization Context* (developed using Grafana web application) to monitor the system. The *Processing Context* module implements the proposed controllers in Matlab/Gurobi and calculates the FESS commands which are submitted for execution to the Physical System through a C# script. Measurement and control data between the Physical System and the Core Context Management are exchanged through the laboratory Local Area Network (LAN). Note that the experimental setup operates according to the three different time scales presented in Figure 5.3.

5.6.2 FESS model validation and parameter identification

This section validates the proposed model for the power losses, Eqs. (5.5a)-(5.5b), and maximum power, Eqs. (5.5c)-(5.5d), of the employed prototype FESS. To derive the charging power losses, the FESS operation was regulated with a constant charging power for varying SoC and maximum allowable power. The power losses were then calculated at each operating condition pairs (SoC, charging power) as the difference between the measured absorbed energy for charging and the measured stored energy in the FESS. For example, the power losses at 50% SoC and 2 kW charging power are derived by the difference between the energy drawn from the grid and the FESS stored energy for a SoC increase from 45% to 55% using a constant charging power of 2 kW. A similar approach was used for the discharging mode.

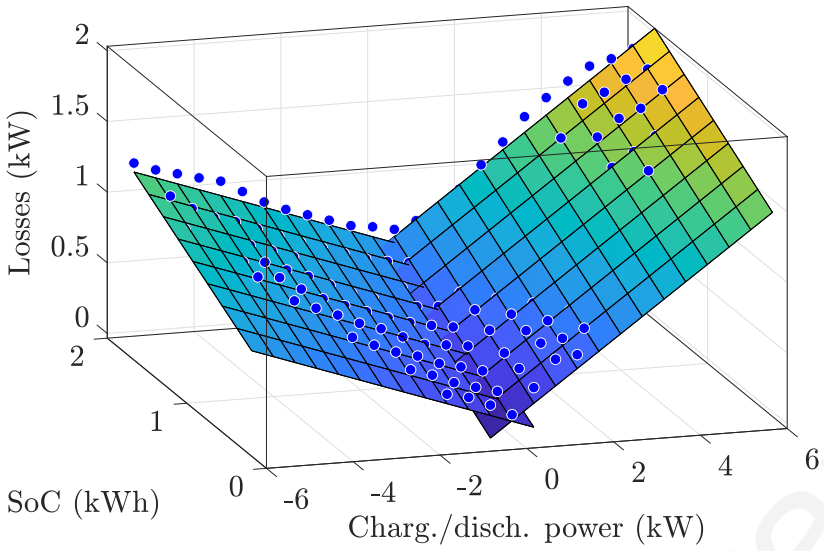

Figure 5.12: The FESS power losses for varying SoC and charging/discharging power. The two intersecting planes is the result from linear regression using the sample points and the dots indicate sample points located above the planes.

Table 5.3: Regression Analysis - Parameter Identification

Charg. mode - Eq. (5.4c)	Disch. mode - Eq. (5.4b)	Max. power - Eq. (5.4e)
$\hat{b}^c = 0.106, \hat{c}^c = 0.394$	$\hat{b}^d = 0.223, \hat{c}^d = 0.419$	$\hat{\alpha} = 0.172, \hat{\beta} = 0.622$
Adjusted $R^2 = 0.973$	Adjusted $R^2 = 0.961$	Adjusted $R^2 = 0.996$
RMSE = 0.046	RMSE = 0.103	RMSE = 0.081

The FESS power losses as a function of the charging/discharging power and the SoC are illustrated in Figure 5.12. From the figure two important observations can be made. First, the FESS power losses become higher as the charging/discharging power and the SoC increase. Second, the maximum power depends on the SoC, as shown in Figure 5.13, and thus the measurements on the power losses do not span the entire SoC/maximum power region. Due to this limitation, the total number of measurements were 166 instead of 225 when the SoC and maximum power vary in the ranges $\{10, 20, ..., 90\%\}$ and $\{-6, -5.5, ..., 5.5, 6$ kW$\}$, respectively. The maximum charging/discharging power limitation is further verified according to experimental measurements received from the FESS interface, as shown in Figure 5.13, which indicates that the maximum power is a monotonically increasing concave function of the SoC.

Linear regression was used to model the FESS power losses (kW) as a function of the SoC (kWh) and the charging or discharging rate (kW). Table 5.3 presents the iden-

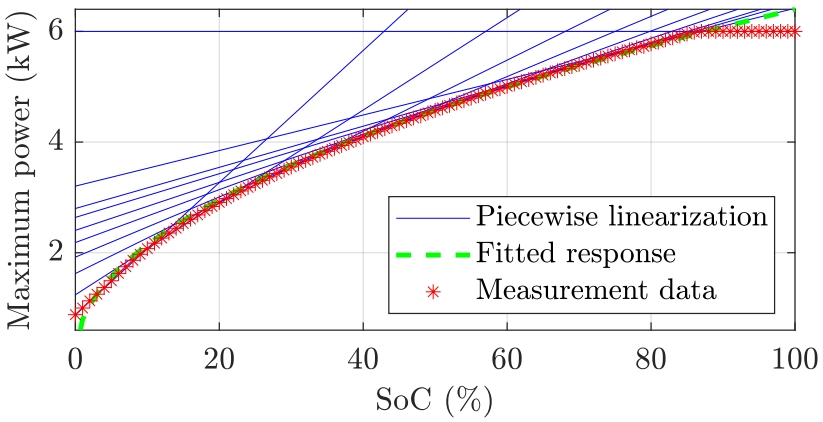

Figure 5.13: The maximum charging/discharging power of the FESS as a function of the SoC obtained from 100 experimental samples. The dashed line is the fitted response using regression. The ten blue solid lines construct a piecewise linear approximation of the concave function produced from the samples.

tified parameters of the two linear models for the charging and discharging modes, according to Eqs. (5.4b)-(5.4c) or Eqs. (5.5a)-(5.5b), along with two coefficients to determine the goodness of fit. The *Adjusted Coefficient of Determination* (Adjusted R^2) falls very close to 1 (Adjusted $R^2 > 0.95$) in both cases; this indicates that the derived models explain more than 95% of the variance in the power losses. The goodness of fit is also indicated by the small *Root Mean Squared Error* (RMSE) values which are less than 0.105 kW in both cases.

The results of the linear regression are illustrated in Figure 5.12 by the two intersecting planes representing the power losses for the charging and discharging mode. As can be seen, the two intersecting planes define a convex function which explains the selection of Eqs. (5.5a)-(5.5b).

Similarly, the parameters of the maximum power model, Eq. (5.4e), are identified using linear regression based on the measurements depicted in Figure 5.13. Table 5.3 shows an excellent goodness of fit having an Adjusted R^2 value larger than 0.99 and a RMSE smaller than 0.01 kW. The fitted model and a 10-segment piecewise linear appproximation of the model are shown in Figure 5.13. These linear segments are used to derive convex constraints on the maximum power in (5.5c)-(5.5d).

5.6.3 Experimental results

To experimentally evaluate the two proposed controllers, we consider a 3-hour scenario, $T = 3$ hours, with power grid limits of 3.3 kW and -1 kW and the experimental

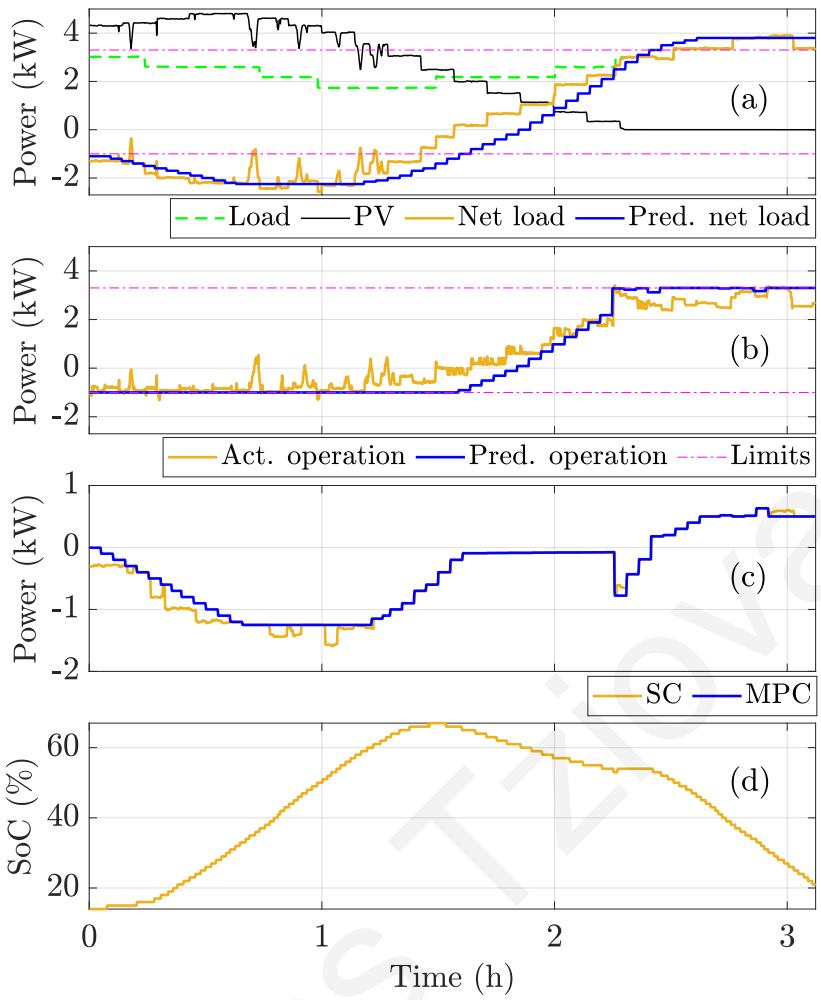

Figure 5.14: Experimental validation using the prototype FESS: (a) Input data, (b) Actual (Plant) and predicted (MPC) transformer operation, (c) FESS charging/discharging power based on the MPC and secondary controllers (SC), and (d) SoC.

setup described in Section 5.6.1. The timing parameters used in Section 5.5 for the control architecture remain the same. Figure 5.14(a) shows the PV generation and load demand of the physical system, as well as actual and predicted net load demand. Figure 5.14(b) illustrates that the controllers successfully shave the peaks exceeding the power limits in almost all cases. Figure 5.14(c) presents the FESS power set-points of the MPC and secondary controllers. As can be seen, major deviations between the controllers output are experienced during the period [0h, 1h]; however, the secondary controller manages to successful compensate the unpredicted extra net load demand and maintain the power grid limits. Finally, the FESS SoC due to the charging/discharging power is illustrated in Figure 5.14(d).

5.7 Practical implementation considerations

The practical implementation of the proposed energy management and control scheme for providing peak shaving services requires proper consideration of (a) the transformer power limit violations, (b) the cost-effective operation of the system, and (c) communication and cybersecurity issues.

The size (capacity) of the FESS is a key aspect that can lead to violations of the transformer power limit. As presented in Section 5.5.2, a small FESS imposes energy limits and violations can occur. Thus, before the investment, a planning study must be carried out, considering the historical and future power profiles of the transformer, to determine the adequate size of the FESS for each application. In addition, the utilization of an accurate predicted curve for the transformer net load is required to enhance the performance of the proposed scheme. This predicted curve can be constructed using forecasting data and/or historical data, as indicated in Section 5.5.2. In case the proposed scheme fails to eliminate all violations, PV curtailments and/or load shedding must be applied to avoid overloading the distribution transformer.

The FESS efficiency and standby losses is an important factor that should be considered for the cost-effective operation of the system in real applications. Low efficiency and high standby losses result in significant total energy losses that affect the sustainability of the investment. In addition, high energy losses affect the FESS mission profile (charging/discharging power) resulting in higher power rates which can affect the lifetime of the FESS power electronics, especially when the system operates near to its rate limits [92]. Such a case was illustrated in Figure 5.5, where the prototype FESS resulted in significantly higher charging power compared to the more efficient commercial FESS.

Secure communication is also a major concern in smart grid applications. In this chapter, measurement and control data between the Core Context Management and the Physical System are exchanged through a LAN, since all modules of the experimental setup, presented in Figure 5.11, were located within the same building. However, in real-world applications, the physical systems may be distributed far away from the central Monitoring and Processing Contexts (server or cloud-based). In this case, secure and reliable communication can be achieved over the Internet using different methods. Two indicative approaches are the following. The first approach is to use a Virtual Private Network (VPN) router at the physical system

level to facilitate secure communication with a central processing server. The second approach is to use a local controller with firewall protection to maintain communication between the components at the physical level through a LAN. In the latter case, only the local controller can communicate over the Internet with the central Processing Context in a bi-directional way using secure Internet of Things (IoT) protocols such as the Message Queuing Telemetry Transport (MQTT) protocol.

5.8 Conclusions

In this chapter, an energy management and control scheme is proposed to provide peak shaving services to the distribution grid using a FESS. Convex functions that represent the FESS power losses and maximum power are derived and incorporated in a novel lexicographic optimization that defines the FESS power set-points. A two-level hierarchical control scheme is proposed for the solution of the lexicographic optimization to deal with demand prediction errors and modelling uncertainty. In this study the proposed FESS modelling is experimentally validated and the FESS parameters are identified. Simulation and experimental results validate the effectiveness of the proposed energy management and control scheme to provide peak shaving services under realistic conditions. The proposed scheme enables the active management of distribution grids and increases the hosting capacity for PV installations and load demand growth in existing power grids.

Chapter 6

Stochastic optimization of the bidding strategy of RES producers in electricity markets considering battery degradation

Battery energy storage systems (BESSs) is an emerging technology that can enhance the flexibility and controllability of wind and photovoltaic power plants. This work develops a bidding strategy for combined BESS and renewable energy source (RES) plants to maximize the expected profit of producers in day-ahead energy and balancing markets, considering battery degradation and power exchange limitations with the grid due to transmission congestion. The resulting problem is challenging to solve due to the non-convex degradation and power loss models of the BESS, and the uncertainties arising from RES generation and energy prices. To address the non-convexities associated with the BESS, a linear deterministic optimization scheme is developed that incorporates an approximate cycle-based degradation model and a relaxed BESS model. To handle uncertainties in RES power generation, day-ahead energy prices, and imbalance prices, a scenario-based linear stochastic optimization scheme is developed that can be fast and reliably solved. Simulation results, using real data from a wind and PV plant, demonstrate the effectiveness of the proposed stochastic scheme in enhancing the profit of producers compared to (a) the corresponding deterministic scheme and (b) a base scenario where the RES forecasting generation profile is directly submitted to the market.

6.1 Introduction

The requirement for RES plants to participate in electricity markets presents opportunities to maximize profits by taking advantage of market operations. This includes buying and storing energy when prices are low and selling when prices are high. RES producers who participate in day-ahead energy markets are paid based on their scheduled RES production profile submitted to the market for the next day [93]. However, since day-ahead prices are unknown, producers must make decisions based on forecasted prices, which may reduce their profits in case of high forecasting errors. Additionally, forecasting errors in RES power generation create power imbalances that threaten the stability of the power system. Power imbalances can result in power deficits which are penalized at higher costs compared to day-ahead prices, or power excesses which are paid at lower prices [94]. This incentivizes RES producers to submit accurate scheduled production profiles to the day-ahead market to maximize profits. This chapter aims to develop a bidding strategy for RES-BESS producers to maximize profits by buying and selling power in electricity markets, considering power exchange limits with the grid to ensure transmission system restrictions.

The insufficiency of the power grid infrastructure to accommodate the variable RES generation due to transmission constraints may lead to RES power curtailments, which can deteriorate the profits of RES producers. When the total RES generation cannot be injected into the power grid due to limitations related to the transmission congestion, energy storage systems (ESSs) can store the surplus RES generation to avoid RES curtailments. A real-time operation strategy of a wind-storage system to maximize the producer profits by reducing the wind curtailment cost due to transmission congestion is presented in [95]. Similarly, deterministic energy management schemes for BESSs operating in photovoltaic (PV) power plants considering power grid limits are developed in [96].

The consideration of battery degradation costs in bidding and operating strategies in electricity markets is essential to ensure that the revenues obtained from the BESSs operation will at least cover their true operation and maintenance costs [97,98]. The most critical degradation factor concerns the BESS cycle depth, as most electrochemical batteries age nonlinearly to the cycle depth [98, 99]. To count BESS cycles and quantify the cumulative impact, the rainflow counting algorithm has

been widely used for battery life assessment [98,100]. However, the rainflow counting algorithm does not have an analytical mathematical expression and cannot be incorporated into optimization formulations [98]. Towards this direction, an approximate cycle-based degradation model that can be easily incorporated in optimization formulations is proposed in [98]. In [97,98], bidding strategies of BESSs participating in electricity markets are developed; however, these works do not consider the combined RES-BESS system. An operating strategy for a wind-BESS system considering battery degradation is presented in [101], but the bidding strategy in day-ahead electricity markets is not considered.

Day-ahead offering strategies of wind power producers using stochastic programming to consider RES generation, day-ahead price, and imbalance price uncertainties are proposed in [94, 102–104]; however, these works do not consider the usage of ESSs. Day-ahead trading strategies of combined wind generation and pumped-storage units are presented in [105, 106], but the expansion of pumped-storage units is limited due to environmental constraints. Offering and operating strategies are proposed in [107], but the day-ahead offering strategy is developed as a deterministic optimization problem; thus, the uncertainties in RES generation, day-ahead and imbalance prices are ignored. Day-ahead bidding strategies that handle the associated uncertainties are presented in [108,109]. However, none of the aforementioned bidding strategies for RES-BESS producers considers the BESS cycle degradation cost, which can reduce the producers' profit. In addition, power grid limits, due to transmission congestion, are not taken into account, which challenges the optimal energy scheduling of the RES-BESS system.

This chapter develops a bidding strategy for RES-BESS producers (e.g., wind-BESS and PV-BESS) to maximize their expected profits in electricity markets. The proposed strategy considers uncertainty in RES generation, as well as day-ahead and imbalance prices. BESS degradation and constraints on the allowable power exchange with the grid are also considered. Considering the power grid limits, the proposed scheme provides peak shaving services by making uncertainty-aware BESS decisions which reduce the real-operation RES power curtailments. To address the non-convexities associated with the BESS, a linear deterministic optimization scheme is developed that incorporates an approximate cycle-based degradation model and a relaxed BESS model. To handle uncertainties in RES power generation, day-ahead energy prices, and imbalance prices, a scenario-based linear stochastic

optimization scheme is developed that can be fast and reliably solved. Simulation results demonstrate the effectiveness of the proposed stochastic scheme in improving producers' profit compared to both the corresponding deterministic scheme and the base scenario, where the RES generation forecasting profile is directly submitted to the market.

The rest of this paper is organized as follows. Section 6.2 states the problem and Section 6.3 formulates the deterministic bidding strategy as a linear program. Section 6.4 formulates the two-stage scenario-based stochastic optimization scheme. The scenario selection methodology is explained in Section 6.5 and simulation results are presented in Section 6.6. Finally, conclusions are given in Section 6.7.

6.2 Problem statement

This section states the underlying problem by (a) describing the constraints of the RES-BESS plant, (b) presenting the cycle-based degradation model, (c) introducing the framework of the electricity markets under consideration, and (d) formulating the optimization problem of the bidding strategy considering the RES-BESS constraints, degradation model, and electicity market structure.

6.2.1 RES-BESS plant

We consider a BESS integrated in a RES plant (e.g., wind or PV plant), which is connected to the power grid. The arrows in Figure 6.1 indicate the possible power flow directions in a RES-BESS plant. Specifically, the power balance is defined as

$$P_t^r + P_t^d - P_t^c = P_t^g, \quad \forall t \in \mathcal{T}, \tag{6.1}$$

where $\mathcal{T} = \{1, ..., T\}$ denotes the considered time horizon. Variables $P_t^r \geq 0$, $P_t^d \geq 0$, $P_t^c \geq 0$, and P_t^g denote the RES power generation, BESS discharging power, BESS charging power, and buying (negative) or selling (positive) power into the power grid at time-step t in MW.

To avoid transmission congestion, the power exchange with the grid is restricted to

$$-\rho\overline{P}^r \leq P_t^g \leq \rho\overline{P}^r, \quad \forall t \in \mathcal{T}, \tag{6.2}$$

where constant $\overline{P}^r$ denotes the nominal capacity of the RES plant and ρ, $0 < \rho \leq 1$, defines the power grid limits. To ensure the power grid limits, the BESS can be

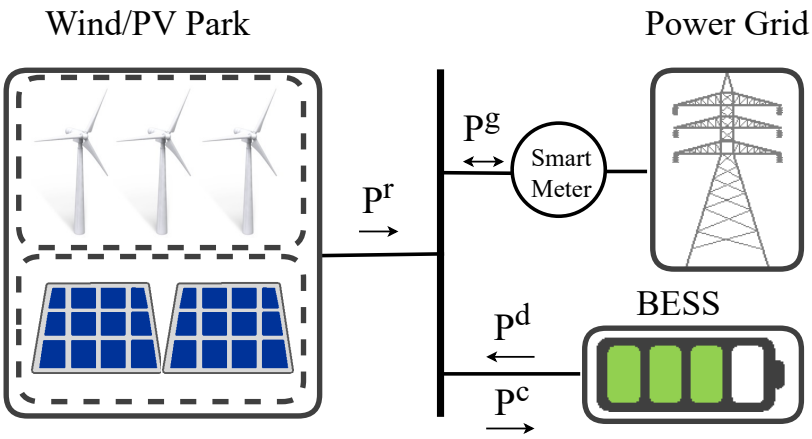

Figure 6.1: RES-BESS plant.

charged when the RES generation exceeds the grid limits; otherwise, RES power curtailments, P_t^u, must be applied, defined as

$$P_t^u = P_t^a - P_t^r, \quad 0 \leq P_t^r \leq P_t^a, \quad \forall t \in \mathcal{T}, \tag{6.3}$$

where constant P_t^a denotes the available RES generation at time-step t; P_t^a is usually replaced by the RES generation forecast. In (6.3), it is true that the RES generation $P_t^r < P_t^a$ when RES curtailments are applied, implying that $P_t^u > 0$.

Considering the widely-used piecewise linear power loss model presented in [27], the energy stored in the BESS is defined as

$$C_{t+1} = C_t + \Delta T(-P_t^d/\eta^d + \eta^c P_t^c), \quad \forall t \in \mathcal{T}, \tag{6.4}$$

where ΔT is the time-step duration in hours, η^c and η^d the charging and discharging efficiency coefficients, and C_t the energy stored in the BESS at time-step t in MWh. The charging and discharging power losses, l^c and l^d in %, are implicitly considered in (6.4) using the efficiency coefficients, such that $\eta^d = 1/(1 + l^d)$ and $\eta^c = 1 - l^c$. The BESS energy limits are set equal to

$$\underline{C} \leq C_t \leq \overline{C}, \quad \forall t \in \mathcal{T}, \tag{6.5a}$$

$$C_0 = I, \quad C_{T+1} \geq E^f, \tag{6.5b}$$

where constants $\underline{C}$ and $\overline{C}$ denote the minimum and maximum energy limits, and I and E^f the initial and final energy stored in the BESS over the considered time horizon, such that $\underline{C} \leq I \leq \overline{C}$ and $\underline{C} \leq E^f \leq \overline{C}$. The charging and discharging power limits are given by

$$0 \leq P_t^d \leq \overline{P}^d, \quad 0 \leq P_t^c \leq \overline{P}^c, \quad \forall t \in \mathcal{T}, \tag{6.6a}$$

$$P_t^d P_t^c = 0, \quad \forall t \in \mathcal{T}, \tag{6.6b}$$

where constants $\overline{P}^d$ and $\overline{P}^c$ denote the discharging and charging power limits. The non-convex constraint in (6.6b) ensures non-simultaneous charging and discharging.

6.2.2 BESS degradation

The cycle depth is a critical stress factor for BESS degradation which presents a nonlinear aging relationship with respect to the depth-of-discharge (DoD[1]) [99]. Specifically, cycles with higher DoD cause more severe damage to the battery. The DoD is associated with the state-of-charge (SoC) defined as

$$C_t^S = C_t / \hat{C}, \quad \forall t \in \mathcal{T}, \tag{6.7}$$

where variable C_t^S denotes the SoC of the BESS at time-step t and constant $\hat{C} \geq \overline{C}$ denotes the nominal BESS capacity in MWh. The rainflow cycle counting method is widely used to identify the BESS cycles for a given SoC profile [98,100]. Specifically, the main idea of the rainflow cycle method is to find the minimum and maximum values of the SoC profile, identify the half and full cycles, and calculate their DoD. For example, the SoC profile demonstrated in Figure 6.2 has one charging half cycle of 60% DoD (δ_1-δ_2), one full cycle of 40% DoD (δ_2-δ_4), and one discharging half cycle of 50% DoD (δ_4-δ_5). Let $\mathcal{J} = \{1, ..., J\}$ denotes the set of cycles for a given SoC profile, d_j the DoD of cycle $j \in \mathcal{J}$ in %, and $k_j = \{0.5, 1\}$ the length of cycle $j \in \mathcal{J}$, where $k_j = 0.5$ and $k_j = 1$ denote a half and full cycle, respectively. The rainflow algorithm for cycle identification is defined as

$$[\mathbf{k}, \mathbf{d}] = \texttt{Rainflow}(\mathbf{C}^S), \tag{6.8}$$

where $\mathbf{d}$ and $\mathbf{k}$ denote the vector forms of d_j and k_j, $\forall j \in \mathcal{J}$, while $\mathbf{C}^S$ the vector form of C_t^S, $\forall t \in \mathcal{T}$. Empirical non-linear DoD stress models are used to determine the degradation (also known as life loss) caused by one cycle of a BESS operating under a specific DoD [98,99]. A widely-used model is represented by the polynomial DoD stress function, $\Phi(d_j)$, given by

$$\Phi(d_j) = \gamma_1 d_j^{(\gamma_2)}, \tag{6.9}$$

[1]The DoD is defined as the ratio of the amount of energy that has been extracted from the battery in a cycle to its nominal capacity.

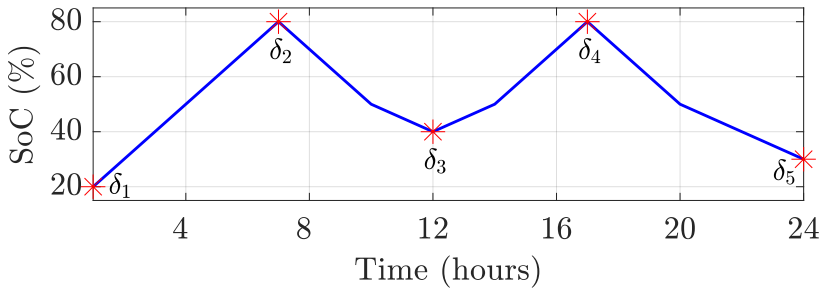

Figure 6.2: Identifying the BESS cycle depths for a given SoC profile. The SoC profile has one charging half cycle of 60% DoD (δ_1-δ_2), one full cycle of 40% DoD (δ_2-δ_4), and one discharging half cycle of 50% DoD (δ_4-δ_5).

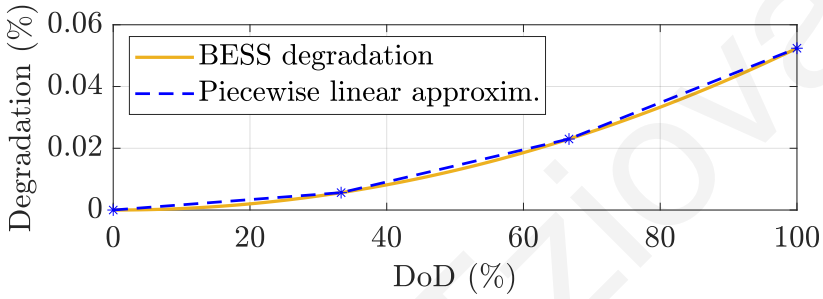

Figure 6.3: BESS degradation in % as a function of the DoD. The convex degradation function is approximated using N piece-wise linear segments.

where γ_1 and γ_2 denote the parameters of function $\Phi(d_j)$. For example, Figure 6.3 depicts the degradation using the polynomial DoD stress function, indicating that cycles with higher DoD cause more severe BESS degradation. For example, a 20% full cycle DoD causes 0.002% degradation, while a 60% full cycle DoD causes 0.019% degradation.

The total degradation, $L(\mathbf{C}^S)$, resulting from an SoC profile is calculated as the sum of the degradation caused by all the half and full cycles, defined as

$$L(\mathbf{C}^S) = \sum_{j \in \mathcal{J}} k_j \Phi(d_j). \tag{6.10}$$

The total degradation cost, $F^D(\mathbf{C}^S)$, is usually calculated as the product of the total degradation, $L(\mathbf{C}^S)$, and the battery replacement cost R [98], as

$$F^D(\mathbf{C}^S) = L(\mathbf{C}^S)R. \tag{6.11}$$

6.2.3 Electricity markets

The profits of RES-BESS producers can be maximized by trading energy in electricity markets. This work considers both the day-ahead (DA) and balancing markets.

Day-ahead market. The DA market concerns the entire day D and is cleared the day before, i.e. $D-1$. Figure 6.4(a) illustrates the hourly day-ahead prices, λ_t^D, obtained from the Spanish electricity market for the day 01/02/2022 [110]. The figure indicates that RES-BESS producers can benefit from energy arbitrage by buying and storing power during low-price periods and selling power during high-price periods. Since the actual DA prices are unknown when RES-BESS producers submit their bids to the DA market, producers can maximize their expected profits by making energy trading decisions based on predictions of the DA market prices and RES power generation.

Balancing market. Having a perfect next-day forecast for the RES power generation is unrealistic, due to the intermittent uncertain nature of these sources. As a result, any mismatch between day-ahead scheduled and actual power generation of the RES-BESS plant creates power imbalances during actual operation. These power imbalances can either cause excess or deficit of power in case of overproduction or underproduction of the RES-BESS plant, respectively. Considering the Spanish electricity market, the producer will be paid (charged) for its excess (deficit) of generation according to the imbalance prices of the balancing market. Figure 6.4(b) depicts the imbalance prices for power excess, λ_t^+, and power deficit, λ_t^-, for the day 01/02/2022. The figure indicates that $\lambda_t^+ \leq \lambda_t^D$ and $\lambda_t^- \geq \lambda_t^D$, $\forall t \in \mathcal{T}$. Therefore, the imbalance prices for excess and deficit of power can be linked with the day-ahead prices [94] as

$$r_t^+ = \frac{\lambda_t^+}{\lambda_t^D} \leq 1, \quad r_t^- = \frac{\lambda_t^-}{\lambda_t^D} \geq 1, \quad \forall t \in \mathcal{T}, \tag{6.12}$$

where r_t^+ and r_t^- denote the imbalance price ratio for excess and deficit of power, respectively. According to (6.12), overproduction is paid at a lower price compared to the DA price, while underproduction is charged at a higher price. This incentivizes RES-BESS producers to reduce their power imbalances to maximize their profits.

6.2.4 Bidding strategy

The bidding strategy aims to maximize the expected profits of RES-BESS producers by determining the power exchange with the grid through the day-ahead energy scheduling of the RES-BESS plant. The outcome of the bidding strategy is the power

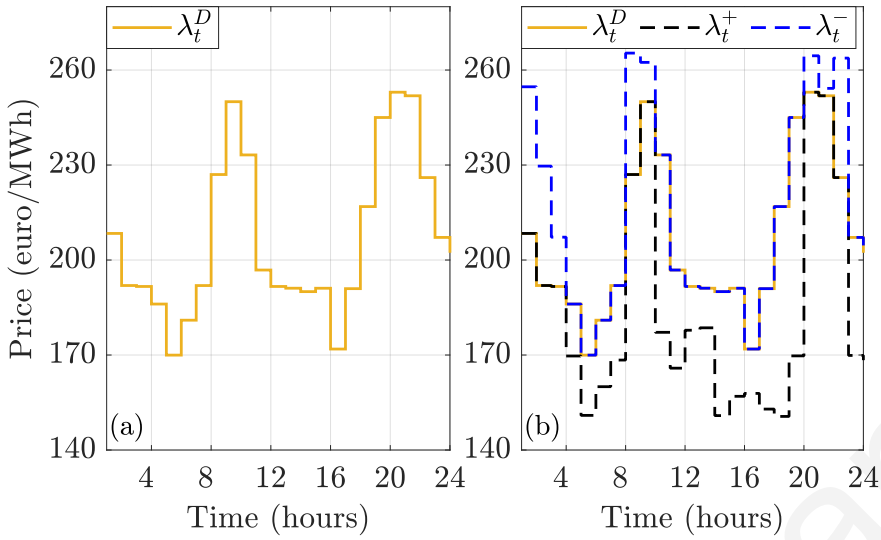

Figure 6.4: Prices from the Spanish electricity market for 01/02/2022: (a) day-ahead electricity prices and (b) imbalance prices of the balancing market.

exchange with the grid submitted to the DA market. This work considers *price-taker*[2] *producers*.

Assuming perfect knowledge of the RES generation, P_t^q, and day-ahead electricity prices, λ_t^D, any power imbalances are eliminated and the balancing market can be ignored. Under this assumption, the bidding strategy is formulated as a deterministic optimization problem that maximizes (minimizes) the revenues (costs) of selling (buying) energy in the DA market and minimizes the BESS degradation cost, while satisfying the dynamics and physical constraints of the RES-BESS plant, as

$$\text{maximize} \quad \Delta T \sum_{t \in \mathcal{T}} \lambda_t^D P_t^g - F^D(\mathbf{C}^S), \tag{6.13a}$$

$$\text{subject to:} \quad (6.1) - (6.8). \tag{6.13b}$$

Problem (6.13) is challenging to solve for three reasons:

1. *Non-convex BESS power loss model*. The complementarity constraint (6.6b) of the BESS power loss model is non-convex as it involves a product of variables.

2. *Rainflow algorithm*. Although the polynomial DoD stress model in (6.9) is convex, the rainflow counting algorithm (6.8) does not have an analytical mathematical expression and cannot be incorporated into an optimization formulation [98].

[2] A price-taker producer has no capability of altering market-clearing prices and takes the prevailing market prices (see [25], Section 7.3).

3. *Parametric Uncertainty*. Assuming perfect knowledge of RES generation and day-ahead electricity prices for the next day is unrealistic; thus, the actual RES generation, P_t^a, and DA prices, λ_t^D, are uncertain. Nonetheless, having uncertainty in RES generation implies that the balancing market should also be considered in the bidding strategy which implies that the imbalance ratios r_t^+ and r_t^- should also be treated as uncertain.

In the next section, we develop a linear deterministic optimization formulation to deal with the non-convexities arising from the first two challenges, while in Section 6.4 we develop a scenario-based stochastic optimization bidding strategy to handle the aforementioned uncertainties.

6.3 Deterministic Bidding Strategy

This section formulates the deterministic bidding strategy as a linear program, which can be fast and reliably solved, by incorporating an approximate BESS degradation model and using a relaxed power loss model.

6.3.1 Relaxed Power Loss Model

Constraints (6.6a)-(6.6b) of the non-convex power loss model can be reformulated using binary variables, yielding

$$0 \leq P_t^d \leq (1 - b_t)\overline{P}^d, \quad 0 \leq P_t^c \leq b_t\overline{P}^c, \quad \forall t \in \mathcal{T}, \tag{6.14a}$$

$$b_t \in \{0, 1\}, \quad \forall t \in \mathcal{T}, \tag{6.14b}$$

where binary variable b_t is used in (6.14a) to ensure non-simultaneous charging and discharging. The relaxed model is derived by relaxing b_t to take continuous values, i.e.

$$b_t \in [0, 1], \quad \forall t \in \mathcal{T}. \tag{6.15}$$

The relaxed model, i.e. constraints (6.4)-(6.5b), (6.14a), and (6.15), can be used to formulate convex optimization problems. This model is exact, generating the optimal solution, when charging and discharging do not simultaneously occur. In the proposed bidding strategy, the maximization of the producer profit is an incentive to satisfy the relaxation exactness, because increased BESS power losses that reduce

the producer profit result from the optimization problem when the relaxation is not exact.

6.3.2 Approximate BESS Degradation Model

To deal with the rainflow counting algorithm (6.8), which cannot be incorporated in a convex mathematical program, we utilize the approximate degradation model proposed in [98]. This model eliminates the rainflow counting algorithm by assuming that degradation only occurs during the discharging period of the BESS, such that one discharging half cycle is counted as one full cycle of the same DoD. Thus, the charging half cycles are ignored. Considering the aforementioned assumption, the approximate model may yield different solutions compared to the rainflow algorithm when the initial SoC differs from the final SoC. For example, considering the SoC profile shown in Figure 6.2, the total degradation using the approximate model is equal to $L(\mathbf{C}^S) = \Phi(40\%) + \Phi(50\%)$, while the total degradation calculated using the rainflow algorithm is equal to $L(\mathbf{C}^S) = \Phi(40\%) + 0.5\Phi(50\%) + 0.5\Phi(60\%)$. However, the approximate model can be integrated in convex optimization problems and yields high quality approximate solutions when we consider the daily BESS operation in electricity markets [98]. Next, the formulation of the approximate model is described.

Degradation Cost Function. The convex DoD stress function, $\Phi(d_j)$, is approximated using a piecewise linear function with $\mathcal{N} = \{1, ..., N\}$ linear segments, as shown in Figure 6.3 with $N = 3$. The degradation cost function of the approximate model is defined as

$$F^A(\mathbf{P}^{d,A}) = \Delta T \sum_{t=1}^{T} \sum_{n=1}^{N} c_n^A P_{t,n}^{d,A}, \tag{6.16}$$

where variable $P_{t,n}^{d,A} \geq 0$ denotes the BESS discharging power for time-step $t \in \mathcal{T}$ and linear segment $n \in \mathcal{N}$, $\mathbf{P}^{d,A}$ the vector form of $P_{t,n}^{d,A}$, $\forall t \in \mathcal{T}$, $n \in \mathcal{N}$, and constant c_n^A the degradation cost associated with DoD segment $n \in \mathcal{N}$. Constant c_n^A is calculated for each segment $n \in \mathcal{N}$ using the degradation function $\Phi(d_j)$, replacement cost R, discharging efficiency η^d, and BESS capacity $\hat{C}$ [98], as

$$c_n^A = \frac{R}{\eta^d \hat{C}} N \left(\Phi\left(\frac{n}{N}\right) - \Phi\left(\frac{n-1}{N}\right) \right). \tag{6.17}$$

Constraints. Considering the set of linear segments $\mathcal{N}$, the approximate model

reformulates constraint (6.4) as

$$C^A_{t+1,n} = C^A_{t,n} + \Delta T(-P^{d,A}_{t,n}/\eta^d + \eta^c P^{c,A}_{t,n}), \quad \forall t \in \mathcal{T}, n \in \mathcal{N}, \tag{6.18}$$

where variables $P^{c,A}_{t,n} \geq 0$, and $C^A_{t,n} \geq 0$ denote the charging power and energy stored in the BESS for each time interval $t \in \mathcal{T}$ and DoD segment $n \in \mathcal{N}$. The energy limit of each DoD segment is set as

$$C^A_{t,n} \leq \overline{C}^A_n, \quad \forall t \in \mathcal{T}, n \in \mathcal{N}, \tag{6.19a}$$

$$C^A_{1,n} = I^A_n, \quad \forall n \in \mathcal{N}, \tag{6.19b}$$

where constants $\overline{C}^A_n$ and I^A_n denote the maximum and initial energy stored in the BESS in segment n, respectively. Considering that all DoD segments have the same energy limits, then it is true that $\overline{C}^A_n = \hat{C}/N$, $\forall n \in \mathcal{N}$. The total discharging/charging power and energy stored in the BESS at time t are equal to

$$P^d_t = \sum_{n \in \mathcal{N}} P^{d,A}_{t,n}, \quad P^c_t = \sum_{n \in \mathcal{N}} P^{c,A}_{t,n}, \qquad \forall t \in \mathcal{T}, \tag{6.20a}$$

$$C_t = \sum_{n \in \mathcal{N}} C^A_{t,n}, \quad \underline{C} \leq C_t \leq \overline{C}, \qquad \forall t \in \mathcal{T}. \tag{6.20b}$$

The constraints presented in (6.5b), (6.14a)-(6.14b) are also included in the model. Since the degradation cost function is convex monotonically increasing, it is true that $c^A_n \leq c^A_{n+1}$. This implies that the BESS always discharges from the DoD segments with the lower degradation cost to the segments with higher cost.

6.3.3 Mathematical Formulation

The deterministic optimization problem (6.13) is reformulated to consider the approximate BESS degradation model and relaxed power loss model. In addition, the actual RES generation P^a_t and day-ahead prices λ^D_t, which are unknown, are replaced by their predicted values $\hat{P}^a_t$ and $\hat{\lambda}^D_t$, respectively, such that $\hat{P}^a_t$ is used in (6.3) instead of P^a_t. The considered problem, defined as Problem $\mathcal{P}^D$, is formulated as

$$\mathcal{P}^D : \begin{cases} \text{maximize} & \Delta T \sum_{t \in \mathcal{T}} \left(\hat{\lambda}^D_t P^g_t - F^A(\mathbf{P}^{d,A}) \right) \\ \text{subject to} & (6.1) - (6.3), (6.5b), (6.14a), (6.15), (6.18) - (6.20b). \end{cases}$$

Problem $\mathcal{P}^D$ is a linear program.

6.4 Stochastic Bidding Strategy

This section builds on the formulation of the deterministic bidding strategy of Section 6.3 to develop a two-stage scenario-based stochastic optimization scheme to deal with uncertainties in RES generation, day-ahead prices, and imbalance ratio. This work uses scenario curves to characterize each uncertainty source, where a scenario curve represents one possible realization of the corresponding uncertainty source, e.g., RES generation, for the next day. The proposed scenario-based stochastic scheme involves two stages of decision-making. Specifically, decisions are made in the day-ahead market (first stage) considering possible scenarios of the balancing market (second stage). The first-stage decision variables are associated with the power exchange with the grid, P_t^g, $\forall t \in \mathcal{T}$, which is submitted to the day-ahead market. The second-stage decision variables are related with the power imbalances, which are defined by the scenarios.

6.4.1 Objective Function

We consider the set of scenarios $\mathcal{S} = \{1, ..., S\}$ with $S = |\mathcal{S}|$; each scenario concerns the RES power generation, day-ahead prices, and imbalance ratios of the considered horizon $\mathcal{T}$. Let variables $P_{t,s}^+ \geq 0$ and $P_{t,s}^- \geq 0$ denote the imbalance power for excess and deficit of power at time-step t of scenario s, respectively. The objective of the stochastic optimization scheme is to maximize the producer profit by maximizing the expected market profit, $\mathbb{E}[F(\mathbf{P}^g, \mathbf{P}^+, \mathbf{P}^-)]$, and minimizing the BESS degradation cost, $F^A(\mathbf{P}^{d,A})$, yielding

$$\text{maximize} \quad \mathbb{E}[F(\mathbf{P}^g, \mathbf{P}^+, \mathbf{P}^-)] - F^A(\mathbf{P}^{d,A}), \tag{6.21}$$

where $\mathbf{P}^g$, $\mathbf{P}^+$, and $\mathbf{P}^-$ are the vector-forms of variables P_t^g, $P_{t,s}^+$, and $P_{t,s}^-$, $\forall t \in \mathcal{T}, s \in \mathcal{S}$. The expected market profit is defined as the weighted-average profit[3] of the producer obtained from the day-ahead and balancing markets across all scenarios

$$\mathbb{E}[F(\mathbf{P}^g, \mathbf{P}^+, \mathbf{P}^-)] = \Delta T \sum_{s \in \mathcal{S}} \phi_s \Big(\sum_{t \in \mathcal{T}} \Big(\tilde{\lambda}_{t,s}^D P_t^g + \tilde{r}_{t,s}^+ \tilde{\lambda}_{t,s}^D P_{t,s}^+ - \tilde{r}_{t,s}^- \tilde{\lambda}_{t,s}^D P_{t,s}^- \Big) \Big), \tag{6.22}$$

where constants $\tilde{\lambda}_{t,s}^D$, $\tilde{r}_{t,s}^+$, and $\tilde{r}_{t,s}^-$ denote the day-ahead prices and imbalance price ratios for excess and deficit of power at time-step t of scenario s, respectively; ϕ_s is

[3]The market profits are defined as the market revenues minus the costs.

the weighting parameter of scenario s such that $\sum_{s\in\mathcal{S}} \phi_s = 1$. Note that the scenario selection process is explained in Section 6.5.

6.4.2 Constraints

First-Stage Constraints. The constraints of the day-ahead stage, which are scenario independent, are associated with the constraints of the deterministic bidding strategy, given by

$$\text{Constraints:} \quad (6.1), (6.5b), (6.14a), (6.15), (6.18) - (6.20b). \tag{6.23}$$

The RES power generation, P_t^r, is limited by the nominal capacity of the RES plant, $\overline{P}^r$, defined as

$$0 \leq P_t^r \leq \overline{P}^r, \quad \forall t \in \mathcal{T}. \tag{6.24}$$

In the stochastic optimization scheme, the produced power $P_t^r, \forall t \in \mathcal{T}$ is a first-stage variable defined by the RES power production profiles of the selected scenarios.

Second-Stage Constraints. The constraints of the power grid limits in (6.2) are reformulated to consider the power imbalances for power excess, $P_{t,s}^+$, and deficit, $P_{t,s}^-$, in scenario s as

$$P_t^g + P_{t,s}^+ \leq \rho\overline{P}^r, \quad \forall t \in \mathcal{T}, s \in \mathcal{S}, \tag{6.25a}$$

$$-\rho\overline{P}^r \leq P_t^g - P_{t,s}^-, \quad \forall t \in \mathcal{T}, s \in \mathcal{S}. \tag{6.25b}$$

Constraints (6.25a) and (6.25b) ensure the direct and reverse power flow limits, respectively. Any overproduction or underproduction of the RES power generation needs to be compensated to ensure power balance. Let constant $\tilde{P}_{t,s}^r$ denote the RES power generation at time t of scenario s. Then, the difference between the RES generation of scenario s and the scheduled RES generation at time t, $(\tilde{P}_{t,s}^r - P_t^r)$, denotes the RES overproduction (positive) or underproduction (negative). When $(\tilde{P}_{t,s}^r - P_t^r) > 0$ the RES overproduction creates excess of power, $P_{t,s}^+$, that will be paid, except of the cases where the grid power limits in (6.25a) are violated and RES power curtailments, $\hat{P}_{t,s}^u$, must be applied. Similarly, when $(\tilde{P}_{t,s}^r - P_t^r) < 0$ the RES underproduction creates deficit of power, $P_{t,s}^-$, that will be charged. These conditions yield

$$(\tilde{P}_{t,s}^r - P_t^r) = P_{t,s}^+ - P_{t,s}^- + \hat{P}_{t,s}^u, \quad \forall t \in \mathcal{T}, s \in \mathcal{S}. \tag{6.26}$$

Note that the BESS power set-points are first-stage decisions that can adjust the scheduled grid power, P_t^g, through (6.1) to reduce the RES power curtailments, $\hat{P}_{t,s}^u$, in (6.26). It is important to note that non-convex constraints that ensure non-simultaneous excess and deficit of power can be avoided [94], because the expected market profit in (6.22) is maximized when $P_{t,s}^-$ is minimized, implying that $P_{t,s}^+ P_{t,s}^- = 0$ when $\tilde{r}_{t,s}^+ < \tilde{r}_{t,s}^-$, $\forall t \in \mathcal{T}, s \in \mathcal{S}$.

The optimization problem of the stochastic bidding strategy, defined as Problem $\mathcal{P}^S$, is summarized as

$$\mathcal{P}^S : \begin{cases} \text{maximize} & (6.21) \\ \text{subject to} & (6.23) - (6.26). \end{cases}$$

Problem $\mathcal{P}^S$ is a linear program that can be fast and reliably solved under a large number of scenarios.

6.5 Scenario selection

This section explains the methodology used to select scenario curves for the RES power generation (whether it is from PV or wind), day-ahead prices, and imbalance ratios. This work selects the scenario curves for each uncertainty source based on historical data, using two different methodologies.

Methodology 1. The first methodology assumes that forecasting data for the next day are available for the considered uncertainty source, e.g., for the wind power generation. This method selects a subset of the historical curves which are closest to the day-ahead forecasted curve. Towards this direction, we utilize the Euclidean distance between a historical and the forecasted curve, given by [111]

$$y_k(\mathbf{W}, \mathbf{A}_k) = \sqrt{\sum_{t \in \mathcal{T}} (W_t - A_{t,k})^2}, \quad k \in \mathcal{K}, \tag{6.27}$$

where $\mathbf{W}$ is the time series vector of the forecasted curve, $\mathbf{A}_k$, $\forall k \in \mathcal{K}$ is the time series vector of the kth historical actual curves, and $\mathcal{K}$ is the corresponding set. Then, the set of selected curves $\mathcal{G} = \{1, ..., G\}$ is formed by the $G - 1$ curves with the smallest Euclidean distance and the forecasted curve. The weights of the selected curves are weighted according to an importance factor $f_g^G \in [0, 1]$, $\forall g \in \mathcal{G}$ that aims to put more importance on curves with small Euclidean distance. Factor f_g^G is defined as

$$f_g^G = 1 - \frac{y_g(\mathbf{W}, \mathbf{A}_g)}{y^{max}}, \quad g \in \mathcal{G}, \tag{6.28}$$

where $y^{max} = \max_{k \in \mathcal{K}}\{y_k(\mathbf{W}, \mathbf{A}_k)\}$. Note that the importance factor of the forecasted curve $\mathbf{W}$ is equal to one because the corresponding Euclidean distance is equal to zero. Normalizing the importance factors yields the weights of the selected curves ϕ_g^G, defined as

$$\phi_g^G = f_g^G / \sum_{i \in \mathcal{G}} f_i^G, \quad g \in \mathcal{G}. \tag{6.29}$$

Methodology 2. The second methodology assumes that forecasting data for the next day are unavailable for the considered uncertainty source. Thus, only historical data of the previous days are used to form the scenarios. Let day D denote the current day and $D+1$ the day ahead where we aim to determine the scheduled grid power, $P_t^g \ \forall t \in \mathcal{T}$, submitted to the day-ahead market. We assume that the decisions are made at the end of day D, enabling the use of the actual curve of this day. Then, the set of selected curves $\mathcal{G} = \{D - G + 1, ..., D\}$ is formed by the historical curves of the last G days. The importance factor $\mathbf{f}^G = [1/G, 2/G, ..., G/G]$ is introduced, aiming to assign an increasing importance on daily profiles closer to day D. Similarly with the first methodology, the weights of the selected curves are defined using (6.29), where f_g^G is the g element of vector $\mathbf{f}^G$.

Using either the first or second methodology, depending on the availability of forecasting data, we select

- V RES generation curves with weights ϕ_v^V, $v = 1, ..., V$.
- M day-ahead price curves with weights ϕ_m^M, $m = 1, ..., M$.
- Q imbalance ratio curves with weights ϕ_q^Q, $q = 1, ..., Q$.

There are various sophisticated methodologies available in the literature for generating scenarios, such us seasonal ARIMA and second-order autoregressive models for generating price and wind generation scenarios [25, 94]. However, the accurate characterization of the considered uncertainties is out of the scope of this work. Similarly with [94], any correlations among market prices and RES generation are ignored in this work. Therefore, we deal with the three source of uncertainty by building the symmetric scenario tree presented in Figure 6.5. Specifically, each scenario $s \in \mathcal{S}$ represents a combination of a single RES generation, day-ahead price, and imbalance ratio curve with weight $\phi_s = \phi_v^V \cdot \phi_m^M \cdot \phi_q^Q$. Thus, the total number of scenarios is $S = V \cdot M \cdot Q$.

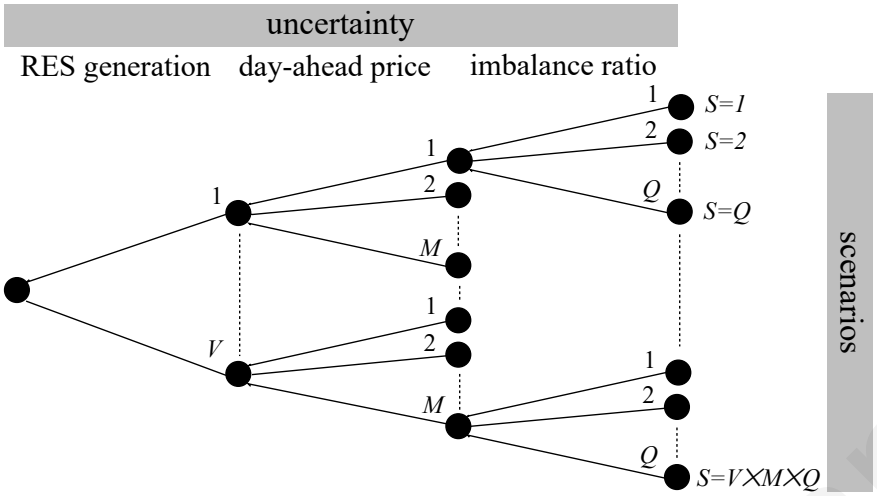

Figure 6.5: The scenario tree considering the RES power generation, day-ahead price, and imbalance ratio curves.

In the deterministic scheme, Problem $\mathcal{P}^D$, the prediction data used depends on the availability of forecasting data for each uncertainty source. Specifically, either the forecasted curve or the historical curve of the previous day D is used as the predicted curve.

6.6 Simulation results

This section evaluates the performance of the proposed stochastic bidding strategy considering both PV-BESS and wind-BESS producers. The performance of the deterministic and stochastic optimization schemes, Problems $\mathcal{P}^D$ and $\mathcal{P}^S$, in terms of actual producer profits[4] is compared with the solution of the following problems:

- **Problem $\mathcal{P}^B$**: The base case where the BESS is ignored and the predicted RES power generation, $\hat{P}^a_t$, $\forall t \in \mathcal{T}$, is submitted to the day-ahead market.
- **Problem $\mathcal{P}^I$**: The ideal case where the actual RES power generation, P^a_t, and day-ahead prices, λ^D_t, are used in $\mathcal{P}^D$. Although Problem $\mathcal{P}^I$ is unrealizable as it assumes knowledge of future information, it is used for comparison purposes as it provides the optimal performance.

[4]The actual producer profits are calculated using the optimization decisions of the RES-BESS plant and the actual RES generation, day-ahead prices, and imbalance ratios. Specifically, the market profits are calculated using the scheduled grid power, while the BESS degradation cost is calculated by applying the BESS decisions in the Rainflow algorithm.

All problems are coded in Matlab and solved using optimization solver Gurobi [43] on a personal computer with 16 GB RAM and an Intel Core-i7 2.11 GHz processor. The horizon is set to one day with 30-minute time intervals. The scenarios in Problem $\mathcal{P}^S$ are constructed by selecting 15 curves for RES power generation ($V = 15$) and 10 curves for day-ahead price and imbalance ratio curves ($M = 10$ and $Q = 10$), yielding $S = 1500$ scenarios. All the day-ahead and imbalance price curves are obtained from the Spanish electricity market [110]. This work considers the polynomial DoD stress function in (6.9), where $\gamma_1 = 5.24 \times 10^{-4}$, $\gamma_2 = 2.03$ [98] and $N = 50$ piecewise linear segments. The battery replacement cost is set equal to 100000 €/MWh, such that $R = 100000 \times \hat{C}$ €.

6.6.1 Wind-BESS producer

Setup. The performance of the proposed stochastic scheme is evaluated using real data from a 10.8 MW ($\overline{P}^r = 10.8$ MW) wind power plant located in Larnaca, Cyprus. The proposed scheme is examined under power grid limits due to transmission congestion, setting $\rho = 0.875$. We consider an integrated BESS with capacity of 10 MWh ($\hat{C} = 10$ MWh), charging/discharging power of 10 MW ($\overline{P}^c = \overline{P}^d = 10$ MW) and one-way efficiency of 96% ($\eta^d = \eta^c = 0.96$). Moreover, minimum and maximum energy limits of 1.5 and 9.5 MWh ($\underline{C} = 0.15\hat{C}$ and $\overline{C} = 0.95\hat{C}$ MWh) are set to protect the BESS from over-discharge and over-charge. The initial and final energy stored in the BESS is set to 2 MWh ($I = E^f = 0.2\hat{C}$). Since forecasting data for the wind generation are available and provided from the real wind plant, the corresponding scenario curves are selected using Methodology 1 described in Section 6.5. The scenario curves for the day-ahead energy prices and imbalance ratios are selected according to Methodology 2 because forecasting data are unavailable.

Performance evaluation. The performance of the proposed stochastic scheme $\mathcal{P}^S$ is evaluated and compared with the deterministic scheme $\mathcal{P}^D$ for the day 04/03/2022. Fig. 6.6 depicts the real curves of the wind power generation, day-ahead prices, and imbalance ratios used in the two schemes. Specifically, the predicted and scenario curves are used as input in $\mathcal{P}^S$, while only the predicted curves are used in $\mathcal{P}^D$. Moreover, the actual curves are used for evaluation.

Ignoring the BESS degradation model in Problems $\mathcal{P}^S$ and $\mathcal{P}^D$, Figures 6.7(a)-(d) and 6.7(e)-(h) illustrate the scheduled day-ahead decisions of the wind-BESS plant

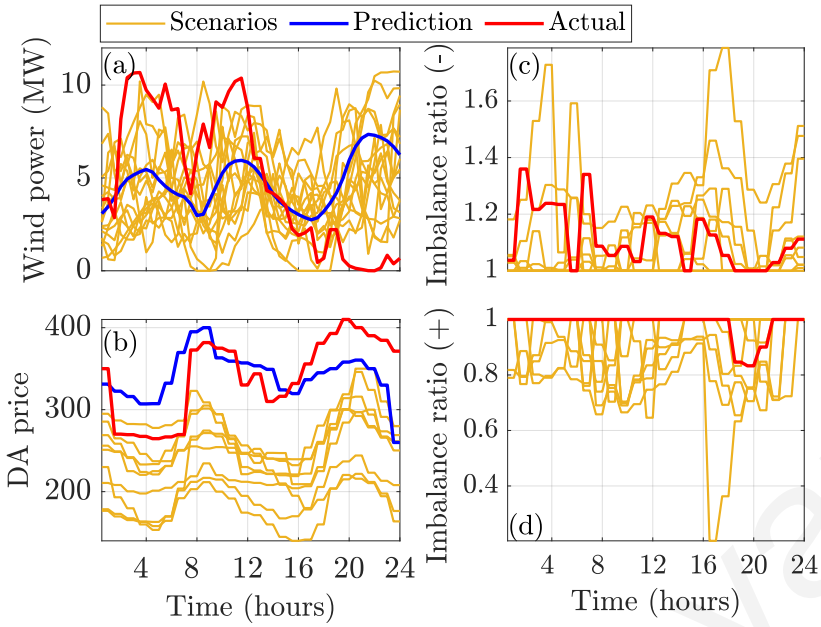

Figure 6.6: The predicted, actual, and scenario curves used for the performance evaluation of Problems $\mathcal{P}^S$ and $\mathcal{P}^D$ for 04/03/2022: (a) wind power generation (MW), (b) day-ahead prices (€/MWh), (c) imbalance ratio for power deficit, and (d) imbalance ratio for power excess.

as well as the actual system operation using $\mathcal{P}^D$ and $\mathcal{P}^S$, respectively. As expected, Figure 6.7(a) shows that the scheduled wind power follows the predicted curve in $\mathcal{P}^D$, while Figure 6.7(e) indicates that the scheduled wind power deviates from the predicted curve due to the impact of the scenarios in $\mathcal{P}^S$. Figures 6.7(b) and 6.7(f) demonstrate the scheduled grid power based on the scheduled wind power and the decisions of the BESS power set-points presented in Figures 6.7(c) and 6.7(g). The energy stored in the BESS based on the BESS power set-points is depicted in Figures 6.7(d) and 6.7(h). As shown in Figures 6.7(d) and 6.7(h), two full cycles of almost 80% DoD are presented in both Problems $\mathcal{P}^D$ and $\mathcal{P}^S$ because the BESS degradation is ignored. However, this BESS operation causes a severe BESS degradation, resulting in 0.0646% and 0.0667% degradation and 646.4€ and 667.4€ degradation cost using $\mathcal{P}^D$ and $\mathcal{P}^S$, respectively. As expected, the uncertainty-aware decisions of Problem $\mathcal{P}^S$ increase the actual producer profit by 2.34% compared to $\mathcal{P}^D$, where the daily profits using $\mathcal{P}^D$ and $\mathcal{P}^S$ are 35294.3€ and 36120.9€, respectively.

Considering the BESS degradation model, Figures 6.8(a)-(c) and 6.8(d)-(f) illustrate the scheduled and actual grid power, as well as the BESS power and energy decisions using Problems $\mathcal{P}^D$ and $\mathcal{P}^S$, respectively. To ensure the power grid limits in actual operation of the wind-BESS plant, wind energy curtailments[5] of 6.08 MWh

[5]We consider that RES power curtailments are applied in real operation to maintain the actual

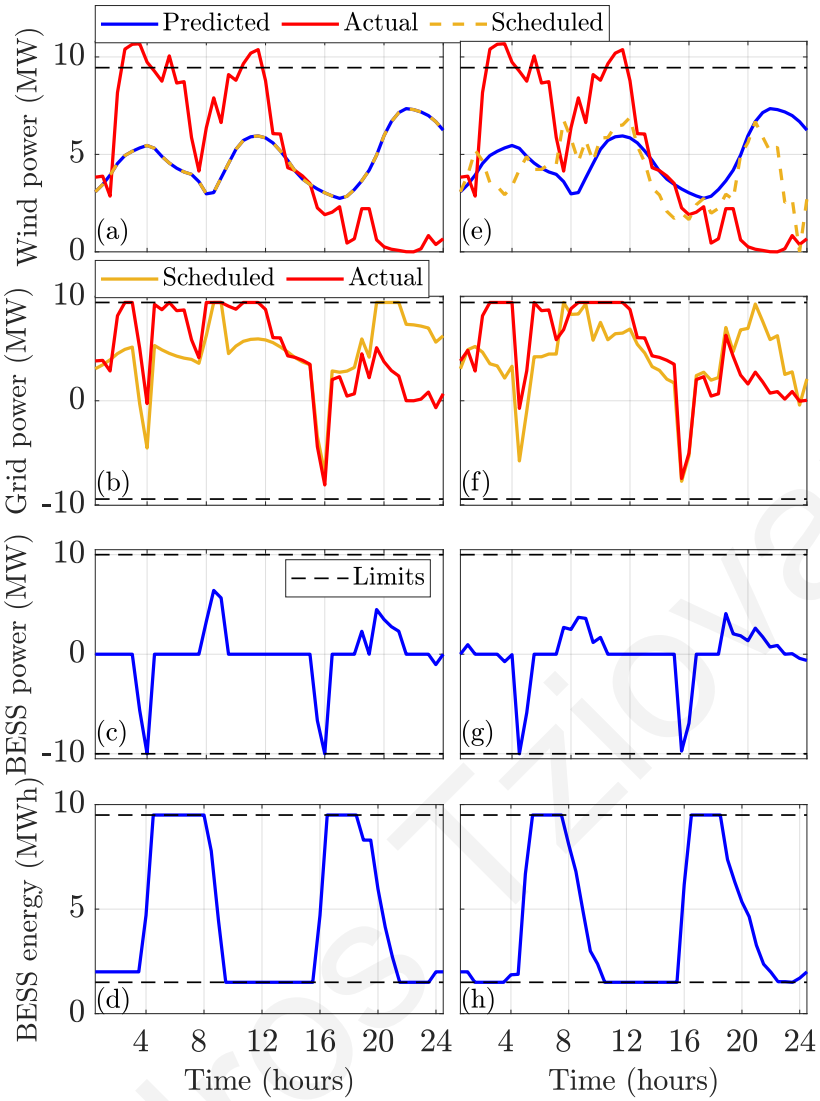

Figure 6.7: The scheduled day-ahead decisions of the wind-BESS plant as well as the actual system operation using Problems $\mathcal{P}^D$ (a)-(d) and $\mathcal{P}^S$ (e)-(h) when the BESS degradation is ignored in both optimization problems.

and 2.92 MWh are applied in $\mathcal{P}^D$ and $\mathcal{P}^S$, respectively. As expected, the uncertainty-aware decisions of Problem $\mathcal{P}^S$ reduce the wind curtailments by 51.97%. As shown in Figures 6.8(c) and 6.8(f), both $\mathcal{P}^D$ and $\mathcal{P}^S$ avoid to fully charge the BESS, reducing the degradation from 0.0646% and 0.0667% to 0.0193% and 0.0090% compared to the BESS operation presented in Figures 6.7(d) and 6.7(h). Therefore, the degradation cost in Problems $\mathcal{P}^D$ and $\mathcal{P}^S$ reduces from 646.4€ and 667.4€ to 193.3€ and 90€, respectively. Reducing the degradation cost, the actual producer profit in $\mathcal{P}^D$ and $\mathcal{P}^S$ increases from 35294.3€ and 36120.9€ to 35389.8€ and 36931.5€, respectively. Considering BESS degradation, Problem $\mathcal{P}^S$ increases the producer profit from 2.34%

grid power between its limits.

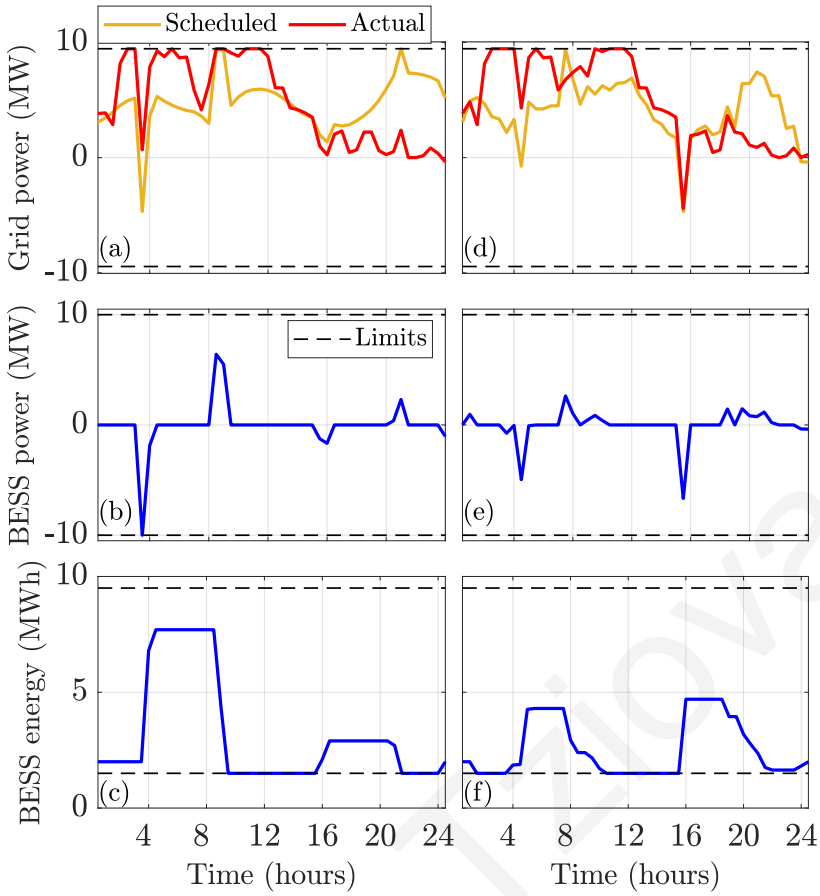

Figure 6.8: The scheduled day-ahead decisions and actual operation of the wind-BESS plant using Problems $\mathcal{P}^D$ (a)-(c) and $\mathcal{P}^S$ (d)-(f) when the BESS degradation is considered in both optimization problems.

to 4.35% compared to $\mathcal{P}^D$.

The approximate degradation model yields degradation costs of 208.2€ and 88.1€ for $\mathcal{P}^D$ and $\mathcal{P}^S$, respectively. These degradation costs are similar to the costs calculated using the Rainflow algorithm (193.3€ and 90€), indicating that the approximate degradation model yields high quality approximate solutions for the proposed bidding strategy.

The execution times of $\mathcal{P}^D$ and $\mathcal{P}^S$ are 0.08 and 14.7 seconds when the BESS degradation model is used, indicating the increased complexity of Problem $\mathcal{P}^S$ compared to $\mathcal{P}^D$. However, Problem $\mathcal{P}^S$ presents a small execution time despite the consideration of a large number of scenarios ($S = 1500$).

Aggregate performance evaluation. The proposed stochastic scheme, Problem $\mathcal{P}^S$, is evaluated and compared with Problems $\mathcal{P}^B$, $\mathcal{P}^D$, and $\mathcal{P}^I$ for each day of the period 01/02/2022-30/09/2022. Table 6.1 presents the total producer profits and wind power curtailments for the entire period using the considered problems. Interestingly, the

Table 6.1: Total actual producer profits and wind curtailments for the period 01/02/2022-30/09/2022 using the different problems.

Problem	Profit (€)	Profit increment (%)	wind curtailments (MWh)
$\mathcal{P}^B$	2,677,715		332.5
$\mathcal{P}^D$	2,693,783	0.6	569.6
$\mathcal{P}^S$	2,835,448	5.9	373.7
$\mathcal{P}^I$	3,190,269	19.1	58.0

actual wind power curtailments using Problems $\mathcal{P}^D$ and $\mathcal{P}^S$ are higher compared to $\mathcal{P}^B$, where the BESS is not utilized. This is because Problems $\mathcal{P}^D$ and $\mathcal{P}^S$ operate the wind-BESS system closer to the power grid limits to maximize profits through energy storage arbitrage. As a result, wind curtailments occur more frequently in real operation to ensure the grid limits when high forecasting errors occur. Although both Problems $\mathcal{P}^D$ and $\mathcal{P}^S$ increase wind curtailments, they also increase the total profit by 0.6% and 5.9%, respectively, compared to $\mathcal{P}^B$. The Table also indicates the superiority of Problem $\mathcal{P}^S$ to achieve higher profits compared to $\mathcal{P}^D$, increasing the total profit by 141,665 €. Note that by employing an operating strategy along with the bidding strategy can lead to a significant reduction in actual wind curtailments, resulting in further improvement in the producer profit. Although Problem $\mathcal{P}^I$ assumes perfect knowledge of the wind power generation, wind power curtailments of 58 MWh are applied because the BESS capacity is insufficient to always ensure the power grid limits. Problem $\mathcal{P}^I$ increases the total profit by 19.1% as it provides the optimal performance; however, Problem $\mathcal{P}^I$ is unrealizable. Figures 6.6(a) and 6.6(c)-(d) indicate that the representative scenarios capture the actual curves well; however, this is not the case for the day-ahead prices (see Figure 6.6(c)) because by using the historical curves of the previous days as scenarios does not always represent uncertainty well. Thus, by selecting the scenarios in a more sophisticated way can further enhance the performance of Problem $\mathcal{P}^S$.

6.6.2 PV-BESS producer

Setup. To emulate the PV power plant, we use real data from a residential PV system with an installed capacity of 5.58 KW and we upscale its power generation to consider a 10.8 MW PV plant ($\overline{P}^r$ = 10.8 MW). We set stricter power grid limits

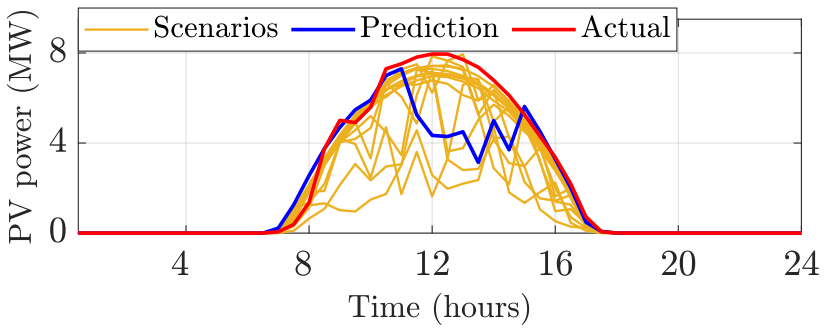

Figure 6.9: The scenario, predicted, and actual PV curves used for the performance evaluation of Problems $\mathcal{P}^S$ and $\mathcal{P}^D$ for 04/03/2022.

for the PV producer compared to the wind producer, reducing ρ from 0.875 to 0.6. Morever, we consider an integrated BESS with capacity of 5 MWh ($\hat{C}$ = 5 MWh), charging/discharging power of 5 MW ($\overline{P}^c = \overline{P}^d$ = 5 MW) and one-way efficiency of 96% ($\eta^d = \eta^c$ = 0.96). Similarly with the setup of the wind producer, we set $I = E^f = 0.2\hat{C}$, $\underline{C} = 0.15\hat{C}$, and $\overline{C} = 0.95\hat{C}$. Since forecasting data are unavailable, the scenario curves for the PV generation, day-ahead energy prices and imbalance ratios are selected using Methodology 2 described in Section 6.5.

Performance evaluation. The performance of Problem $\mathcal{P}^S$ is evaluated and compared with $\mathcal{P}^D$ for the day 04/03/2022. Figures 6.9 and 6.6(b)-(d) depicts the real curves of the PV power generation, day-ahead prices, and imbalance ratio used in the two schemes. Note that the predicted and scenario curves are used in $\mathcal{P}^S$ and $\mathcal{P}^D$, while the actual curves are used for evaluation. Figures 6.10(a)-(d) and 6.10(e)-(h) illustrate the scheduled day-ahead decisions of the PV-BESS plant as well as the actual system operation using Problems $\mathcal{P}^D$ and $\mathcal{P}^S$, respectively. Figures 6.10(a) and 6.10(e) show the predicted, actual, and scheduled PV power, indicating the high prediction error between predicted and actual generation. Figures 6.10(b) and 6.10(f) depict the scheduled and actual grid power based on the PV generation and BESS power decisions shown in Figures 6.10(c) and 6.10(g), respectively. As demonstrated in Figures 6.10(g)-(h), Problem $\mathcal{P}^S$ charges the BESS during the critical hours from 10:00 to 14:00, where the actual PV generation may exceed the power grid limits, reducing the PV power curtailments from 4.24 MWh to 2.02 MWh compared to $\mathcal{P}^D$. Problems $\mathcal{P}^D$ and $\mathcal{P}^S$ avoid to fully charge the BESS to reduce the degradation cost (see Figures 6.10(d) and 6.10(h)), presenting a degradation of 0.0163% and 0.0271% that corresponds to 81.35€ and 135.7€, respectively. The uncertainty-aware decisions of Problem $\mathcal{P}^S$ increase the daily producer profit from 16447.3€ to 17203.6€

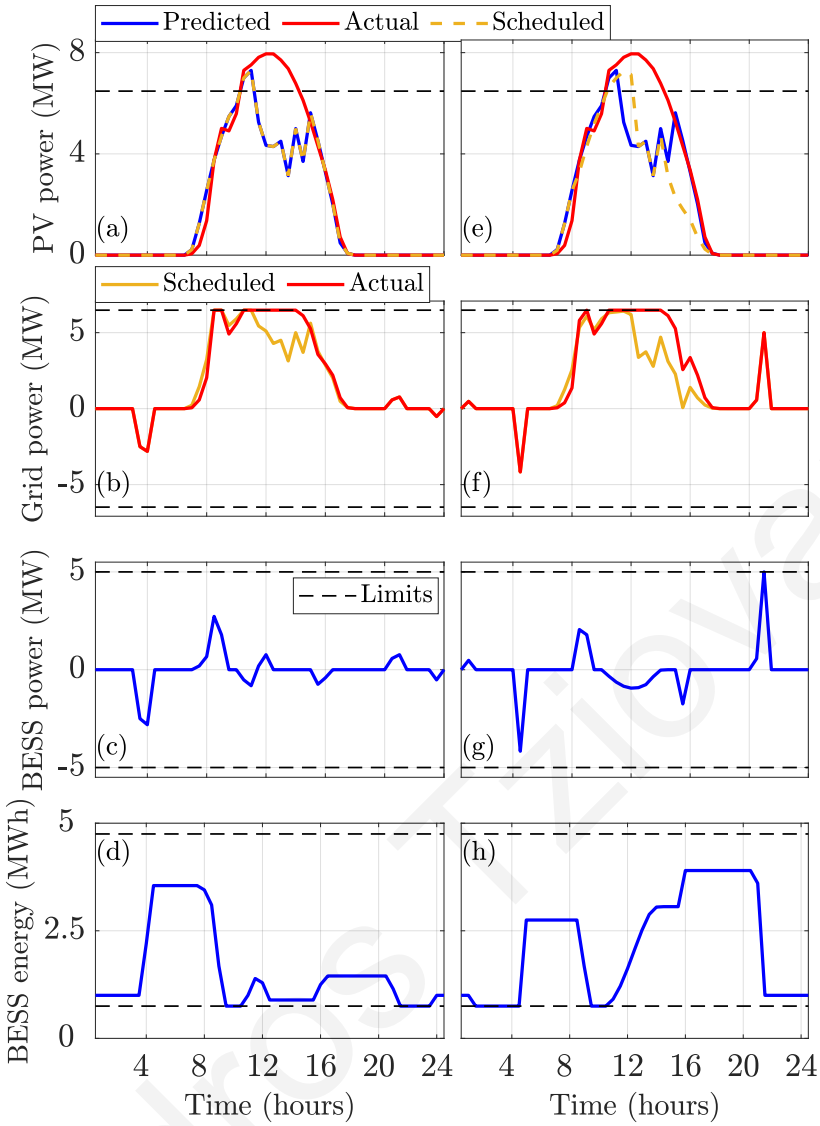

Figure 6.10: The scheduled day-ahead decisions of the PV-BESS plant as well as the actual system operation using Problems $\mathcal{P}^D$ (a)-(d) and $\mathcal{P}^S$ (e)-(h) when the BESS degradation model is used in both optimization problems.

compared to $\mathcal{P}^D$, achieving a profit increment of 4.59%.

The execution times of $\mathcal{P}^D$ and $\mathcal{P}^S$ are 0.1 and 7.1 seconds, indicating that the formulated linear programs can be solved fast even when a large number of scenarios is utilized in $\mathcal{P}^S$.

Aggregate performance evaluation. Table 6.2 presents the total producer profits and PV power curtailments using Problems $\mathcal{P}^B$, $\mathcal{P}^D$, $\mathcal{P}^S$, and $\mathcal{P}^I$ for the period 01/02/2022-30/09/2022. Problem $\mathcal{P}^D$ reduces the PV curtailments from 551.4 MWh to 195.5 MWh and increases the profit by 3.7% compared to $\mathcal{P}^B$. Table 6.2 shows that Problem $\mathcal{P}^S$ reduces the PV curtailments to 71.4 MWh and increases the profit by 5.0%, highlighting the superiority of the proposed stochastic scheme compared to

Table 6.2: Total actual producer profits and PV power curtailments for the period 01/02/2022-30/09/2022 using the different problems.

Problem	Profit (€)	Profit increment (%)	PV curtailments (MWh)
$\mathcal{P}^B$	1,936,181		551.4
$\mathcal{P}^D$	2,007,600	3.7	195.5
$\mathcal{P}^S$	2,032,480	5.0	71.4
$\mathcal{P}^I$	2,106,399	8.8	21.5

$\mathcal{P}^D$. Problem $\mathcal{P}^I$ presents total PV curtailments of 21.5 MWh, indicating that the BESS capacity is insufficient to always ensure the power grid limits. Problem $\mathcal{P}^I$, which is unrealizable, increases the profit by 8.8% compared to $\mathcal{P}^B$, indicating that Problem $\mathcal{P}^S$ can yield even higher profits, e.g., by selecting the scenarios in a more sophisticated way and employing an operating strategy. Note that the BESS relaxation exactness is always satisfied in the simulation results, obtaining the optimal solution, for both the wind-BESS and PV-BESS producers.

6.7 Conclusions

This chapter developed a bidding strategy for RES-BESS producers to maximize their expected profits in electricity markets considering BESS degradation and power grid limits. To address the non-convexities associated with the BESS, a linear deterministic optimization scheme is developed that incorporates an approximate cycle-based degradation model and a relaxed BESS model. Moreover, a scenario-based linear stochastic optimization scheme is developed to handle uncertainties in RES power generation, day-ahead energy prices, and imbalance prices. Simulation results indicate the capability of the proposed stochastic scheme to increase the profits of the wind-BESS and PV-BESS producers by 5.9% and 5.0% compared to the base scenario, where the RES forecasting generation profile is directly submitted to the market. Moreover, the results indicate the capability of the stochastic scheme to yield considerably higher profits compared to the corresponding deterministic scheme. The stochastic scheme yields execution times of a few seconds, indicating that it can be fast and reliably solved under a large number of scenarios. Future work will develop more sophisticated scenario selection methodologies to yield even higher

profits using the proposed stochastic scheme.

Chapter 7

Conclusions

This thesis develops optimization schemes for the management of distributed energy resources in power systems under a high RES penetration. The introduced schemes generate fast and optimal or close-to-optimal solutions, while for operational purposes handle well modelling inaccuracies and RES uncertainties. In particular, four such problems were considered with the above characteristics: (i) optimization of general energy management problems in power systems involving non-convex ESS models, (ii) energy management of photovoltaic and battery storage systems in active distribution grids, (iii) energy management of a flywheel storage system for peak shaving applications, and (iv) stochastic optimization of the bidding strategy of RES producers in electricity markets considering battery degradation. In the remainder, we summarise the main contributions and conclusions associated with each technical thesis chapter.

Optimization of general energy management problems in power systems involving non-convex ESS models: Chapter 3 addresses the issue of the ESS relaxation violation by developing two successive convexification algorithms that generate fast and high-quality feasible solutions when the derived solution is not exact. The first algorithm handles general ESS loss functions, while the second specialized algorithm enhances the algorithm performance when piecewise-linear loss functions are used. The two algorithms are applied in two different optimization problems in power systems, the *Unit Commitment* and *Peak Shaving and Energy Arbitrage* problems, to investigate their performance considering piecewise-linear and quadratic ESS loss functions. Simulation results indicate the capability of the proposed al-

gorithms to yield almost optimal, if not optimal, solutions with significantly lower execution times compared to state-of-the-art solvers that utilize exact ESS models. Specifically, the proposed algorithms reduce the average execution time by 50% for the Unit Commitment problem, which remains nonconvex even upon relaxation, and achieve a 2-3 orders of magnitude speedup for the Peak Shaving and Energy Arbitrage problem, which becomes convex upon relaxation.

Energy management of photovoltaic and battery storage systems in active distribution grids: Chapter 4 proposes a centralized energy management and control scheme for managing the PVs-BESSs operation in smart distribution grids. The proposed scheme minimizes both the prosumers electricity cost and the grid energy losses cost, while ensuring reliable grid operation by incorporating power flow constraints and reactive power support. Because the resulting optimization model is non-convex, we develop a convex second-order cone program by appropriately relaxing the non-convex constraints which yields optimal results in most operating conditions, especially under "normal" operating conditions. To ensure feasibility under all operating conditions, we develop an algorithm that utilizes the convexified model to yield feasible solutions under "extreme" operating conditions. In addition, we propose a second algorithm to find the operating point that minimizes the absolute difference between the objective gain losses, providing fairness between the prosumers and the grid costs. Simulation results indicate the effectiveness and superiority of the proposed scheme in comparison with a self-consumption approach, even under PV generation uncertainty. Specifically, the proposed scheme reduces the prosumers daily electricity cost by 20.6% compared to the self-consumption approach. In addition, the self-consumption approach presents voltage violations, while the proposed scheme always satisfies the constraints of the power grid.

Energy management of a flywheel storage system for peak shaving applications: Chapter 5 investigates the provision of peak shaving services from a FESS installed in a transformer substation. FESS power losses and maximum power functions are constructed to be dependent on parameters that are readily available through commercial FESS interfaces (charging/discharging power and SoC). Moreover, the derived FESS functions are modeled with convex constraints that enable the formulation of convex optimization problems. Using the derived FESS functions we develop

a new optimization formulation for the peak-shaving problem that minimizes the transformer power limit violations and FESS power losses in a lexicographic fashion. In addition, we develop a two-level hierarchical control scheme to solve the peak-shaving problem fast and reliably, while handling prediction errors and modelling inaccuracies. The proposed hierarchical control scheme is integrated and validated in an experimental setup. Specifically, we validate the proposed FESS modelling and we identify the FESS parameters, indicating the high accuracy of the derived functions to estimate the FESS power losses and maximum power. Moreover, we validate the effectiveness of the proposed energy management and control scheme to provide peak shaving services through simulation and experimental results. The proposed scheme enables the active management of distribution grids and increases the hosting capacity for PV installations and load demand growth in power grids.

Stochastic optimization of the bidding strategy of RES producers in electricity markets considering battery degradation: Chapter 6 presents a bidding strategy for combined BESS-RES plants to maximize expected producer profits in day-ahead and balancing markets, while taking into account battery degradation and power grid limits due to transmission congestion. To address uncertainty in RES power generation, day-ahead energy prices, and imbalance prices, a two-stage scenario-based stochastic optimization scheme is developed. The scheme is formulated as a linear program, which can be solved quickly and reliably, using an approximate cycle-based degradation model and a relaxed BESS model. Simulation results demonstrate that the proposed stochastic scheme can increase the profits of wind-BESS and PV-BESS producers by 5.9% and 5.0%, respectively, compared to the base case scenario where the RES forecasting generation profile is submitted to the market. Furthermore, the results indicate that the proposed scheme can yield considerably higher profits compared to the corresponding deterministic scheme. Despite the consideration of a large number of scenarios, the proposed scheme yields execution times of the order of a few seconds.

Chapter 8

Future work

There are several interesting directions for future research based on the work undertaken in this thesis. Next, we provide suggestions for further work for the two problems presented in Chapters 4 and 6.

Energy management of photovoltaic and battery storage systems in active distribution grids: Chapter 4 proposed a centralized energy management and control scheme for managing the PVs-BESSs operation in smart distribution grids. Specifically, the proposed scheme manages the power set-points of all PVs-BESSs in the distribution grid to minimize both the prosumers electricity cost and the grid energy losses cost, while ensuring reliable grid operation by incorporating power flow constraints.

The considered problem faces two main challenges. The first is the lack of scalability of the centralized architecture. The second is the inherent uncertainty in electricity prices, PV generation, and load demand for each prosumer that needs explicit consideration. The proposed centralized scheme optimized the entire system by taking into account system-level objectives and constraints. In this respect, this scheme requires full knowledge of prosumer models and a central entity to collect and process information from all prosumers. Although the resulting problem is convex and can be solved fast, the execution time increases considerably when larger distribution grids are considered. Furthermore, high prediction errors in PV generation, load demand, and electricity prices may have a negative impact on the prosumers' profits, despite the fact that the developed MPC framework handles modelling inaccuracy and PV generation uncertainty well.

To address these issues, a promising direction is to develop distributed optimization solution methods. One popular approach for distributed optimization is the alternating direction method of multipliers (ADMM). With ADMM, the optimization problem can be decomposed into a set of subproblems, each solved by a local controller or agent. Each agent, such as a prosumer, only has access to its own local information and solves its own subproblem, without necessarily having access to the complete information of the system. The agents communicate and exchange information with each other through a centralized coordinator, who oversees the convergence of the algorithm. To address the uncertainty in electricity prices, PV generation, and load demand, an interesting direction is to develop stochastic optimization schemes. Considering the ADMM method, each prosumer subproblem can be formulated as a stochastic optimization problem, maximizing the expected prosumer profit by making uncertainty-aware decisions for its PV-BESS system.

Stochastic optimization of the bidding strategy of RES producers in electricity markets considering battery degradation: Chapter 6 presented a bidding strategy for combined BESS-RES plants to maximize the expected producer profits in day-ahead and balancing markets, while taking into account battery degradation and power grid limits due to transmission congestion. To address uncertainty in RES power generation, day-ahead energy prices, and imbalance prices, a two-stage scenario-based stochastic optimization scheme was developed.

The main challenge of the developed scenario-based stochastic optimization scheme is the selection of scenarios, as the effectiveness of the proposed scheme depends on the representative scenarios that capture a wide range of possible outcomes of the underlying stochastic processes. Selecting a small set of scenarios may not fully represent uncertainty, while considering a large set of scenarios can result in computational issues, when handling multiple sources of uncertainty. In the proposed scheme, the scenario set is constructed by combining three sources of uncertainty in relation to RES generation, day-ahead price, and imbalance price curves. Therefore, selecting a large number of curves to represent each source of uncertainty can result in a vast number of scenarios.

An interesting direction for future research is to explore scenario selection methodologies, including various scenario-generation techniques for building appropriate sets of scenarios that represent stochastic processes. Furthermore, it would be worth-

while to examine scenario-reduction techniques that can effectively reduce scenarios to overcome computational challenges, while maintaining the important features of the original scenario set.

Another promising direction is the development of operating strategies for the energy management of RES-BESS plants during actual operations. The aim of such strategies is to maximize the producer profits by making corrective decisions based on real-time information about the RES generation and imbalance price. To achieve this, a stochastic MPC controller can be developed to optimize the RES-BESS power set-points in real operation, considering the scheduled RES-BESS production profile submitted to the day-ahead market and uncertainty in RES generation and imbalance prices.

Bibliography

[1] *Renewable Energy Sources*, IRENA. [Online]. Available: https://www.irena.org/

[2] *2050 Climate and Energy Strategy*, European Commission. [Online]. Available: https://ec.europa.eu/clima/eu-action/climate-strategies-targets/2050-long-term-strategy_en

[3] I. A. Essackjee and R. T. F. Ah King, "The impact of increasing penetration level of small scale distributed generations on voltage in a secondary distribution network," in *IEEE EmergiTech*, 2016, pp. 245–250.

[4] D. Chathurangi, U. Jayatunga, M. Rathnayake, A. Wickramasinghe, A. Agalgaonkar, and S. Perera, "Potential power quality impacts on LV distribution networks with high penetration levels of solar PV," in *IEEE ICHQP*, 2018, pp. 1–6.

[5] J. M. Lavalliere, H. A. Abdelsalam, and E. B. Makram, "Impact of PV on peak load shaving on an actual distribution system," in *2015 North American Power Symposium (NAPS)*, 2015, pp. 1–6.

[6] *Power System Production*, Cyprus Transmission System Operator (CTSO), 2021. [Online]. Available: https://tsoc.org.cy/electrical-system/total-daily-system-generation-on-the-transmission-system/

[7] H. Nosair and F. Bouffard, "Reconstructing operating reserve: Flexibility for sustainable power systems," *IEEE Transactions on Sustainable Energy*, vol. 6, no. 4, pp. 1624–1637, 2015.

[8] Y. Wu *et al.*, "A review of flexibility requirement of electric generators in high wind power penetration systems," in *IEEE ICASI*, 2017, pp. 1890–1893.

[9] A. Jain, S. Yamujala, P. Das, A. S. Gaur, R. Bhakar, J. Mathur, and P. Kushwaha, "Unit commitment framework to assess flexibility resource capability for high RES penetration," in *2020 IEEE PES ISGT-Europe*, 2020, pp. 779–783.

[10] *Electricity Storage and Renewables: Costs and Markets to 2030*, IRENA, 2017. [Online]. Available: https://www.irena.org/publications/2017/oct/electricity-storage-and-renewables-costs-and-markets

[11] *Five Steps to Energy Storage*, World Energy Council, 2020. [Online]. Available: https://www.worldenergy.org/publications/entry/innovation-insights-brief-five-steps-to-energy-storage

[12] N. Günter and A. Marinopoulos, "Energy storage for grid services and applications: Classification, market review, metrics, and methodology for evaluation of deployment cases," *Journal of Energy Storage*, vol. 8, p. 226–234, 2016.

[13] *Access to Energy*, Our World in Data, 2021. [Online]. Available: https://ourworldindata.org/energy-access

[14] *Challenges and opportunities in global battery storage markets*, Deloitte, 2018. [Online]. Available: https://www2.deloitte.com/content/dam/Deloitte/bg/Documents/energy-resources/gx-er-challenges-opportunities-global-battery-storage-markets.pdf

[15] M. S. Ziegler and J. E. Trancik, "Re-examining rates of lithium-ion battery technology improvement and cost decline," *Energy and Environmental Science*, vol. 14, p. 1635–1651, 2021.

[16] A. Astolfi, *The Art of Optimization*. Imperial College London, 2018.

[17] S. Boyd and L. Vandenberghe, *Convex optimization*. Cambridge university press, 2014.

[18] D. Bertsimas and J. Tsitsiklis, *Introduction to Linear Optimization*. Athena Scientific, 1997.

[19] *MOSEK Modeling Cookbook*, MOSEK ApS, 2021. [Online]. Available: https://docs.mosek.com/modeling-cookbook/index.html

[20] P. Williams, *Model Building in Mathematical Programming*. Wiley, 2013.

[21] R. T. Marler and J. S. Arora, "The weighted sum method for multiobjective optimization: New insights," *Structural and Multidisciplinary Optimization*, vol. 41, p. 853–862, 2010.

[22] H. Isermann, "Linear lexicographic optimization," *OR Spektrum 4*, pp. 223–228, 1982.

[23] A. Bemporad, *Model Predictive Control*, IMT School for Advanced Studies Lucca, 2021. [Online]. Available: http://cse.lab.imtlucca.it/~bemporad/teaching/mpc/imt/1-linear_mpc.pdf

[24] E. F. Camacho and C. Bordons, *Model Predictive Control*. Springer, 2007.

[25] A. J. Conejo *et al.*, *Decision Making Under Uncertainty in Electricity Markets*. Springer, 2010.

[26] L. A. Roald, D. Pozo, A. Papavasiliou, D. Molzahn, J. Kazempour, and A. Conejo, "Power systems optimization under uncertainty: A review of methods and applications," *Electric Power Systems Research*, vol. 214, p. 1–25, 2023.

[27] P. Haessig, "Convex storage loss modeling for optimal energy management," in *2021 IEEE Madrid PowerTech*, 2021, pp. 1–6.

[28] Q. Li, R. Ayyanar, and V. Vittal, "Convex optimization for DES planning and operation in radial distribution systems with high penetration of photovoltaic resources," *IEEE Transactions on Sustainable Energy*, vol. 7, no. 3, pp. 985–995, July 2016.

[29] R. Zafar *et al.*, "Optimal dispatch of battery energy storage system using convex relaxations in unbalanced distribution grids," *IEEE Transactions on Industrial Informatics*, vol. 16, no. 1, pp. 97–108, Jan. 2020.

[30] Z. Li *et al.*, "Storage-like devices in load leveling: Complementarity constraints and a new and exact relaxation method," *Applied Energy*, vol. 151, pp. 13–22, 2015.

[31] K. Garifi *et al.*, "Convex relaxation of grid-connected energy storage system models with complementarity constraints in dc opf," *IEEE Transactions on Smart Grid*, vol. 11, no. 5, pp. 4070–4079, Sept. 2020.

[32] M. F. Zia *et al.*, "Energy management system for an islanded microgrid with convex relaxation," *IEEE Transactions on Industry Applications*, vol. 55, no. 6, pp. 7175–7185, Dec. 2019.

[33] Z. Li *et al.*, "Sufficient conditions for exact relaxation of complementarity constraints for storage-concerned economic dispatch," *IEEE Transactions on Power Systems*, vol. 31, no. 2, pp. 1653–1654, March 2016.

[34] C. Shao *et al.*, "Cooperative dispatch of wind generation and electric vehicles with battery storage capacity constraints in SCUC," *IEEE Transactions on Smart Grid*, vol. 5, no. 5, pp. 2219–2226, Sept. 2014.

[35] D. Pozo *et al.*, "Unit commitment with ideal and generic energy storage units," *IEEE Transactions on Power Systems*, vol. 29, no. 6, pp. 2974–2984, Nov. 2014.

[36] Y. Wen *et al.*, "Enhanced security-constrained unit commitment with emerging utility-scale energy storage," *IEEE Transactions on Power Systems*, vol. 31, no. 1, pp. 652–662, Jan. 2016.

[37] B. Zhao *et al.*, "Using electrical energy storage to mitigate natural gas-supply shortages," *IEEE Transactions on Power Systems*, vol. 33, no. 6, pp. 7076–7086, Nov. 2018.

[38] X. Zhang *et al.*, "Coordinated investment in transmission and storage systems representing long- and short-term uncertainty," *IEEE Transactions on Power Systems*, vol. 33, no. 6, pp. 7143–7151, Nov. 2018.

[39] J. M. Arroyo *et al.*, "On the use of a convex model for bulk storage in MIP-based power system operation and planning," *IEEE Transactions on Power Systems*, vol. 35, no. 6, pp. 4964–4967, Nov. 2020.

[40] P. Yang and A. Nehorai, "Joint optimization of hybrid energy storage and generation capacity with renewable energy," *IEEE Transactions on Smart Grid*, vol. 5, no. 4, pp. 1566–1574, July 2014.

[41] M. Petrik and S. Zilberstein, "A bilinear programming approach for multiagent planning," *Journal of Artificial Intelligence Research*, vol. 35, pp. 235–274, 2009.

[42] S. Chouhan *et al.*, "Der optimization to determine optimum bess charge/discharge schedule using linear programming," in *Proc. IEEE Power and Energy Society General Meeting (PESGM)*, 2016, pp. 1–5.

[43] *Gurobi Optimizer Reference Manual*, Gurobi Optimization, 2022. [Online]. Available: http://www.gurobi.com

[44] J. Dong *et al.*, "Distribution voltage control: current status and future trends," in *Proc. IEEE PEDG*, 2018, pp. 1–7.

[45] L. Park *et al.*, "Prosumer energy management considering contract with consumers under progressive pricing policy," *IEEE Access*, vol. 8, pp. 115 789–115 799, 2020.

[46] C. Feng *et al.*, "Decentralized short-term voltage control in active power distribution systems," *IEEE Transactions on Smart Grid*, vol. 9, no. 5, pp. 4566–4576, 2018.

[47] Q. Nguyen *et al.*, "Exact optimal power dispatch in unbalanced distribution systems with high PV penetration," *IEEE Transactions on Power Systems*, vol. 34, no. 1, pp. 718–728, Jan. 2019.

[48] E. Dall'Anese *et al.*, "Optimal dispatch of photovoltaic inverters in residential distribution systems," *IEEE Transactions on Sustainable Energy*, vol. 5, no. 2, pp. 487–497, Apr. 2014.

[49] X. Su *et al.*, "Optimal PV inverter reactive power control and real power curtailment to improve performance of unbalanced four-wire LV distribution networks," *IEEE Transactions on Sustainable Energy*, vol. 5, no. 3, pp. 967–977, Jul. 2014.

[50] D. Ranamuka, K. M. Muttaqi, and D. Sutanto, "Flexible AC power flow control in distribution systems by coordinated control of distributed solar-PV and battery energy storage units," *IEEE Transactions on Sustainable Energy*, vol. 11, no. 4, pp. 2054–2062, Oct. 2020.

[51] J. Tant *et al.*, "Multiobjective battery storage to improve PV integration in residential distribution grids," *IEEE Transactions on Sustainable Energy*, vol. 4, no. 1, pp. 182–191, Jan. 2013.

[52] D. Zarrilli *et al.*, "Energy storage operation for voltage control in distribution networks: A receding horizon approach," *IEEE Transactions on Control Systems Technology*, vol. 26, no. 2, pp. 599–609, Mar. 2018.

[53] P. Fortenbacher *et al.*, "Modeling and optimal operation of distributed battery storage in low voltage grids," *IEEE Transactions on Power Systems*, vol. 32, no. 6, pp. 4340–4350, Nov. 2017.

[54] P. M. van de Ven *et al.*, "Optimal control of end-user energy storage," *IEEE Transactions on Smart Grid*, vol. 4, no. 2, pp. 789–797, Jun. 2013.

[55] S. Kim *et al.*, "Optimal operation control for multiple BESSs of a large-scale customer under time-based pricing," *IEEE Transactions on Power Systems*, vol. 33, no. 1, pp. 803–816, Jan. 2018.

[56] J. Hu *et al.*, "Energy management strategy for a society of prosumers under the IOT environment considering the network constraints," *IEEE Access*, vol. 7, no. 1, pp. 57 760–57 768, May 2019.

[57] P. Zhuang *et al.*, "Hierarchical and decentralized stochastic energy management for smart distribution systems with high BESS penetration," *IEEE Transactions on Smart Grid*, vol. 10, no. 6, pp. 6516–6527, Nov. 2019.

[58] P. Tian *et al.*, "A hierarchical energy management system based on hierarchical optimization for microgrid community economic operation," *IEEE Transactions on Smart Grid*, vol. 7, no. 5, pp. 2230–2241, Sept. 2016.

[59] H. Gao *et al.*, "Decentralized energy management for networked microgrids in future distribution systems," *IEEE Transactions on Power Systems*, vol. 33, no. 4, pp. 3599–3610, Jul. 2018.

[60] M. Rastegar *et al.*, "Developing a two-level framework for residential energy management," *IEEE Transactions on Smart Grid*, vol. 9, no. 3, pp. 1707–1717, May 2018.

[61] P. Olivella-Rosell *et al.*, "Centralised and distributed optimization for aggregated flexibility services provision," *IEEE Transactions on Smart Grid*, vol. 11, no. 4, pp. 3257–3269, July 2020.

[62] C. Zhang *et al.*, "Multi-objective adaptive robust voltage/VAR control for high-PV penetrated distribution networks," *IEEE Transactions on Smart Grid*, vol. 11, no. 6, pp. 5288–5300, Nov. 2020.

[63] C. Roman and W. Rosehart, "Evenly distributed pareto points in multi-objective optimal power flow," *IEEE Transactions on Power Systems*, vol. 21, no. 2, pp. 1011–1012, May 2006.

[64] Y. Fu *et al.*, "Multiobjective stochastic economic dispatch with variable wind generation using scenario-based decomposition and asynchronous block iteration," *IEEE Transactions on Sustainable Energy*, vol. 7, no. 1, pp. 139–149, Jan. 2016.

[65] L. Gan *et al.*, "Exact convex relaxation of optimal power flow in radial networks," *IEEE Transactions on Automatic Control*, vol. 60, no. 1, pp. 72–87, Jan. 2015.

[66] M. Farivar and S. H. Low, "Branch flow model: Relaxations and convexification-Part I," *IEEE Transactions on Power Systems*, vol. 28, no. 3, pp. 2554–2564, Aug. 2013.

[67] S. Nykamp *et al.*, "Value of storage in distribution grids—competition or cooperation of stakeholders?" *IEEE Transactions on Smart Grid*, vol. 4, no. 3, pp. 1361–1370, Sept. 2013.

[68] M. H. Pandya *et al.*, "Enhancing the distribution feeder capacity through energy storage," in *Proc. IEEE ICIT*, 2013, pp. 1739–1744.

[69] F. Nadeem *et al.*, "Comparative review of energy storage systems, their roles, and impacts on future power systems," *IEEE Access*, vol. 7, pp. 4555–4585, 2019.

[70] M. Farhadi and O. Mohammed, "Energy storage technologies for high-power applications," *IEEE Transactions on Industry Applications*, vol. 52, no. 3, pp. 1953–1961, 2016.

[71] Y. Yang *et al.*, "Cost-benefit study of dispersed battery storage to increase penetration of photovoltaic systems on distribution feeders," in *Proc. IEEE PES General Meeting*, 2014, pp. 1–5.

[72] T. Zhang *et al.*, "Distribution feeder upgrade deferral through use of energy storage systems," in *Proc. IEEE PES General Meeting*, 2016, pp. 1–5.

[73] D. Kodaira, W. Jung, and S. Han, "Optimal energy storage system operation for peak reduction in a distribution network using a prediction interval," *IEEE Transactions on Smart Grid*, vol. 11, no. 3, pp. 2208–2217, Oct. 2019.

[74] J. Tant *et al.*, "Multiobjective battery storage to improve PV integration in residential distribution grids," *IEEE Transactions on Sustainable Energy*, vol. 4, no. 1, pp. 182–191, Jan. 2013.

[75] Z. Taylor *et al.*, "Battery-assisted distribution feeder peak load reduction: Stochastic optimization and utility-scale implementation," in *Proc. IEEE PES General Meeting*, 2016, pp. 1–5.

[76] Z. Taylor, H. Akhavan-Hejazi, *et al.*, "Customer-side SCADA-assisted large battery operation optimization for distribution feeder peak load shaving," *IEEE Transactions on Smart Grid*, vol. 10, no. 1, pp. 992–1004, Jan. 2019.

[77] A. Nagarajan and R. Ayyanar, "Design and strategy for the deployment of energy storage systems in a distribution feeder with penetration of renewable resources," *IEEE Transactions on Sustainable Energy*, vol. 6, no. 3, pp. 1085–1092, July 2015.

[78] G. Parise *et al.*, "Comprehensive peak-shaving solutions for port cranes," *IEEE Transactions on Industry Applications*, vol. 53, no. 3, pp. 1799–1806, 2017.

[79] F. Díaz-González, F. D. Bianchi, *et al.*, "Control of a flywheel energy storage system for power smoothing in wind power plants," *IEEE Transactions on Energy Conversion*, vol. 29, no. 1, pp. 204–214, March 2014.

[80] G. O. Suvire *et al.*, "Improving the integration of wind power generation into AC microgrids using flywheel energy storage," *IEEE Transactions on Smart Grid*, vol. 3, no. 4, pp. 1945–1954, Dec. 2012.

[81] F. Islam *et al.*, "Smoothing of wind farm output by prediction and supervisory-control-unit-based FESS," *IEEE Transactions on Sustainable Energy*, vol. 4, no. 4, pp. 925–933, Oct. 2013.

[82] F. Díaz-González *et al.*, "Energy management of flywheel-based energy storage device for wind power smoothing," *Applied Energy*, vol. 110, no. 4, pp. 207–219, Oct. 2013.

[83] H. H. Abdeltawab *et al.*, "Robust energy management of a hybrid wind and flywheel energy storage system considering flywheel power losses minimization and grid-code constraints," *IEEE Transactions on Industrial Electronics*, vol. 63, no. 7, pp. 4242–4254, July 2016.

[84] *FIWARE: The Open Source Platform for Our Smart Digital Future*, FIWARE, 2020. [Online]. Available: https://www.fiware.org

[85] S. T. Gurumurthy *et al.*, "Apportioning and mitigation of losses in a flywheel energy storage system," in *Proc. IEEE PEDG*, 2013, pp. 1–6.

[86] C. S. Hearn *et al.*, "Utilization of optimal control law to size grid-level flywheel energy storage," *IEEE Transactions on Sustainable Energy*, vol. 4, no. 3, pp. 611–618, July 2013.

[87] C. Shi *et al.*, "Charging-discharging control strategy for a flywheel array energy storage system based on the equal incremental principle," *Energies Open Access Journal*, vol. 12, pp. 1–27, July 2019.

[88] A. Soomro *et al.*, "Performance and loss analysis of squirrel cage induction machine based flywheel energy storage system," *Applied Sciences*, vol. 9, no. 21, Oct. 2019.

[89] L. Mears *et al.*, "EPRI-DOE handbook of energy storage for transmission and distribution applications," *Electric Power Research Institute; U.S Department of Energy*, 2003.

[90] X. Chang *et al.*, "Active disturbance rejection control for a flywheel energy storage system," *IEEE Transactions on Industrial Electronics*, vol. 62, no. 2, pp. 991–1001, Feb. 2015.

[91] C. Sourkounis, "Storage system management for power conditioning in wind parks," in *Proc. IEEE ENERGYCON*, 2014, pp. 597–602.

[92] Y. Yang *et al.*, "A hybrid power control concept for PV inverters with reduced thermal loading," *IEEE Transactions on Power Electronics*, vol. 29, no. 12, pp. 6271–6275, Dec. 2014.

[93] J. M. Morales, A. J. Conejo, *et al.*, *Integrating Renewables in Electricity Markets*. Springer, 2014.

[94] J. M. Morales, A. J. Conejo, and J. Perez-Ruiz, "Short-term trading for a wind power producer," *IEEE Transactions on Power Systems*, vol. 25, no. 1, pp. 554–564, Feb. 2010.

[95] T. Qi *et al.*, "Prediction-free online dispatch of remote wind-storage plant considering transmission congestion," in *Proc. IEEE 40th Chinese Control Conference (CCC)*, 2021, pp. 1675–1680.

[96] A. Berrueta *et al.*, "Identification of critical parameters for the design of energy management algorithms for li-ion batteries operating in pv power plants," *IEEE Transactions on Industry Applications*, vol. 56, no. 5, pp. 4670–4678, Oct. 2020.

[97] N. Padmanabhan *et al.*, "Battery energy storage systems in energy and reserve markets," *IEEE Transactions on Power Systems*, vol. 35, no. 1, pp. 215–226, Jan. 2020.

[98] B. Xu, J. Zhao, T. Zheng, E. Litvinov, and D. S. Kirschen, "Factoring the cycle aging cost of batteries participating in electricity markets," *IEEE Transactions on Power Systems*, vol. 33, no. 2, pp. 2248–2259, March 2018.

[99] B. Xu, A. Oudalov, A. Ulbig, G. Andersson, and D. S. Kirschen, "Modeling of lithium-ion battery degradation for cell life assessment," *IEEE Transactions on Smart Grid*, vol. 9, no. 2, pp. 1131–1140, March 2018.

[100] Y. Shi *et al.*, "A convex cycle-based degradation model for battery energy storage planning and operation," in *Proc. IEEE Annual American Control Conference (ACC)*, 2021, pp. 4590–4596.

[101] Y. Wang *et al.*, "Stochastic coordinated operation of wind and battery energy storage system considering battery degradation," *Journal of Modern Power Systems and Clean Energy*, vol. 4, no. 4, pp. 581–592, Oct. 2016.

[102] N. Mahmoudi *et al.*, "Wind power offering strategy in day-ahead markets: Employing demand response in a two-stage plan," *IEEE Transactions on Power Systems*, vol. 30, no. 4, pp. 1888–1896, July 2015.

[103] E. Heydarian-Forushani *et al.*, "Risk-constrained offering strategy of wind power producers considering intraday demand response exchange," *IEEE Transactions on Sustainable Energy*, vol. 5, no. 4, pp. 1036–1047, Oct. 2014.

[104] M. K. AlAshery *et al.*, "Second-order stochastic dominance constraints for risk management of a wind power producer's optimal bidding strategy," *IEEE Transactions on Sustainable Energy*, vol. 11, no. 3, pp. 1404–1413, July 2020.

[105] H. Ding *et al.*, "Rolling optimization of wind farm and energy storage system in electricity markets," *IEEE Transactions on Power Systems*, vol. 30, no. 5, pp. 2676–2684, Sept. 2015.

[106] A. A. S. de la Nieta *et al.*, "Optimal single wind hydro-pump storage bidding in day-ahead markets including bilateral contracts," *IEEE Transactions on Sustainable Energy*, vol. 7, no. 3, pp. 1284–1294, July 2016.

[107] M. Liu *et al.*, "Dispatch scheduling for a wind farm with hybrid energy storage based on wind and lmp forecasting," *IEEE Transactions on Industry Applications*, vol. 51, no. 3, pp. 1970–1977, June 2015.

[108] A. A. Thatte *et al.*, "Risk measure based robust bidding strategy for arbitrage using a wind farm and energy storage," *IEEE Transactions on Smart Grid*, vol. 4, no. 4, pp. 2191–2199, Dec. 2013.

[109] A. Jamali *et al.*, "Self-scheduling approach to coordinating wind power producers with energy storage and demand response," *IEEE Transactions on Sustainable Energy*, vol. 11, no. 3, pp. 1210–1219, July 2020.

[110] *Day-ahead and imbalance prices*, Spanish electricity market, 2022. [Online]. Available: https://www.esios.ree.es/en

[111] C. Cassisi *et al.*, "Similarity measures and dimensionality reduction techniques for time series data mining," in *Advances in Data Mining Knowledge Discovery and Applications*, 2012, pp. 71–96.

Appendix

Appendix A: Literature-based BESS models

The *exact non-convex BESS model* presented in [33, 34, 40] is expressed as

$$C^B_{t+1,k} = C^B_{t,k} + \Delta T(-\frac{1}{\eta^d_k} P^d_{t,k} + \eta^c_k P^c_{t,k}), \quad \forall t, k \in \mathcal{B}, \tag{A.1}$$

$$\underline{C}^B_k \leq C^B_{t,k} \leq \overline{C}^B_k, \quad C^B_{0,k} = I^B_k, \quad \forall t, k \in \mathcal{B}, \tag{A.2}$$

$$0 \leq P^d_{t,k} \leq \overline{P}^B_k, \quad 0 \leq P^c_{t,k} \leq \underline{P}^B_k, \quad \forall t, k \in \mathcal{B}, \tag{A.3}$$

$$P^d_{t,k} \perp P^c_{t,k} \quad \forall t, k \in \mathcal{B}, \tag{A.4}$$

where variables $P^d_{t,k}$ and $P^c_{t,k}$ denote the discharging and charging power, respectively. The non-convex complementarity constraint (A.4) restricts the simultaneous charging and discharging power.

The non-convex BESS model, Eqs. (A.1) - (A.4), is relaxed to the convex BESS model in [33, 34, 40] by removing the complementarity constraint (A.4). The *relaxed convex BESS model* is exact when simultaneous charging and discharging power does not occur. Moreover, when the two BESS models are used in Problem $\mathbb{P}_R(w)$ instead of the proposed BESS model, then variables $P^B_{t,k}$ must be replaced by $P^B_{t,k} = P^d_{t,k} - P^c_{t,k}$ in the formulation. Under the two literature-based BESS models, the power losses are given

$$\hat{P}^L_{t,k} = e^d_k P^d_{t,k} + e^c_k P^c_{t,k} \quad \forall t, k \in \mathcal{B}. \tag{A.5}$$

The total BESS energy losses are calculated as $\sum_{t \in \mathcal{T}} \sum_{k \in \mathcal{B}} (\hat{P}^L_{t,k}) \Delta T$.